

A STUDY OF THE MARINE BOUNDARY LAYER BY LES-MODELLING AND EXPERIMENTAL OBSERVATIONS WITH A FOCUS ON OFFSHORE WIND ENERGY APPLICATIONS

Von der Fakultät für Mathematik und Physik
der Gottfried Wilhelm Leibniz Universität Hannover

zur Erlangung des Grades

Doktorin der Naturwissenschaften
-Dr. rer. nat.-

genehmigte Dissertation
von

Dipl.-Phys., M.Sc. Beatriz Cañadillas Perdomo

geboren am 18. Februar 1975 in Teneriffa (Spanien)

Hannover 2010

Referent: Prof. Dr. Siegfried Raasch
Korreferent: Prof. Dr. Günter Groß

Tag der Promotion: 18.12.2009

To my family.

Abstract

Over the next few years, an increasing tendency towards offshore wind energy is expected world-wide. One of the main reasons for going offshore is the higher and more constant wind resource at sea than on land, resulting in significantly higher production per unit installed. Current knowledge of offshore conditions is very limited compared to conditions on land and this has placed growing importance on the necessity for research in this field.

The overall goal of this thesis was to get a better understanding of the Marine Atmospheric Boundary Layer (MABL) with respect to turbulence effects in the range where they play a role in wind energy applications. In achieving this goal, several interconnected tasks were undertaken and developed in the present research where a combination of observations and modelling have been used.

The first part of the work was devoted to the analysis of observational data. For this purpose, an extensive data processing has been carried out using a two-year data period provided by the offshore meteorological mast FINO1 located in the North Sea. By doing so, several new insights about offshore conditions have been gained, where the sonic anemometers available at FINO1 were used as primary data source. The eddy covariance technique was used to determine the sensible heat fluxes and wind stresses. The Obukhov length was then derived and the stability parameter (zL^{-1}) calculated. It was found that at FINO1 the boundary layer is often neutral stratified.

In addition, the Monin-Obukhov theory was checked and found to be in close agreement with the FINO1 data, especially for neutral and unstable conditions. Oceanographic data from a Wave-Rider Buoy located close to the FINO1 mast were also used to investigate the sea state dependence on the surface wind stress under neutral conditions. The so-called wave age parameter was derived and used to classify the sea state, namely, pure wind-sea and swell. The analyzed results suggest a general trend of increasing sea roughness with inverse wave age, the trend being less pronounced than those reported in the literature.

Moreover, this study has been used to develop a database of reliable data in order to compare with the model outputs presented in the second part of the thesis.

In the second part of the thesis, Large-Eddy Simulations (LESs) have been performed. LES is considered to be a suitable tool due to its ability to solve most of the energy content in atmospheric turbulence flows. Shear-driven flows (neutral and stable regimes) have been considered here because of their importance in wind energy applications. Furthermore, an LES database is generated and used in conjunction with the FINO1 data to further explore the inherent characteristics of wind shear flows as well as to check the performance of the LES model.

LES model performance has been tested over a number of stability regimes ranging from neutral to moderately stable and for different geostrophic winds. The mean profiles of several parameters

have been compared, namely vertical wind shear, wind direction and turbulence intensity. Moreover, in order to gain a further understanding of the LES approach, a statistical analysis is performed through the selection of a representative neutral case. Good general agreement is found between both datasets.

Finally, a basic study concerning the turbulence effect on wind power density was carried out. Here the relative percentage error committed when using a point measurement at hub height as representation of the whole rotor is investigated for different combination of hub heights and rotor diameters. This error was assessed quantitatively by defining an equivalent wind speed accounting for the spatial variation of the wind speed over the rotor span. It was found that the total mean errors are bigger for stable than for neutral conditions.

Keywords: *Marine Atmospheric Boundary Layer, Offshore Wind Energy, Large Eddy Simulation*

Kurzfassung

In den nächsten Jahren ist damit zu rechnen, dass sich der Ausbau der Windenergie immer stärker auf das Meer verlagern wird. Einer der wichtigsten Gründe, Offshore zu gehen, ist das deutlich höhere Windpotential auf See verbunden mit einer gleichmäßigeren Strömung als an Land. Insgesamt ergibt sich ein signifikant höherer Energieertrag pro installierter Windenergieanlage. Da jedoch über die Offshore-Bedingungen für die Windenergienutzung sehr viel weniger Kenntnisse vorliegen als über die Verhältnisse an Land, besteht hier noch erheblicher Forschungsbedarf.

Das Hauptziel der vorliegenden Dissertation war es, zu einem besseren Verständnis der marinen atmosphärischen Grenzschicht (MABL) in bezug auf Turbulenzen in dem Bereich, in dem sie in der Windenergienutzung eine Rolle spielen, zu gelangen. Um dieses Ziel zu erreichen, mussten im Rahmen des Forschungsprojektes verschiedene miteinander zusammenhängende Aufgaben entwickelt und durchgeführt werden, wobei verschiedene Ansätze und Modelle verwendet wurden.

Der erste Teil der Arbeit befasste sich mit der Analyse von Messdaten. Hierfür war eine umfangreiche Auswertung erforderlich, die auf der Grundlage von zwei Jahren Daten des Messmastes der in der Nordsee gelegenen Forschungsplattform FINO1 durchgeführt wurde. Diese Auswertung erbrachte einige neue Erkenntnisse, wobei die auf der FINO1-Plattform installierten Ultraschallanemometer die wichtigsten Sensoren darstellten. Die Wärmeströme und Windlasten wurden mit Hilfe der sogenannten Eddy-Kovarianz-Methode bestimmt. Anschließend wurde die Obukhov-Länge abgeleitet und der Stabilitätsparameter berechnet. Es stellte sich heraus, dass die auf der FINO1 gemessene Grenzschicht häufig neutral geschichtet ist. Eine Überprüfung anhand der Monin-Obukhov-Theorie ergab eine gute Übereinstimmung mit den FINO1-Daten, insbesondere für neutrale und instabile Grenzschichten. Ozeanographische Daten von einer in der Nähe des FINO1-Mastes befindlichen Seegangsboje wurden genutzt, um den Einfluss des Seegangs auf die marine Grenzschicht zu untersuchen. Aus der Analyse der Ergebnisse ergab sich unter anderem die Tendenz zu einer steigenden Rauigkeit der Meeresoberfläche mit abnehmendem Wellenalter, wobei diese Tendenz weniger ausgeprägt zu sein scheint als bisher in der Literatur berichtet.

Die Untersuchung diente darüber hinaus auch dazu, eine belastbare Datengrundlage zu schaffen, um einen Vergleich mit den im zweiten Teil der Dissertation durchgeführten Large-Eddy-Simulationen (LES) zu ermöglichen.

LES gilt aufgrund seiner Fähigkeit, den größten Teil des Energiegehalts turbulenter atmosphärischer Strömungen aufzulösen, als geeignetes Modell für die Untersuchung der marinen Grenzschicht. Es wurden vor allem Windgradienten bei neutralen und stabilen Verhältnissen untersucht, weil sie für die Windenergieanwendung von besonderer Bedeutung sind. Außerdem wurde eine LES Datenbank aufgebaut, um im Zusammenhang mit den FINO1-Daten die inhärenten Eigenschaften der Strömungen zu untersuchen und die Eignung des LES-Modells überprüfen zu können.

Die Leistungsfähigkeit des LES-Modells wurde in verschiedenen Stabilitätsregimen von neutral bis gemäßigt stabil und bei unterschiedlichen geostrophischen Windgeschwindigkeiten untersucht. Die mittleren Profile von Parametern, die für die Windenergieanwendung von Bedeutung sind, wurden verglichen. Für ein tieferes Verständnis des LES-Ansatzes wurde auch eine statistische Analyse durch Auswahl eines repräsentativen neutralen Falls durchgeführt. Zwischen beiden Datensätzen wurde eine gute allgemeine Übereinstimmung festgestellt.

Schlagwörter: *Marine atmosphärische Grenzschicht, Offshore Windenergie, Grobstruktursimulation*

Acknowledgements

It is probably impossible to thank all the people who have contributed in one way or another to the conclusion of this thesis. To start with, I wish to express my sincere thanks to Prof. Dr. Siegfried Raasch who gave me the opportunity to work in his research group at the Institute of Meteorology and Climatology of Hannover University. His guidance and experience in research have been beneficial as well as his very valuable comments throughout the process of this work. Thank you for always having time to answer my questions.

I would especially like to express my deep gratitude to my daily supervisor Dr. Thomas Neumann at the DEWI-German Wind Energy Institute. Like no other person, he has constantly provided me with helpful suggestions, valuable discussions and never-ending encouragement, limitless patience and support. This thesis could hardly have been done without the help I have obtained from him and I am not thinking just about the work. Many thanks for helping me through the more difficult phases of this thesis.

Furthermore, I wish to thank all members of the PALM group for their very warm welcome each time I visited them. Especially, I wish to thank Björn Witha, Dr. Gerald Steinfeld (no longer at the Institute) and Dr. Marcus Letzel for all the technical support with the PALM model.

The quality of the thesis has been improved considerably thanks to the very helpful comments from Dr. Jinhua Jiang, Dr. Kay Suselj, Dr. Gerald Steinfeld and Dr. Øyving Saetra.

Many thanks also go to the DEWI-German Wind Energy Institute for giving me the opportunity to carry out such interesting research over the last three years. I am grateful to all those colleagues at DEWI who made my day to day life easier, providing me with a working atmosphere which has been very important for me. Special thanks go to Patricia Chaves, Barbara Jurok and Jurgen Röhlje.

Lastly, but definitely not least, my greatest thanks go to my family and friends for all the unconditional support and patience even when I have been away for such long periods, so far away from them. Thanks for always being there.

This study was financially supported by EU under the Sixth Framework Programme (Marie-Curie Programme): *ModObs - Atmospheric Modelling for Wind Energy, Climate and Environment Applications: Exploring Added Value from New Observation Technique (MRTN-CT-2005-019369)*. The financial support is gratefully acknowledged.

The figures in this study were produced using NCAR Command Language (NCL) or MatLab. The text was typeset with L^AT_EX.

Contents

Abstract	iii
Kurzfassung	v
Acknowledgements	vii
List of Figures	xi
List of Tables	xiv
Abbreviations	xv
1 Introduction	1
1.1 Offshore Wind Energy: General Overview	1
1.2 Purpose and Outline of the Thesis	2
2 General Background	5
2.1 Atmospheric Boundary Layer	5
2.1.1 Peculiarities of the Marine Boundary Layer	6
2.2 Turbulence	8
2.2.1 Eddies and Scales of Motion	9
2.2.1.1 The Energy Cascade	10
2.3 Numerical Simulation	11
3 The Offshore Environment According to FINO1 Observations	15
3.1 Introduction	15
3.2 State of Knowledge on the Dependence of Wave Age on Surface Stress	16
3.3 Theoretical Background	18
3.4 Measurements	21
3.4.1 Measurement Site	21
3.5 Results	34
3.5.1 Relationship between Drag Coefficient and Sea State	34
3.5.2 Relationship between Roughness and Sea State	36
3.6 Summary	38

4	Numerical Simulation.	
	Large Eddy Simulations of the Marine Boundary Layer: From Neutral to Stable Conditions	39
4.1	Introduction	39
4.2	Large Eddy simulation: PALM code	41
4.2.1	Governing Equations of Fluid Motion	41
4.2.2	Filter Operation	43
4.2.3	Filtered Governing Equations	44
4.2.4	Subgrid-Scale Modelling	45
4.2.4.1	Turbulence Closure: TKE-based (Eddy-Viscosity) Model	45
4.2.5	Boundary Conditions	47
4.3	Setting of Simulation Resolution: Minimum Time-step	49
4.3.1	Offshore wind turbine	49
4.3.2	Wind Turbine Operating in Turbulent Flow	49
4.4	Model Set-up Strategy	53
4.4.1	Theoretical maximum surface heat flux	55
4.5	Results and Discussions	57
4.5.1	Bulk Parameters	57
4.5.2	Mean and Turbulent Vertical Structure	60
4.5.3	Contribution of SGS Parameterization to Total TKE	66
4.5.4	Sensitivity Tests	68
4.5.4.1	Sensitivity to Grid Size or Resolution	68
4.5.4.2	Sensitivity to Domain Size	71
4.6	Flow visualization: Eddy structure	73
4.7	Summary	79
5	Comparison: LES-simulations and FINO1-observations	80
5.1	Introduction	80
5.2	Profile Comparison	82
5.2.1	Data Selection for Comparison Purposes	82
5.2.2	Results: Profile Comparison	85
5.3	Further Analysis: Time Series	92
5.3.1	Horizontal Wind Velocity Turbulence Power Spectrum	92
5.3.1.1	Spectrum Methodology	93
5.3.1.2	Spectrum Results	93
5.3.2	Probability Density Function of the Horizontal Wind Velocity	97
5.3.2.1	Methodology	97
5.3.2.2	Results	99
5.3.3	Integral Scales of the Horizontal Wind Velocity	100
5.3.3.1	Methodology	100
5.3.3.2	Results	101
5.4	Short-term Extreme Wind Events: Wind Gusts	103
5.4.1	Characterizing Gust Behaviour	103
5.4.2	Gust Factor	104
5.4.3	IEC Gust Shape	105
5.4.3.1	Deterministic Gust Model	105
5.5	Summary	109

6	LES Application: Assessing the Power Density Error when Using Data from One Point at Hub Height as Representative of the Whole WT Rotor Area	110
6.1	Introduction	110
6.2	Theoretical background	112
6.2.1	Power extracted from the wind	112
6.2.2	Turbulence effects	112
6.2.2.1	Temporal fluctuations	113
6.2.2.2	Spatial fluctuations	114
6.3	Methodology	116
6.4	Assessment of Error	119
6.5	Results	120
6.6	Summary	125
7	Conclusions	126
7.1	Future work	128
7.1.1	Observational data	128
7.1.2	Simulation	128
	Bibliography	131
	Curriculum Vitae	141

List of Figures

1.1	Scenario of installed capacity in Germany up to the year 2030 (Source: Windenergie-Institut (2008)).	2
2.1	Vertical structure of the marine boundary layer. p_+ and p_- indicate positive and negative pressure deviations which lead to a driving force p on the waves. Schematic profiles of the shear stress, τ_s , and the pressure drag on the waves, τ_p , and typical height intervals are given on the right-hand side (source: (Emeis and Türk 2009)).	7
2.2	Sketch of the theoretical spectrum for three-dimensional turbulence.	10
2.3	Turbulent scales resolved/modelled by RANS, LES and DNS.	13
3.1	Location of the FINO1 platform. Shaded red areas represent wind farm projects (Source: www.bsh.de).	21
3.2	Field measurements on the FINO1 meteorological mast (source: www.fino-offshore.de).	23
3.3	Layout of the measurement mast at FINO1 (source: www.fino-offshore.de).	24
3.4	Wind direction distribution (wind rose) (left-side panel) and wind speed histogram (with fitted Weibull distributions) (right-side panel) at 40 m over the period analyzed.	25
3.5	Sonic and cup anemometer wind speed ratio at 40 m as a function of wind direction before tower correction (right side of panel) and after tower correction (left side of panel). Data were binned to 5° and the errorbars represent one standard deviation.	26
3.6	Probability distribution function of corrected $\overline{w'\theta'}$ over the study period.	28
3.7	Frequency of occurrence (%) of the zL^{-1} stability parameter.	29
3.8	Non-dimensional wind shear (ϕ_m) versus stability parameter zL^{-1} . Mean values with error bars representing one standard deviation (solid black line). Red dashed line represents the empirical stability function given in Eq. 3.6.	30
3.9	Eddy correlation friction velocity versus 10 m neutral wind speed.	30
3.10	Significant wave height (H_s) versus wind speed at 10 m height and corrected for buoyancy effects.	32
3.11	Wave age probability density function.	33
3.12	Drag coefficient versus wind speed, both at 10 m neutral. Pure wind sea data are distinguished from the swell and mixed sea cases using the criterion on wave age. Bin-median values with the error bar representing one standard deviation are shown on the left side of the panel.	34
3.13	Dimensionless roughness versus inverse wave age for rough sea conditions ($R = u_* z_0 \nu^{-1} > 2.3$). The solid black line represents bin-median values with one standard deviation error bar.	36
3.14	Distribution of friction velocity u_* and peak phase speed C_p in rough sea conditions ($R = u_* z_0 \nu^{-1} > 2.3$).	37
4.1	Actual wind speed profile.	50

4.2	Blade passing through a turbulent eddy (left-side panel). Stationary and rotationally sampled turbulence spectrum (right-side panel).	51
4.3	Temporal evolution of the surface potential temperature for each geostrophic wind from the present study (left) and from Jiménez and Cuxart (2005) study.	56
4.4	Evolution of the mean profiles as surface cooling increases: wind speed (left-side upper panel), wind angle (right-side upper panel), Turbulent Intensity (TI) (left-side middle panel), non-dimensional horizontal kinematic shear stress (right-side middle panel), potential temperature (θ) (left-side lower panel) and Brunt-Väisälä frequency (N) (right-side lower panel) for $u_g = 8 \text{ ms}^{-1}$. See Table 4.5 for acronyms shown in the legend. Note that only the first 300 m above the surface are plotted.	62
4.5	Same as Figure 4.4, but for $u_g = 10 \text{ ms}^{-1}$.	63
4.6	Same as Figure 4.4, but for $u_g = 12 \text{ ms}^{-1}$.	64
4.7	Same as Figure 4.4, but for $u_g = 14 \text{ ms}^{-1}$.	65
4.8	Mean profiles of the total TKE (left side of the panel), subgrid TKE (middle panel) and ratio between TKE_{SGS} and TKE_{total} (right side of the panel) for increasing u_g (Top to bottom). Blue (black) lines correspond to neutral (stable) regime.	67
4.9	Mean profiles at 5 m resolution (solid lines) and 2 m resolution (dashed lines) of horizontal wind speed (upper panel) and potential temperature (bottom panel)	69
4.10	Mean profiles at 5 m resolution (solid lines) and 2 m resolution (dashed lines) of TKE_{total} (upper panel) and TKE_{SGS} (bottom panel)	70
4.11	Profiles of Horizontal wind speed (upper left panel), wind angle (upper right panel) resolved non-dimensional variances (lower left panel) and total and SGS TKE (lower right panel) with varying domain width. Legend shows number of grid points in the horizontal direction. In brackets the resolution used.	71
4.12	Horizontal cross-sections (three first rows) at 40 m, 100 m and 160 m heights and vertical cross-sections at $y = 600 \text{ m}$ for the longitudinal wind velocity (u [ms^{-1}]) for neutral conditions ($u_g = 10 \text{ ms}^{-1}$ (left-side panel) and $u_g = 14 \text{ ms}^{-1}$ (right-side panel)).	75
4.13	Same as Figure 4.12, but for $\overline{w\theta}_s = -0.01 \text{ mKs}^{-1}$.	76
4.14	Same as Figure 4.12, but for $\overline{w\theta}_s = -0.02 \text{ mKs}^{-1}$.	77
4.15	Same as Figure 4.12, but for $\overline{w\theta}_s = -0.03 \text{ mKs}^{-1}$.	78
5.1	Comparison of profiles between simulated (blue) and measured (red) data for $u_g = 8 \text{ ms}^{-1}$. Vertical wind shear (left side of the panel), horizontal wind direction (middle side of the panel) and Turbulent Intensity (TI) (right side of the panel) as cooling surface increases: Neutral (first panel row), S0 ($\overline{w\theta}_s = -0.005 \text{ mKs}^{-1}$) (second panel row), S1 ($\overline{w\theta}_s = -0.01 \text{ mKs}^{-1}$) (third panel row) and S2 ($\overline{w\theta}_s = -0.02 \text{ mKs}^{-1}$) (fourth panel row). Profiles marked with blue dashed lines correspond simulations which suffer from runaway cooling or SGS failure.	86
5.2	Same as Fig. 5.1, but for $u_g = 10 \text{ ms}^{-1}$.	87
5.3	Same as Fig. 5.1, but for $u_g = 12 \text{ ms}^{-1}$.	88
5.4	Same as Fig. 5.1, but for $u_g = 14 \text{ ms}^{-1}$.	89
5.5	Normalized one-dimensional spectra of the horizontal wind velocity fluctuations for LES simulations: 10 m (green), 5 m (blue) and 2 m (red) grid spacing	94
5.6	Normalized one-dimensional spectra of the horizontal wind velocity fluctuations for LES simulations: 2m (red line) grid spacing	95
5.7	Normalized one-dimensional spectra of the horizontal wind velocity fluctuations: LES simulations (blue) and FINO1 data (red)	96

5.8	PDFs of the the horizontal wind velocity fluctuations at 40 m (upper left panel) and at 80 m (upper right panel) and velocity differences (bottom panel). Blue (red) dotted lines represent simulated (measured) data. The standard Gaussian distribution is indicated by the solid lines.	99
5.9	Autocorrelation function for the horizontal wind velocity fluctuations: LES simulation and FINO1 data.	102
5.10	PDFs of velocity fluctuation increments at $\tau = 1, 3, 10$ sec respectively (bottom-up). Red (blue) filled circles denote measured (simulated) data. The standard Gaussian distribution is indicated by solid lines. PDFs are shifted vertically by an offset of 10.	104
5.11	Gust factors as a function of duration time for several fixed averaging times: LES simulation (triangles) and FINO1 measurements (circles).	105
5.12	'Mexican-hat-like' shape IEC gust for different turbulence intensities, 25 m/s mean wind speed and one year return period.	106
5.13	'Mexican-hat-like' shape IEC gust found in the data: LES simulation (blue lines) and FINO1 measurements (red lines).	107
6.1	Wind field evolution over the rotor plane for a 120 m diameter wind turbine at 90 m hub height.	113
6.2	Example of longitudinal (upper panel) and vertical (bottom panel) PDF wind speed increments over the rotor plane (120 m diameter and 90 m hub height) for $u_g = 10 \text{ ms}^{-1}$	115
6.3	Schematic visualization of a 3D velocity field provided by the LES model (left panel). Swept rotor area divided into grids (5 m resolution) (right panel).	116
6.4	Example of time series of wind speed for one point located at hub height (90 m) (black line) and considering the whole rotor diameter (120 m) using Eq. 6.10 (red line).	117
6.5	Wind speed, vertical wind shear (α) (upper panel) and Turbulence Intensity (TI) (lower panel) profiles for each case investigated. Solid (dashed) lines represent neutral (stable) regime.	118
6.6	Example of PDFs of the relative percentage error for a 100 m diameter wind turbine with 90 m hub height wind, for neutral (left panel) and stable (right panel) regimes. The solid line represents the fit to a Gaussian distribution.	120
6.7	Percentage relative mean error [%] in power with varying rotor diameter at 90 m hub height (upper panel), at 100 m hub height (middle panel) and at 110 m hub height (lower panel). Left (right) side of the panel corresponds to neutral (stable) regime.	123
6.8	Average standard deviation of wind speed ($\overline{u_i}(y, z)$) over rotor plane. As before, left (right) side of the panel corresponds to neutral (stable) regime.	124
7.1	LIDAR scanning configuration where each square represents 5 m resolution LES data.	129

List of Tables

3.1	Parameters for the tower correction algorithm.	25
3.2	Parameters describing functional dependence of drag coefficient on neutral 10 m wind speed based on wave age criteria.	35
3.3	a and b coefficients found using different data sets in the literature as well as those found in this study.	35
3.4	Experimental Data.	37
4.1	Technical data for Multibrid M5000. Source: http://www.multibrid.de/	49
4.2	Frequencies of interest over rotor plane.	51
4.3	Summary of the LES simulations. The runs prefixed with NS refer to a neutral and stable regime and the runs prefixed with N refer to a neutral regime only. Note that Δ_z is constant bellow 600m.	54
4.4	Maximum surface heat fluxes [$mK s^{-1}$] derived from Derbyshire's formula for each u_g and different values of R_{fc}	55
4.5	Bulk parameters of the simulated BL evolution computed for the last hour of each section and for $u_g = 8 \text{ ms}^{-1}$. Runs that suffer from runaway cooling (according to Eq. 4.26) are labelled in bold.	59
4.6	Same as Table 4.5, but for $u_g = 10 \text{ ms}^{-1}$	59
4.7	Same as Table 4.5, but for $u_g = 12 \text{ ms}^{-1}$	59
4.8	Same as Table 4.5, but for $u_g = 14 \text{ ms}^{-1}$	59
4.9	Runs with an 'X' correspond to successful runs (free of known failures).	68
5.1	Surface heat flux ($\overline{w\theta_s}$) range considered.	83
5.2	30 m wind speed ranges used to classify the FINO1 data according to the values obtained from the LES results at 27.5 m.	83
5.3	Percentage of the number of observed events [%] in FINO1 that have been simulated with LES.	84
5.4	Summary of Skewness and Kurtosis factors from the PDFs shown in Fig. 5.8.	100
5.5	Integral scales: LES simulation and FINO1 measurements	102
5.6	Summary of Skewness and Kurtosis factors from the PDFs shown in Fig. 5.10.	104
5.7	Number of gusts with a 'Mexican-hat-like' shape	108
6.1	Mean (variance) relative percentage error [%] in power when varying the diameter and hub height in the neutral regime.	122
6.2	Mean (variance) relative percentage error [%] in power when varying the diameter and hub height in the stable regime ($\overline{w\theta_s} = -0.01mK s^{-1}$). Values in bold are suspicious of runaway cooling (see Chapter 4).	122

Abbreviations

Acronyms

ABL	A tmospheric B oundary L ayer
BL	B oundary L ayer
CBL	C onvective B oundary L ayer
CFD	C omputational F luid D ynamics
DEWI	D Eutsche W indenergie I nstitut
DNS	D irect N umerical S imulation
FFT	F ast F ourier T ransform
FINO1	F orschungsplattformen in N ord- und O stsee 1
HLRN	Norddeutsches Rechenzentrum für Hoch- und Höchstleistungsrechnen (German High-Performance Computing Centre North)
IEC	I nternational E lectrotechnical C ommittee
IMUK	I nstitut für M eteorologie und K limatologie (Institute of Meteorology and Climatology), LUH
LES	L arge E ddy S imulation
MABL	M arine A tmospheric B oundary L ayer
MOST	M onin- O bukov S imilarity T heory
NBL	N eutral B oundary L ayer
NSE	N avier S tokes E quations
PALM	P Arallelized- L arge Eddy Simulation M odel
PBL	P lanetary B oundary L ayer
PDF	P robability D ensity F unction
PSD	P ower S pectrum D ensity
RANS	R eynolds- A veraged N avier S tokes

SBL	Stable Boundary Layer
TI	Turbulence Intensity
SGS	SubGrid Scale
TKE	Turbulent Kinetic Energy
WT	Wind Turbine

Greek Letters

α	Wind shear
δ_{ij}	Kronecker delta or identity tensor
Δ	Characteristic grid length
Δt	Time step
Δx	Grid spacing in x-direction
Δy	Grid spacing in y-direction
Δz	Grid spacing in z-direction
ϵ	Turbulent dissipation rate
η	Kolmogorov length scale
κ	Von Kàrman constant
λ	Tip speed ratio
ν_T	Eddy viscosity
Ω	Angular velocity
ϕ	Stability function
ψ	Integrated stability function
ρ	Air density
$\sigma_u, \sigma_v, \sigma_w$	Standard deviation in (x, y, z) directions
τ	Wind stress
ϵ_{rel}	Relative percentage error
ζ	Stability parameter

Roman Letters

A_{rotor}	Wind turbine rotor area
C_{DN}	Neutral drag coefficient

C_D	Drag coefficient
C_p	Wave phase velocity
C_p	Wind turbine power coefficient
D_{rotor}	Wind turbine rotor diameter
f_{cutoff}	Cut-off frequency
f_{max}	Maximum frequency
f_{res}	Resolution frequency
f_c	Coriolis parameter
f_s	Sampling frequency
H_s	Signicant wave height
f	Frequency
k_x, k_y, k_z	Wavenumbers in (x, y, z) directions
K_m, K_h	Turbulent difusion coecients for momentum and heat
K_p	Gust factor
L_x, L_y, L_z	Length of computational domain in (x, y, z) directions
N_x, N_y, N_z	Number of computational cells in (x, y, z) directions
P_{eq}	Equivalent wind power density at hub height
P_{hub}	Wind power density at hub height
P_{wind}	Wind power
Re	Reynolds number
R_{fc}	Critical Richardson ux number
u	Friction velocity
u_g, v_g	Geostrophic wind in (x,y) directions
w_p	Peak wave phase velocity
z_{Ch}	Charnock parameter
z_0	Roughness length
A	Area
f	Frequency
g	Gravitational acceleration
K	Kurtosis
L	Obukhov length
l	Characteristic turbulent length scale
r	Wind turbine radius

Rif	Richardson ux number
P	Mechanical power
S	Skewness
T	Temperature
t	Time
U	Horizontal wind speed
u, v, w	Wind speed components in (x, y, z) directions
u',v',w'	Fluctuation of the wind component in (x, y, z) directions

Chapter 1

Introduction and Motivation

1.1 Offshore Wind Energy: General Overview

Wind energy will play an essential role in meeting the binding target of the European Union (EU) for 20% renewable energy by 2020 ([EU-Commission 2008](#)). While onshore wind energy will remain dominant in the immediate future, in the next few years, an increasing tendency towards offshore wind energy is expected world-wide. Specifically in Germany, for instance, about 11,500 MW are planned to be installed by 2017 in the North Sea and Baltic Sea (Fig. 1.1). One of the main reasons for 'going offshore' is the higher and more constant wind resource at sea than on land, resulting in significantly higher production per unit installed. At the same time, offshore wind farms are more costly to install and maintain than on land. Therefore, to make offshore wind farms economically viable, it is necessary to have a detailed knowledge of offshore conditions.

Current knowledge of offshore conditions is very limited compared to land (partly due to the scarcity and limited time over which measurements have been collected over the sea). This has placed growing importance on the necessity for research in this field as can be seen from the positive political signals and financial incentives. One example is the research project financed by the EU under the Sixth Framework Programme (Marie-Curie Programme): *ModObs - Atmospheric Modelling for Wind Energy, Climate and Environmental Applications: Exploring Added Value from New Observation Techniques (MRTN-CT-2005-019369)*, by which the author of this Ph.D. thesis was also supported.

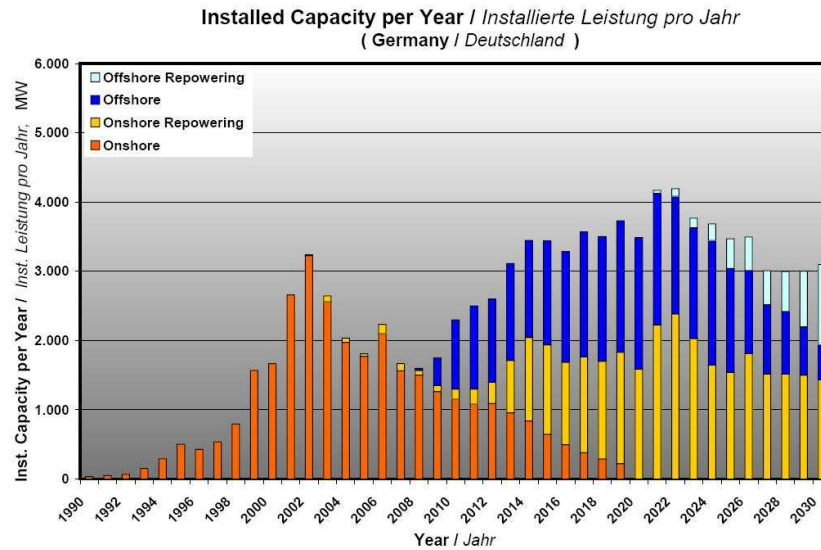


Figure 1.1: Scenario of installed capacity in Germany up to the year 2030 (Source: [Windenergie-Institut \(2008\)](#)).

1.2 Purpose and Outline of the Thesis

The general motivation for this project is to get a better understanding of the marine atmospheric conditions through an analysis of observations and LES-modelling, concentrating in particular on turbulence effects over the range where they play a role in wind energy applications. With this purpose, several interconnected tasks were faced and addressed in the course of the present research. The goal in the long term can be described as follows:

Offshore Environment through Observations: In order to understand the dynamics of wind flow near the surface, a basic understanding of the coupling between the ocean and atmosphere is essential. In this part of the thesis, the dependence of the surface roughness not only on wind speed, but also on wave field (sea state) is investigated.

To address this issue, a two-year database from the offshore platform (FINO1) located in the North Sea was used. This platform provides high quality atmospheric and oceanographic data. This study involves exhaustive data processing with the resulting database used later to test the LES-model results.

LES-Simulations: Exploration of the use of LES for the numerical simulation of the turbulent marine boundary layer.

Large-eddy simulation (LES) is at present the most efficient technique available for high Reynolds number flow simulations, such as for atmospheric boundary layer (ABL)

simulations, in which the larger scale motions are resolved explicitly while the smaller ones are parametrized. LES provides unprecedented high-resolution three-dimensional, time-dependent turbulent data that are accurate enough to tackle turbulence issues on a scale of only a few metres.

LES simulations will be performed for shear-driven flows:

- with a neutral atmosphere boundary layer (NBL)
- and with a weakly to moderately stable boundary layer (SBL),

with various combinations of:

- surface cooling (varying the surface heat flux from 0 to -0.5 mKs^{-1}),
- geostrophic winds (8, 10, 12 and 14 ms^{-1}).

By doing so, an LES database will be generated in order to compare to observational data. A thorough investigation of the LES results through profiles and turbulence statistics in neutral versus stable atmospheric conditions will be presented. Results will focus on the lower vertical part of the boundary layer (first 300 m above the sea surface), where wind turbines are placed.

For wind energy applications, neutral stability is usually the most important situation to consider, particularly when considering the turbulent wind loads on a turbine, since these are largest in strong winds. Moreover, design of wind turbine are carried out under this stability. Nevertheless, stable conditions can give rise to asymmetric loadings due to high wind shear. There can also be rapid changes in wind direction and wind height in this situation.

It is clear that the computational size of such a calculation is inevitably large and therefore computationally very expensive for practical day-to-day engineering calculations. However, with the rapid growth in computer technology, these kinds of calculations could be implemented as part of a normal workload in the not so distant future.

Comparison: Simulation results were verified against measurements. This comparison will help to better understand observations within the ABL as well as to assess the applicability of LES to wind energy.

This study is split into two major parts. In the first part, a qualitative comparison through vertical profiles (bulk flow properties) is carried out for neutral and weak-moderate stable cases simulated. Three parameters of importance in wind energy applications are considered,

namely vertical wind shear, wind direction and turbulence intensity. This comparison will rely on the three sonic anemometers available on the FINO1 mast.

In the second part and in order to further understand the LES approach, a statical analysis will be performed through the selection of a representative neutral case from FINO1 database. In this study, wind spectra, probability density functions and autocorrelations will be studied. Moreover, a brief investigation of the ability of LES data to solve short-term extreme wind events (wind gusts) will be carried out.

LES application: Finally, LES simulations which provide unprecedented temporal and spatial resolution information across the turbine rotor span are used to investigate the relative percentage error when using an approach based on one-point measurements as representative of the whole rotor area. Different combinations of rotor size, hub height and wind speed will be studied.

Summarizing, the outline of this Ph.D. thesis is as follows. Following the introduction, in Chapter 2, a general overview is given, including a description of the Atmospheric Boundary Layer and its turbulent structure, as well as the numerical methods used to study it. In Chapter 3, the offshore dataset is described extensively and the dependence of wave age on surface stress is analyzed. Subsequently, LES simulations of neutrally and stably stratified marine atmospheric boundary layers are carried out in Chapter 4. In Chapter 5, a comparison between the LES simulations and the FINO1 dataset is made. In Chapter 6, an LES application concerning the error committed when using a single point at hub height as representative of the whole rotor diameter is presented. Finally, concluding remarks are summarized in 7, as well as suggestions for future work.

Chapter 2

General Background

In this Chapter, a general description of the Atmospheric Boundary Layer (ABL) as well as its turbulent structure is given and the major differences over land and sea are summarized. Moreover, the numerical methods used to study it are outlined. Note that specific theoretical information is given separately in each chapter whenever necessary, here only the most relevant concepts will be introduced to establish a framework for the study. Further information can be found e.g. in [Stull \(1998\)](#); [Kaimal and Finnigan \(1994\)](#); [Arya \(2001\)](#).

2.1 Atmospheric Boundary Layer

There are many definitions of Atmospheric Boundary Layer (ABL). In [Stull \(1998\)](#), for instance, it is defined as '*that part of the troposphere that is directly influenced by the presence of the earth's surface, and responds to surface forcing with a time scale of about an hour or less (due to the mechanisms of turbulence)*'. This forcing includes frictional drag, evaporation, heat and pollutants transfer and modification of the flow due to the bottom surface.

Since turbulence is characteristic of the ABL, the top of the ABL is often defined as the height where turbulence disappears. The height of the ABL and the scale of turbulence are greatly dependent on thermal stratification. At times, often in late afternoon and under conditions of strong winds, turbulence is not generated by surface heating but is mainly generated mechanically (by the wind gradient). The stratification can then be said to be neutral (NBL). During the day, surface heating drives large thermal motions, that steadily increase the boundary layer height sometimes to heights of 3000 m in the late afternoon. The stratification is said to be unstable. During the night, turbulence

is usually generated by shear and destroyed by negative buoyancy and viscosity. Because of this competition between shear and buoyancy effects, the strength of turbulence in the stable boundary layer (SBL) is much weaker in comparison to the neutral and convective boundary layers. As a result, the stable boundary layer is also much shallower (typical boundary layer height is of the order of 100 m or less) than the neutral (NBL) or convective boundary layer (CBL, typically of the order of 1000 m).

At the top of the ABL, the wind speed equals the wind speed of the free atmosphere (the geostrophic wind) while on the ground, surface friction reduces the air speed to zero. Due to the balance of pressure, friction and Coriolis forces, wind speed and direction change throughout the ABL. In the bottom 10% of the ABL, turbulent fluxes can be considered constant and Coriolis forces are unimportant: turning over of the wind with height is negligible here. This layer is called the surface layer (SL). The SL is directly influenced by roughness elements like grass and trees, which cover the surface of the earth, and most structures of engineering interest are located in the surface layer. Above the SL, lies the outer layer, which can be considered to be independent of surface conditions but is influenced by the rotation of the earth.

2.1.1 Peculiarities of the Marine Boundary Layer

Compared to the boundary layer over land, the offshore Marine Atmospheric Boundary Layer (MABL) is significantly less well researched. The reasons for this lie mainly in the the scarcity of data sets available over the sea which tend to be limited in duration. Properties of the MABL differ in many respects from that over land surfaces ([Petersen et al. 1998](#)). The differences are mainly due to the generally lower surface friction, leading to small vertical wind gradients and thus small turbulence intensities; more importantly, the influence of humidity in the near surface (with a typical relative humidity of 70-100%); and, to a large extent, the absence of the diurnal cycle of the boundary layer due to the large heat capacity of water (meaning that it can absorb large amounts of heat from the sun with relatively little temperature change).

Stability conditions are also different from inland. Under offshore conditions, the neutral boundary layer can exist during long period, when the ocean surface, and the air flowing above it, have nearly the same temperature (air-sea temperature differences tend to be small, except near coastlines). In this regime, turbulence is generated only by mechanical shear at the lower boundary, there is

no gravitational suppression of turbulence. In contrast, the boundary layer becomes stably stratified whenever the underlying surface is colder than the air. This is usually attributed to warm air advection from land over cold water.

The favourable wind resource offshore is mainly caused by the low surface roughness over water areas. Contrary to land conditions, the sea surface roughness is not constant with wind speed but depends on the wave field present. This in turn is governed by the momentum exchange process between wind and waves, which depends on wind speed, water depth, fetch (distance to coast), atmospheric stability, etc.

MABL can be schematically divided into three sublayers (Sjöblom and Smedman 2003): (1) the wave sublayer in which the flow is heavily influenced by single waves, (2) the surface or constant-flux sublayer where the flow is horizontally homogeneous and no longer disturbed by the presence of single waves and where we expect to find vertically constant turbulent fluxes and the validity of the logarithmic wind profile and (3) the Ekman sublayer where the roughness influence of the underlying surface decreases with height, the wind speed only increases weakly with height, and a small turning of the wind takes place (see Fig. 2.1).

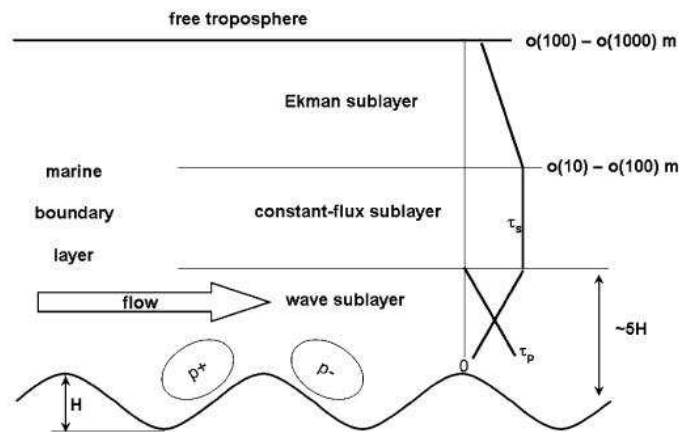


Figure 2.1: Vertical structure of the marine boundary layer. p_+ and p_- indicate positive and negative pressure deviations which lead to a driving force p on the waves. Schematic profiles of the shear stress, τ_s , and the pressure drag on the waves, τ_p , and typical height intervals are given on the right-hand side (source: (Emeis and Türk 2009)).

2.2 Turbulence

This research focusses mainly on the lower part of the boundary layer where wind turbines are placed and therefore where turbulence plays an important role in the flow structure. For that reason, it is worth devoting a section to this issue which serves as groundwork for the following chapters.

Turbulence or turbulent flow, the gustiness superimposed on the mean, although difficult to define, can be visualized as consisting of irregular swirls of motion called **eddies**. Usually turbulence consists of many different sized eddies superimposed on each other. Most of the boundary layer turbulence is generated by forcing from the ground and, far from the mean value (where transport quantities such as moisture, heat, momentum and pollutants determine the horizontal movement), turbulence is responsible for vertical transport.

Several characteristics describing turbulent motion are:

- *Unpredictability*: Turbulent flows are random and chaotic. This renders a deterministic approach impossible, and statistical methods must be relied on.
- *Nonlinearity*: The nonlinear terms in the governing Navier-Stokes equations lead to vortex stretching and the production of turbulence.
- *Large Reynolds numbers*: Turbulence develops in laminar flow (not turbulent) when Reynolds numbers become large (i.e. in atmospheric flows). The Reynolds number is defined in Eq. 2.1 where U_c and L_c are the characteristic velocity and length scales of the flow respectively, and ν is the fluid viscosity.

$$Re = \frac{U_c L_c}{\nu} \sim \frac{\text{inertial forces}}{\text{viscous forces}} \quad (2.1)$$

- *Diffusivity or ability to mix*: Due to its unsteady, chaotic motion, turbulence induces rapid mixing and increased rates of transfer of momentum, heat and mass.
- *Three-dimensionality and rotationality*: Turbulent flows contain fluctuating vortex structures called eddies. The size of these structures range from the order of the flow size (large structures) to the size of the dissipating eddies (small structures). As a result, there is a large continuous range of structure sizes that exist in turbulent flows.
- *Dissipation*: Turbulent flows produce increasingly large velocity gradients that are eventually dissipated by viscosity. Therefore, all turbulent flows are dissipative. As a result of dissipation,

energy must be continuously supplied to maintain turbulence. The energy supply is provided by the large-scale flow and eddy structures.

For the governing equations of turbulent motion, please refer to section 4.2.1 in chapter 4.

2.2.1 Eddies and Scales of Motion

As described earlier, boundary layer turbulence is generated on a variety of scales. Turbulent flow consists of a hierarchy of eddies of a wide range of sizes (length scales), from the smallest that can survive the dissipative action of viscosity to the largest that are allowed by the flow geometry. The range of eddy sizes increases with the Reynolds number of the overall mean flow. In particular, for the ABL, the typical range of eddy sizes is 10^{-3} to 10^3 m in diameter.

Amongst the wide and continuous range of scales in a turbulent flow, a few have special significance and are used to characterize the flow itself. One is the characteristic *large-eddy scale* or macroscale of turbulence, which represents the length (l) or time scale of eddies receiving the most energy from the mean flow. Another is the characteristic *small-eddy scale* or microscale of turbulence, which represents the length (η) or time scale of most dissipating eddies. The ratio l/η is found to be proportional to $Re^{3/4}$ and is typically 10^5 (range: $10^4 - 10^6$) for atmospheric PBLs.

The macroscale, or simply the scale of turbulence, is generally comparable to the characteristic scale of the mean flow, such as boundary layer thickness or channel depth, and does not depend on the molecular properties of the fluid. On the other hand, the smaller scales depend on the fluid friction (viscosity) ν , as well as on the rate of energy dissipation ϵ . Dimensional considerations further lead to the defining relationship,

$$\eta = (\nu^3/\epsilon)^{1/4} \quad (2.2)$$

Under stationary or steady-state conditions, the rate at which energy is dissipated is exactly equal to the rate at which energy is supplied from the mean flow into turbulence. This leads to an inviscid estimate for the rate of energy dissipation $\epsilon = u_l^3/l$, where u_l is the characteristic velocity scale of turbulence (large eddies), which can be defined in terms of the turbulence kinetic energy as $u_l = \sqrt{TKE}$.

2.2.1.1 The Energy Cascade

One of the fundamental concepts of turbulence is a description of the transfer of energy among different scales or eddy sizes. It has been recognized for a long time that in large Reynolds number flows, almost all the energy is supplied by the mean flow to large eddies, while almost all of it is eventually dissipated by small eddies. The transfer of energy from large (energy-containing) to small (energy-dissipating) eddies occurs through a cascade-type process involving the whole range of intermediate size eddies (Richardson 1922). The existence of the energy cascade is clearly demonstrated in the form of a turbulent energy spectrum (depicted in Fig. 2.2). The energy spectrum describes the relative amount of kinetic energy that each turbulent scale contributes to the total turbulent kinetic energy. Fig. 2.2 illustrates that the majority of energy is contained in the large-scale structures (of order l), and that energy is transferred down through the inertial subrange, to smaller scales (η) via Kolmogorov's theoretical $-5/3$ power-law for isotropic, three-dimensional turbulence.

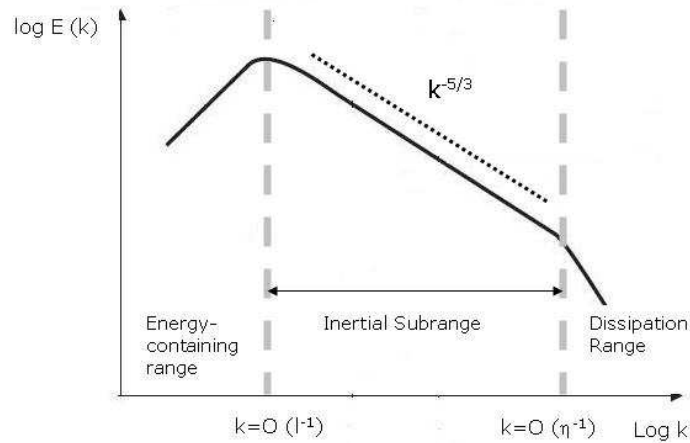


Figure 2.2: Sketch of the theoretical spectrum for three-dimensional turbulence.

If the large-eddy Reynolds number $Re_l = u_l l / \nu$ is sufficiently large, these large eddies become dynamically unstable and produce eddies of somewhat smaller size, which themselves become unstable and produce eddies of still smaller size, and so on further down the scale. This cascade process is terminated when the Reynolds number based on the smallest eddy scales becomes small enough (of the order of one) for the smallest eddies to become stable under the influence of viscosity. This qualitative concept of energy cascade provides an underpinning for subsequent theoretical ideas, as well as experimental studies of turbulence.

Following the above reasoning, Kolmogorov (1941) proposed his local isotropy hypothesis, which states that at sufficiently large Reynolds numbers, small-scale structure is locally isotropic whether

large-scale motions are isotropic or not. Here 'local' refers to the particular range of small-scale eddy motions that may be considered isotropic. The concept of local isotropy has proved to be very useful in that it applies to all turbulent flows with large Reynolds numbers. It also allowed the sufficiently well-developed statistical theory of isotropic turbulence to be applied to small-scale motions in most turbulent flows encountered in practice. The condition of sufficiently large Reynolds number is particularly well satisfied in the atmosphere. Consequently, the local isotropy concept or hypothesis is found to be valid over a wide range of scales and eddies in the atmosphere. For locally isotropic, small-scale turbulence, Kolmogorov (1941) proposed a local similarity theory or scaling based on his well-known equilibrium range hypothesis. This states that at sufficiently high Reynolds numbers, there is a range of small scales for which turbulence structure is in statistical equilibrium and is uniquely determined by the rate of energy dissipation (ϵ) and kinematic viscosity (ν). Here, statistical equilibrium refers to the stationarity of small-scale turbulence, even when large-scale turbulence may not be stationary.

The above two parameters led Kolmogorov to propose the following microscales from dimensional considerations:

$$\eta = (\nu^3/\epsilon)^{1/4} \quad (2.3)$$

$$v = (\nu\epsilon)^{1/4} \quad (2.4)$$

2.3 Numerical Simulation

Field measurements and simulation methods (e.g. numerical, laboratory tank, wind tunnel) are two main directions of research in PBL. Field measurements have a long history in research since they measure the 'real' atmosphere. Although one of the disadvantages is that, in field measurements, a combination of many simultaneous complex effects and processes are involved and it is very difficult to isolate them in order to focus on individual processes such as turbulent processes. In the past decades, numerical simulation has become another popular method for tackling turbulence issues. However a combination of both (field measurements and numerical simulations) are essential for addressing PBL studies.

Numerical simulations have several valuable advantages. They are less expensive and easier to handle than a programme in the field. They provide four-dimensional (spatial and temporal) fields of flow characteristics under well-controlled external conditions. They are more accessible in the sense that numerical simulations can be setup under conditions where field measurements would

be difficult. Moreover, they are very helpful for conceptualizing our understanding of environmental processes and offer the possibility of doing sensitivity studies by changing certain physical parameters, and then studying the effects. Indeed, one or another physical process can be easily excluded from consideration in numerical studies. Thus, the role of different processes can be clearly identified (Esau 2003).

Three main approaches are now in use for the computation of turbulent flows, Direct Numerical Simulation (DNS), Large-Eddy Simulation (LES), and a statistical approach based on the Reynolds Averaged Navier-Stokes (RANS) equations.

A technique used in the simulation of turbulence is **Direct Numerical Simulation (DNS)** which became popular in the 1980s. The full, time-dependent Navier-Stokes equations are solved numerically, essentially without any approximations other than numerical discretizations whose errors can be estimated and controlled. This is the most accurate approach. This method does not require any modelling and all the motions contained in the flow are resolved. These results can be used to produce statistical information. In a direct numerical simulation, all of the kinetic energy dissipation, which occurs on the smallest scales, is captured. The size of the grid must not be larger than the viscosity scale, called the Kolmogorov scale, η (the smallest fundamental turbulent length scale). If L_d is the characteristic length of the physical domain, the number of points in one direction should be of the order:

$$N \sim \frac{L_d}{\eta} \quad (2.5)$$

where $\eta = (\nu^3/\epsilon)^{1/4}$ is the Kolmogorov length scale. The dissipation per unit mass can be approximated as $\epsilon \sim \nu^3/L_d$ where u is the characteristic velocity of the flow. Finally the number of points for a DNS resolved in three dimensions can be estimated as:

$$N \sim \left(\frac{L_d}{\eta}\right)^3 \sim \left(\frac{uL_d}{\nu}\right)^{\frac{9}{4}} = Re_e^{\frac{9}{4}}, \quad (2.6)$$

so that for its usage in ABL flows ($Re_e \sim 10^8$), the number of computational cells necessary, combined with the small numerical time step required to capture the fastest turbulent structures, simply makes the computational cost too high (expressed both in terms of CPU time and variable storage). Obviously in practise DNS is restricted to relatively low Reynolds number.

A less expensive technique is called **Large-Eddy Simulation (LES)**. Here, the large scales of the flow are computed explicitly, as in DNS the approach, while the effect of the small scales on the

large scales is modelled. The justification for such a treatment is that the larger eddies contain most of the energy whereas the smaller eddies are more universal and easier to model. To separate the large from small scales, LES is based on the definition of a filtering operation. Similarly to DNS, LES provides a three-dimensional, time-dependent solution of the Navier-Stokes equations.

The traditional approach to the Navier-Stokes equations was to reduce them to the so-called **Reynolds-Averaged Navier-Stokes (RANS)** equations. According to this strategy only averaged quantities which describe the mean flow are solved and the effect of the unsteadiness in the flow due to turbulence is accounted for by a turbulence closure model. So far, RANS is the most frequently used tool used in wind energy applications. According to the RANS approach to turbulence, all of the unsteadiness is averaged out by time-averaging the NS-equations. By doing so, the computational time is reduced. While the small scales are more or less universal, the large scales are affected very strongly by the boundary conditions. The complexity of turbulence makes it impossible for a single RANS model to represent all turbulent flows. Some adjustment of the constants is often required. Parametrizations are very sensitive to large-eddy structures which depend on environmental conditions such as geometry and stratification. Parametrizations are not valid over a wide range of different flows and are not suitable for detailed turbulence studies.

Fig. 2.3 gives a schematic view of the frequency ranges resolved or modelled by the various approaches introduced earlier by plotting the turbulence spectrum.

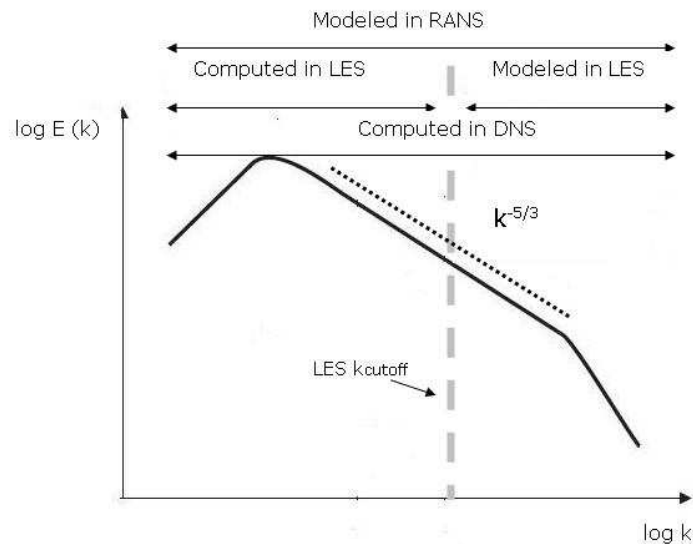


Figure 2.3: Turbulent scales resolved/modelled by RANS, LES and DNS.

Note that, although the set of equations for the RANS and LES approaches are very similar, the main difference lies in the averaging procedure and thus in the meaning of the subgrid stress tensor. Whereas RANS models apply a temporal Reynolds number averaged over a large scale compared to the characteristic scale of temporal fluctuations, LES models apply a spatial filter over quite a small scale compared to characteristic length scales. So the RANS Reynolds stress tensor expresses the momentum flux of all turbulent fluctuations and the entire spectrum of turbulence must be modelled.

Chapter 3

The Offshore Environment According to FINO1 Observations

3.1 Introduction

This Chapter is devoted to the analysis of observational data. Here, a two year high quality dataset from an offshore platform (FINO1) located 45 km off Borkum island in the North Sea are used. The data are unique so far as combining atmospheric and oceanographic information thereby providing an excellent opportunity to get a better understanding of Marine Atmospheric Boundary Layer (MABL) processes.

First, rigorous quality control and pre-processing operations are performed on the data following the suggestions of several authors ([Højstrup 1993](#); [Foken and Wichura 1996](#); [Mauder and Foken 2004](#); [Burba and Anderson 2007](#); [Vickers and Mahrt 2006](#)). Various corrections to account for mast shadow, tilt correction and heat flux humidity correction are applied extensively. Doing so, a robust dataset for further statistical analysis and comparison with LES performance is ensured. Moreover, some parameters such as friction velocity, sensible heat flux, atmospheric stability and wave age are derived which will help later on to give a global view of the database. Finally, the dependence of wave age on surface stress is also investigated.

This Chapter is organized as follows. After a short summary of the state of the knowledge of wave age dependence on surface stress has been presented in Section [3.2](#), a brief review of the theoretical background is given in Section [3.3](#). A description of measurements together with the

pre-processing applied to the data are covered in Section 3.4. Next, the dependence of wave age on surface stress is analyzed. Finally, a summary is presented in Section 3.6.

3.2 State of Knowledge on the Dependence of Wave Age on Surface Stress

The analysis of sea surface shear stress in terms of drag coefficient has been the subject of considerable theoretical and experimental effort during the last decades, because wind stress is a major process controlling exchanges at the air-sea interface.

Knowledge of vertical momentum exchange processes over the open sea is therefore relevant for a better understanding of the Marine Boundary Layer (MBL) and essential not only to improving the parameters used in atmospheric numerical models but also in other applications such as wind energy harvesting, due to its direct relation to wind condition. In recent years, the interest in offshore wind farms has been growing, with several wind farms of a few thousand megawatts being installed at sea. To estimate the expected power output from these wind farms, a correct description of the sea surface roughness is required [Myrhaug and Slaattelid \(1999\)](#); [Frank and Larsen \(2000\)](#).

The standard parametrization of the surface stress over the ocean was introduced by [Charnock \(1955\)](#). Based on a dimensional analysis, he proposed a surface roughness given by:

$$z_0 = z_{Ch} \frac{u_*^2}{g}, \quad (3.1)$$

where the Charnock parameter, z_{Ch} , was assumed to be constant, z_0 is the aerodynamic roughness length, u_* is the friction velocity and g is the acceleration of gravity. Even today, most models of the atmosphere still use the assumption that the Charnock parameter remains constant when calculating the surface stress over the ocean. Various field measurements showed that this concept works well for open ocean sites, except at very low wind speeds ($< 3\text{--}4 \text{ ms}^{-1}$). Based on a theoretical investigation, [Kitaigorodskii and Volkov \(1965\)](#) suggested that the Charnock parameter was dependent on sea-state, yielding larger values for young seas than for old wind seas, i.e. a surface dominated by shorter waves extracts momentum from the atmosphere more effectively than a surface dominated by swell. Some observational evidence of this was later obtained by [Donelan \(1982\)](#). Since instruments for measuring winds were, for a very long time, too slow to resolve high frequency turbulent fluctuations, early observational investigations of sea-surface momentum exchange were

usually based on the inertial dissipation method ([Edson et al. 1991](#)). Here, the turbulent kinetic energy budget is assumed to be governed by a balance between shear production and dissipation. In the presence of growing (or decaying) waves, a vertical energy flux term enters the equation, due to a correlation between pressure and the vertical velocity perturbations induced by the wave field. [Janssen \(1999\)](#) demonstrated that the omission of this term in the inertial dissipation method may lead to an underestimate of the wave effect on air-sea fluxes.

In recent years, sonic anemometers which measure wind speed with very high resolution in time have become available, enabling direct calculations of momentum fluxes using the eddy correlation technique. Here, no pre-assumption on energy balance is needed. Several authors claim to see an impact of sea-state on observations using this method ([Brut et al. \(2005\)](#); [Drennan et al. \(2003, 2005\)](#)).

At present, most of the effort is focused on: (i) understanding the nature of these exchanges, and (ii) deriving a reliable and accurate parameterization of surface turbulence. Indeed, in atmospheric modelling, the drag coefficient which is generally estimated from the bulk formula does not account for the influence of wave age. Several field experiments have been conducted with the aim of searching for a universal relationship between sea surface roughness and different wave field properties (e.g., the Marine Remote Sensing (MARSEN) program (([Geernaert et al. 1987](#)), the Humidity Exchange over Sea (HEXOS) program in the North Sea, the HEXOS Main Experiment (HEXMAX) off the Dutch coast ([Smith et al. \(1992\)](#), the Risø Air Sea Experiment (RASEX) in Denmark ([Vickers and Mahrt \(1997\)](#))). However, despite these studies, controversy remains over the nature of the relationship between wind, sea state, and drag or roughness. In the book by [Csanady \(2001\)](#) (page 28), he refers to [Yelland et al. \(1998\)](#) and [Dobson et al. \(1994\)](#) as examples of observational studies where no impact of sea-state was observed. We take this as evidence that more observational studies are needed before this dispute can be finally settled.

3.3 Theoretical Background

In the stationary and homogeneous atmospheric surface layer (typically the lower 10% of the boundary layer), the Monin-Obukhov Similarity Theory ¹ (Monin and Obukhov 1959) postulates that the nondimensional vertical wind shear is a function of the stability parameter $\zeta = zL^{-1}$ only:

$$\frac{\kappa z}{u_*} \frac{\partial U}{\partial z} = \phi_m \left(\frac{z}{L} \right), \quad (3.2)$$

where L is the Obukhov length which is the height at which buoyancy and shear produce turbulence in equal measures and is defined as:

$$L = - \frac{u_*^3 \theta_0}{\kappa g \overline{w' \theta'}}, \quad (3.3)$$

where $\kappa = 0.4$ is the von Kàrman constant, g is the acceleration due to gravity ($g = 9.81 \text{ m s}^{-2}$), z is the height above the surface, U is the magnitude of the horizontal wind speed ($U = (\overline{u^2} + \overline{v^2})^{1/2}$), ϕ_m is a stability function which relates vertical wind shear to stability (and must be obtained empirically), u_* is the friction velocity, defined by:

$$u_* = \left(\overline{u'w'^2} + \overline{v'w'^2} \right)^{1/4}, \quad (3.4)$$

and θ_0 is the potential temperature and $\overline{w' \theta'}$ represents the turbulence covariance between the fluctuating temperature and the vertical velocity, which is a measure of the sensible heat flux.

Often, Eq. 3.2 is integrated within the surface layer assuming the turbulent fluxes are height-invariant to obtain the integrated form of the wind profile:

$$U(z) = \left(\frac{u_*}{\kappa} \right) \left(\log \left(\frac{z}{z_0} \right) - \psi_m \left(\frac{z}{L} \right) \right), \quad (3.5)$$

where ψ_m is now the integrated stability function which can be related to ϕ_m or rather obtained from measurements and z_0 is an integration constant called the roughness length (the height above

¹Similarity theory provides a way of organizing and grouping the variables of interest in dimensionless groups. This procedure is helpful in gaining a better understanding of fluid-dynamics phenomena and provides guidelines for correct scaling in experimental facilities. A proper choice of dimensionless groups should allow to establish 'universal' relationships between groups, valid for each condition, which can be represented in graphs, numerical tables or regression curves.

ground level at which wind speed is theoretically zero, $U(z_0) = 0$). Thus, if the wind speed is known at a particular height, the vertical wind speed profile is determined by two parameters: the surface roughness z_0 and the Monin-Obukhov length L .

It is worth mentioning that this theory is commonly used in wind energy applications for extrapolation of measurement data to hub height.

The exact empirical formulation of the integrated stability functions seem to be still controversial [Højstrup \(1988\)](#). In the current study, the [Dyer \(1974\)](#) formulation for the stable surface layer ($zL^{-1} > 0$) and [Paulson \(1970\)](#) formulation for unstable surface layer ($zL^{-1} < 0$) are used:

$$\psi_m = \begin{cases} 2 \log \left(\frac{1+x}{2} \right) - \log \left(\frac{(1+x)^2}{2} \right) + 2 \arctan(x) + \frac{\pi}{2} & \text{for } \frac{z}{L} < 0 \\ -\beta \frac{z}{L} & \text{for } \frac{z}{L} > 0 \end{cases} \quad (3.6)$$

where $x = (1 - \gamma \frac{z}{L})^{1/4}$ and the constants $\beta = 5$ and $\gamma = 16$.

Usually, measurements of the friction velocity (u_*) or wind stress ($\tau = -\rho u_*^2$) are not available and therefore the wind stress is parametrized as a product of the mean wind and surface exchange coefficient (C_z) as:

$$|\tau| = -\rho u_*^2 = \rho C_z U(z)^2, \quad (3.7)$$

where the surface drift speed was assumed to be zero, C_z is the exchange coefficient at the reference height z and ρ is the density of air. Usually and for practical reasons, the exchange coefficient at a 10 m height is used for C_{10} . Eq. 3.7 is a common parameterization used in numerical models to calculate the air-sea surface fluxes between the atmosphere and the ocean and therefore it is important to determine accurately the exchange coefficient (C_z).

In the neutral surface layer ($L \rightarrow \infty$ and $\psi_m = 0$), the exchange coefficient related to a 10 m height (C_{N10}) can be written as a function of the surface roughness alone. From Eq. 3.5 and Eq. 3.7, it follows that,

$$C_{DN} = \left(\frac{u_*}{U_{10N}} \right)^2 = \frac{\kappa^2}{(\ln(\frac{10}{z_0}))^2}. \quad (3.8)$$

Here z_0 is obtained from Eq. 3.5 for neutral stability using measurements of U_{10N} and friction velocity as:

$$z_0 = 10 \cdot \exp\left(-\frac{U_{10N} \cdot \kappa}{u_*}\right). \quad (3.9)$$

Therefore, under neutral stratification, there is a one-to-one relation between the drag coefficient C_{DN} and the roughness length z_0 . So specifying the roughness specifies the drag coefficient and vice versa.

3.4 Measurements

3.4.1 Measurement Site

The FINO1 station (Fig. 3.1) is a 100 m high mast located 45 km off Borkum island (lat. $54^{\circ}0.87'N$, long. $6^{\circ}35.24'E$) in the North Sea and performs continuous multilevel measurements of the lower part of the atmospheric boundary layer as well as oceanographic measurements (Neumann et al. 2004). The measurements at the research platform are operated by DEWI GmbH². FINO1 was built mainly for wind energy applications, providing high quality data to cover investigations with a very broad scope. The location of the platform is far from the coast so that measurements represent the marine boundary (open sea) conditions (Lange and Tautz 2004).

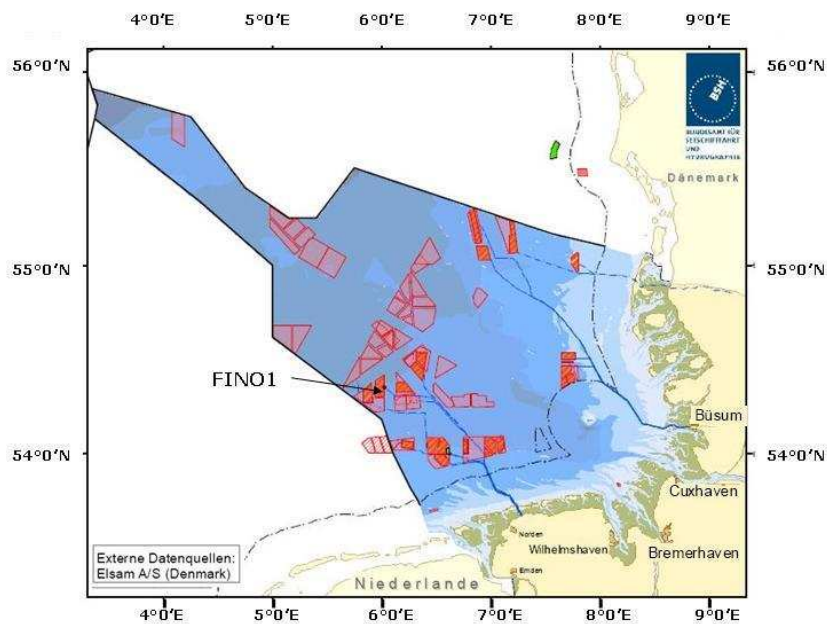


Figure 3.1: Location of the FINO1 platform. Shaded red areas represent wind farm projects (Source: www.bsh.de).

The mast is a bottom-mounted jacket construction with a lattice tower up to 100 m (water depth of 30m), providing a very stable platform which avoids data contamination by the motion of sensors. The reader is referred to (Neumann et al. 2004) for a detailed description of the data and collection procedures. Only a brief description of the measurement setup is provided here.

²DEWI-German Wind Energy Institute. <http://www.dewi.de>

Atmospheric data

In Fig. 3.2, the positions of the sensors for wind speed and wind direction are labelled with arrows. An array of identical cup anemometers are arranged on the South-East side facing away from the platform at eight different heights above the sea (every 10 m from 33.5 to 101.5 m). On the North-West side of the mast, SOLENT 1210R3-50 ultrasonic anemometers (Gill Instruments, Lymington, UK) are installed at intermediate heights (40 m, 60 m and 80 m). Wind direction is available from wind vanes at 30 m, 50 m, 70 m and 90 m. Fig. 3.3 shows a layout of boom locations. From the sonic signals, the three orthogonal components of wind (u , v , w) as well as the so-called 'sonic temperature' are obtained. In addition, other sensors measure standard meteorological parameters such as temperature (30 m, 40 m, 50 m, 70 m and 100 m), humidity (100 m, 50 m and 33 m), air pressure (100 m and 20 m) and solar irradiation (33 m). Slow-response 'profile' instrumentation is sampled once per second (1 Hz) and stored as 10 min averages. Fast-response instrumentation is sampled with a frequency of 10 Hz.

In this work, a two year period (Jan. 2005 - Dec. 2006) is investigated and measurements from the sonic anemometers were used as the primary sources of data while slow response measurements were used when necessary. The eddy covariance method (EC-technique) is used to calculate the turbulent momentum fluxes ($\overline{u'w'}$ and $\overline{v'w'}$) and sensible heat flux ($\overline{w'\theta'}$) from the sonic measurements. This method is based on the Navier-Stokes equations of motion; after application of Reynold's averaging procedure which separates the mean $\bar{\phi}$ and fluctuating part (ϕ') of an atmospheric variable ϕ , such that ($\phi = \bar{\phi} + \phi'$). Prior to calculating the derived-quantities of interest, several tests and corrections were carried out as follows.

Before installation of the sonic anemometers to the mast, a three dimensional calibration was applied, based on wind tunnel measurements. This calibration took into account the dependence of the flow distortion for azimuth and elevation angle, as well as for wind speed (Lange and Tautz 2004). For wind speeds higher than 5 ms^{-1} , the sonic instruments underestimate the wind speed by between 0.5% and 2% (depending on instrument) and are largely independent of wind speed. To correct for the instrument offset, the wind speed has been multiplied by the relevant calibration factors (Lange and Tautz 2004).

The instantaneous measurements were compared to allowable upper and lower limiting values based on instrument manufacturing specifications and the prevalent weather over the North Sea.

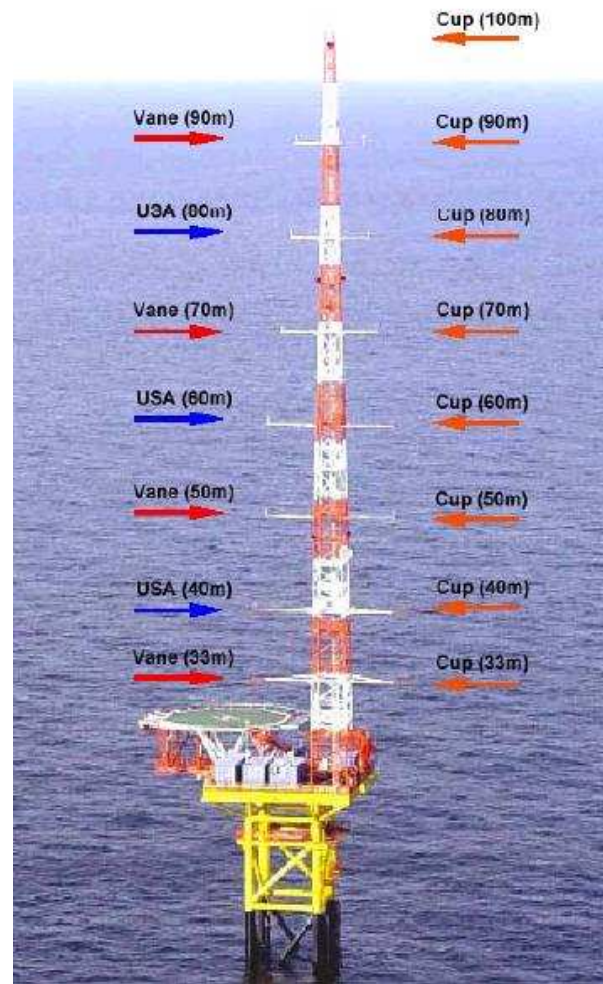


Figure 3.2: Field measurements on the FIN01 meteorological mast (source: www.fino-offshore.de).

Values exceeding those thresholds were discarded as instrumental errors. Temperature measurements exceeding 30°C and lower than -15°C were rejected. A maximum horizontal wind speed of 35 ms^{-1} was allowed, the vertical wind speed had to be between -15 ms^{-1} to 15 ms^{-1} . Furthermore, unreasonable peaks (unrealistically large or small values) associated with non-meteorological events in the data have been removed. The criterion was settled to remove signals that are no more than 5.5 times the standard deviation in a window with 30 minute averaging period in a similar way to that described in [Vickers and Mahrt \(1997\)](#).

Other effects influencing measurements are data trends. An increase in wind speed leads to a deviation from the mean value during the measurement interval, which is not produced by turbulence but is related to mesoscale events. In this work, the stationary nature of the data was analyzed by checking that the mean and standard deviation over a long time period used to calculate fluctuation

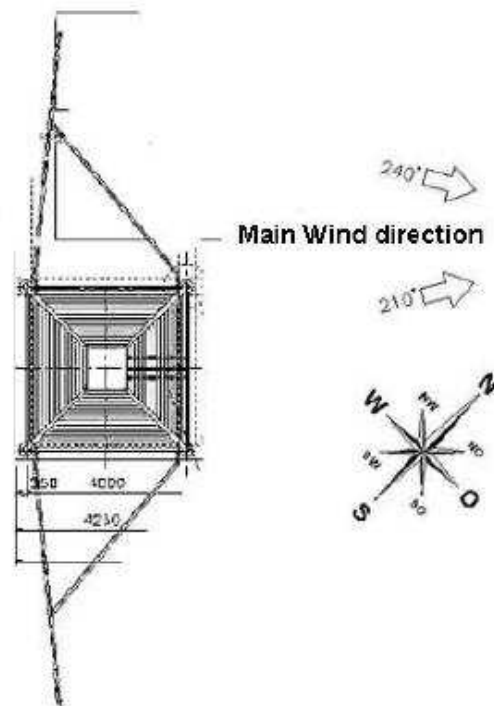


Figure 3.3: Layout of the measurement mast at FINO1 (source: www.fino-offshore.de).

variables, did not vary significantly in time. Non-stationarity has been corrected by using linear de-trending.

In order to isolate large-scale variations from turbulent ones, a simple method was employed averaging the quantities calculated over a period of 30 minutes (conventional averaging time used in many surface-air exchange investigations).

Correction of wind speed for flow distortion of the measurement mast

As pointed out by Högström (1987), the flow distortion produced when the wind comes from the mast (mast shadow) can be an important source of error in data post-processing. Here, direct measurements of mast shadow (from 90° to 180° for sonic and from 270° to 350° for cup anemometers) were discarded. As can be seen in Fig. 3.4 (left-side panel) the main wind direction on FINO1 is South-Westerly with additional high winds from the North-West, with little difference for height (not shown here) and therefore the percentage of data discarded is not too high. Mean wind speed over the period used was 9.26 ms^{-1} , 9.39 ms^{-1} and 9.85 ms^{-1} at 40 m, 60 m and 80 m respectively (Fig. 3.4 (right-side panel)).

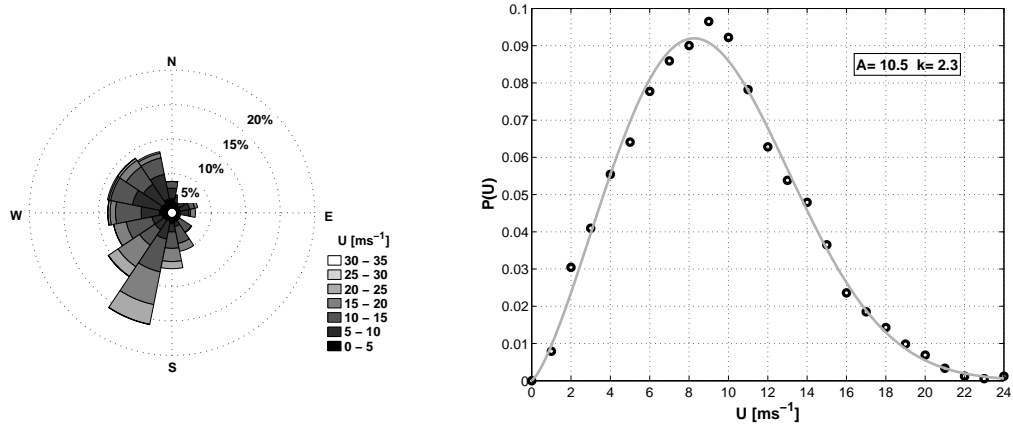


Figure 3.4: Wind direction distribution (wind rose) (left-side panel) and wind speed histogram (with fitted Weibull distributions) (right-side panel) at 40 m over the period analyzed.

However, outside the discarded range, the wind is influenced by the tower structure due to wake effects. A correction accounting for such an effect was applied as follows: The wake effect has been assumed to have a sinusoidal dependence on wind direction. Based on this assumption, the ratio between wind speed in sonic and cup anemometers can be expressed as:

$$\frac{U_s}{U_c} = \frac{U_{sm}(1 + a \sin(\phi + \delta_s))}{U_{cm}(1 + a \sin(\phi + \delta_c))} \quad (3.10)$$

where U_s and U_c are the corrected sonic and cup anemometer measurements (their ratio is ideally 1), while U_{sm} and U_{cm} are the measurements at the sonic and cup anemometers. The sinusoidal correction has the same shape amplitude (a) for both anemometers, since it is assumed that it is a function of the tower itself. The angles (δ_s and δ_c) and the amplitude of correction a is obtained by fitting Eq. 3.10 to the median ratio (of 10 min wind speed) between cup and sonic anemometer binned to 5° , where only wind speeds higher than 5 ms^{-1} were used. Note that this correction is applied to the original sonic (10 Hz) wind speed. This correction corrects for the mean wind speed, but not turbulence (tower-induced von Kàrman vortices), which could be additionally formed by the tower structure. The fit has been done for each anemometer separately (values of fitted parameters are given in Table 3.1).

Height	a	δ_s ($^\circ$)	δ_c ($^\circ$)
40	-0.0313	-30.70	129.23
60	-0.0338	-28.70	131.38
80	-0.0443	-31.40	128.80

Table 3.1: Parameters for the tower correction algorithm.

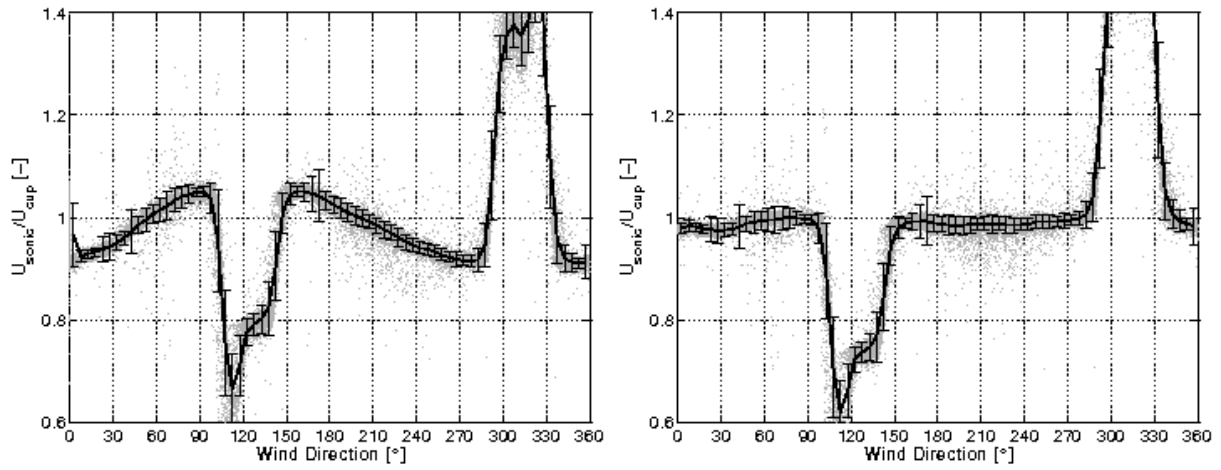


Figure 3.5: Sonic and cup anemometer wind speed ratio at 40 m as a function of wind direction before tower correction (right side of panel) and after tower correction (left side of panel). Data were binned to 5° and the errorbars represent one standard deviation.

The wind direction correction clearly shows the improvement to wind speed. Before the correction is applied, the ratio has clear directional dependence, while it is almost totally removed after correction (Fig. 3.5). At angles of around 90° and 320° , the sonic and cup anemometers are in the shadow of the tower, therefore the wind speed is underestimated over more than 30%. If the ratio of wind speed between sonic and cup anemometer is a measure of its uncertainty, the uncertainty at 40 m has improved from roughly 5% to 2% by applying the corrections. The other two levels which are not shown here have a similar behaviour.

Tilt correction

Prior to the flux calculation, a tilt correction based on the planar fit (PF) method (Wilczak et al. 2001) was applied, mainly to avoid contamination of the vertical wind speed by the horizontal wind speed.

Basically, the mean streamline field is compared to mean sonic measurements. For a tilted sonic, the mean streamline values \vec{u}_P (not yet rotated into the mean wind direction) can be obtained by multiplying the measured wind vector \vec{u}_m with a rotation matrix \mathbf{P} , which transforms the z-axis perpendicular to the plane of the mean stream coordinate system. A possible measurement offset \vec{c} of the sonic has to be considered. Thus, if the anemometer is then tilted, it can be written:

$$\vec{u}_P = \mathbf{P} \cdot (\vec{u}_m - \vec{c}) \quad (3.11)$$

The mean wind components are defined by:

$$\begin{aligned}\bar{u}_P &= P_{11} \cdot (\bar{u}_m - \bar{c}_1) + P_{12} \cdot (\bar{v}_m - \bar{c}_2) + P_{13} \cdot (\bar{w}_m - \bar{c}_3), \\ \bar{v}_P &= P_{21} \cdot (\bar{u}_m - \bar{c}_1) + P_{22} \cdot (\bar{v}_m - \bar{c}_2) + P_{23} \cdot (\bar{w}_m - \bar{c}_3), \\ \bar{w}_P &= P_{31} \cdot (\bar{u}_m - \bar{c}_1) + P_{32} \cdot (\bar{v}_m - \bar{c}_2) + P_{33} \cdot (\bar{w}_m - \bar{c}_3).\end{aligned}\tag{3.12}$$

The mean streamline coordinate system is defined to be aligned so that $\bar{w}_p = 0$. From Eq. 3.12 this yields:

$$\bar{w}_p = c_3 - \frac{P_{31}}{P_{33}}\bar{u}_m - \frac{P_{32}}{P_{33}}\bar{v}_m = b_0 + b_1\bar{u}_m + b_2\bar{v}_m.\tag{3.13}$$

Parameters b_0 , b_1 and b_2 are obtained by multiple linear regression. All components of P can be derived from these parameters, because of relations between the turning angles and the p coefficients as well as geometrical relations between the p and b coefficients. A detailed formula is given by (Wilczak et al. 2001).

This correction is important even at small tilt angles, since the horizontal wind speeds are an order of magnitude higher than the vertical speeds. The PF method constrains the mean vertical speed to be zero and, from this requirement, calculates the tilt angle. In our case, for each month and for each instrument, the tilt angles were calculated separately. The tilt angles show little variation with time, hence confident in the results is given and used the mean tilt angle from all 12 months for the correction. However, each instrument is separately mounted on the tower, therefore at each level, the tilt correction was done independently. On FINO1, the tilt angles were in the range 0.5° to 2° . Wilczak et al. (2001) also showed that the tilt errors are suspected to be largest for deep convective boundary layers, where wind shear is small. Since tilt angles are thought to be first order corrections, the data in these cases may be inaccurate.

Correction for humidity effects

Sonic anemometers do not really measure temperature but the speed of sound, which depends not only on air temperature but also to a minor extent on humidity. Therefore, in order to obtain the fluctuations of the actual temperature instead of the fluctuation of the sonic temperature, the humidity effect was corrected based on [Schotanus et al. \(2004\)](#):

$$\overline{w'\theta'} = \overline{w'\theta'_s} - 0.51\overline{w'q'}, \quad (3.14)$$

where $\overline{w'\theta'}$ is the kinematic heat flux, $\overline{w'\theta'_s}$ includes the humidity component and $\overline{w'q'}$ are the humidity vertical fluctuations.

Since the measurement of humidity did not have a fast response in the FINO1 data set, a bulk formulation was used to determine the second term on the right side in Eq. 3.14 following [Rutgersson et al. \(2001\)](#). The reader is referred to ([Rutgersson et al. 2001](#)) for an analytical formulation. This correction leads to a decrease of about 11% in the sensible heat flux over the studied period. A correction for cross-wind contamination ([Kaimal and Gaynor 1991](#)) caused by signal deflection of the sound path in the instruments due to the vertical wind component, was not included in Eq. 3.14 because it is internally implemented for the sonic anemometers used in this study. The density distribution of the corrected surface heat flux ($\overline{w'\theta'}$) is shown in Fig. 3.6. The estimated accuracy of $\overline{w'\theta'}$ is about $\pm 5\%$.

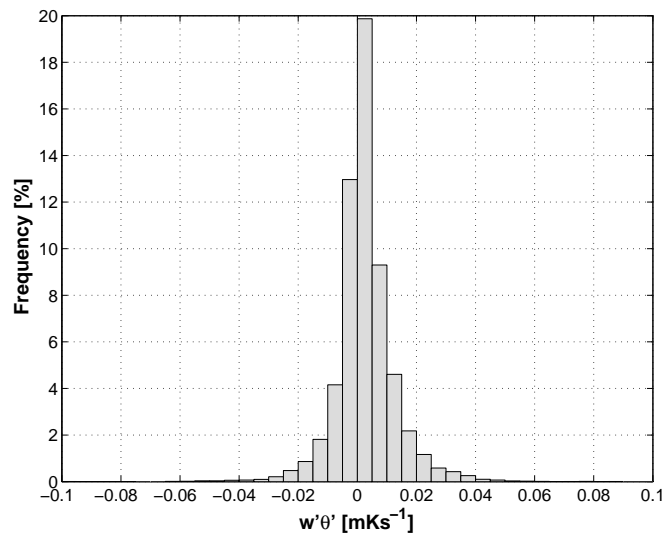


Figure 3.6: Probability distribution function of corrected $\overline{w'\theta'}$ over the study period.

The distribution exhibits an almost symmetric shape with a slight skew towards negative values, indicating heat flow towards the sea surface and stable surface layer conditions. A positive sensible heat flux indicates heat flow away from the sea surface and unstable surface layer conditions.

Once $\overline{w'\theta'}$ has been corrected, the Obukhov length (L) is calculated using Eq. 3.3. The condition for stability has been examined by mean of the $\zeta = zL^{-1}$ parameter (Fig. 3.7). Here the the criterion suggested by Højstrup (1988) of $|zL^{-1}| \leq 0.1$ to designate 'near-neutral' stratification is followed.

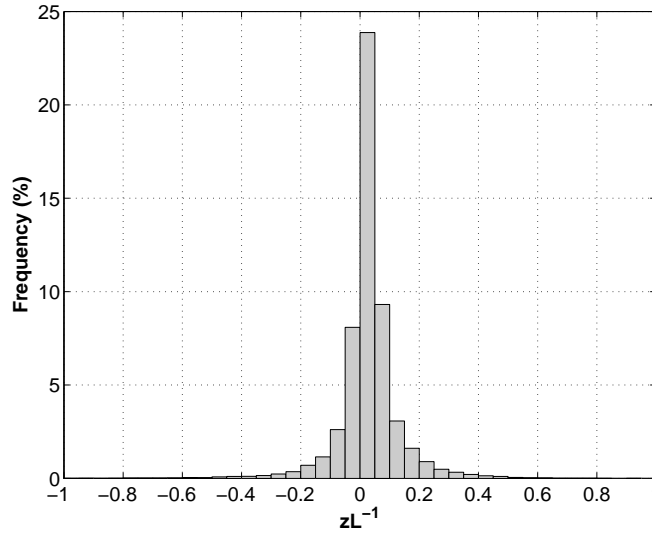


Figure 3.7: Frequency of occurrence (%) of the zL^{-1} stability parameter.

At FINO1, the boundary layer is often neutrally stratified (85% of time) with stable stratification for 10% of the time ($zL^{-1} > 0.1$) and unstable stratification for 5% of the time ($zL^{-1} < 0.1$). This behaviour can be attributed to the fact that FINO1 is about 45 km away from the coast and therefore the winds are not much influenced by the discontinuity of the coast (sea breeze).

The M-O theory predicts that the dimensionless wind shear defined in Eq. 3.2 is only a function of the stability parameter ($\zeta = zL^{-1}$) within the surface layer. For $\zeta = 1$ (neutrally-stratified BL), it is expected that $\phi_m = 1.0$. In Fig. 3.8 the non-dimensional wind profile derived with Eq. 3.2 from measurements at 40 and 60 m heights are plotted as a function of zL^{-1} together with the empirical curve given in Eq. 3.6 to provide a comparison. Very stable or unstable conditions with $zL^{-1} > 1$ or $zL^{-1} < -1$ were excluded from the analysis. In order to better compare the experimental results with the empirical curve (red dashed line), measured data were bin-median averaged (black solid line). A fair agreement is found between both curves and therefore the empirical relation (Eq. 3.6) is used for further calculations. The scatter in the data is considerable for $zL^{-1} > 0$ (stable stratification), which is probably related to the fact that, in stable cases, the measured levels do not

well represent the surface conditions. Other sources could be attributable to sampling variability and large scale contributions.

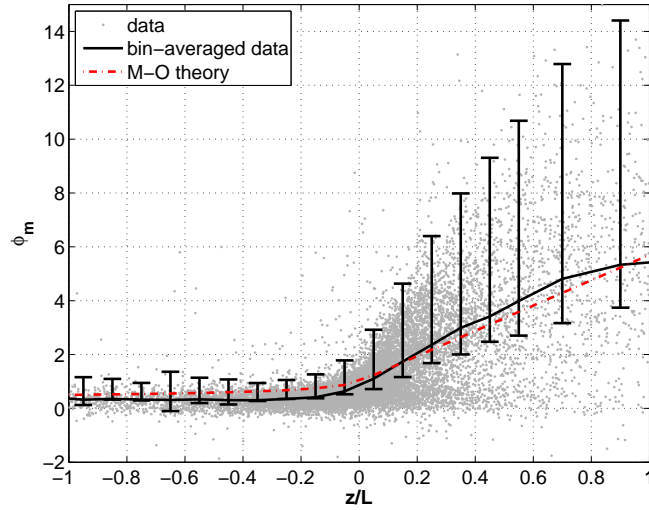


Figure 3.8: Non-dimensional wind shear (ϕ_m) versus stability parameter zL^{-1} . Mean values with error bars representing one standard deviation (solid black line). Red dashed line represents the empirical stability function given in Eq. 3.6.

It is well established that friction velocity depends on wind speed velocity over the sea. Fig. 3.9 shows the eddy correlation friction velocity (u_*) derived with Eq. 3.4 plotted against neutral wind speed at 10 m (U_{N10}) Eq. 3.5. Moreover, the best fit to the data set is plotted. It can be seen that a quadratic fit (solid line) follows reasonably well the trend in the data, however for values in the range of 5 ms^{-1} to 15 ms^{-1} a linear behavior is found (dashed line). Values of u_* were restricted to $u_* \geq 0.1 \text{ ms}^{-1}$.

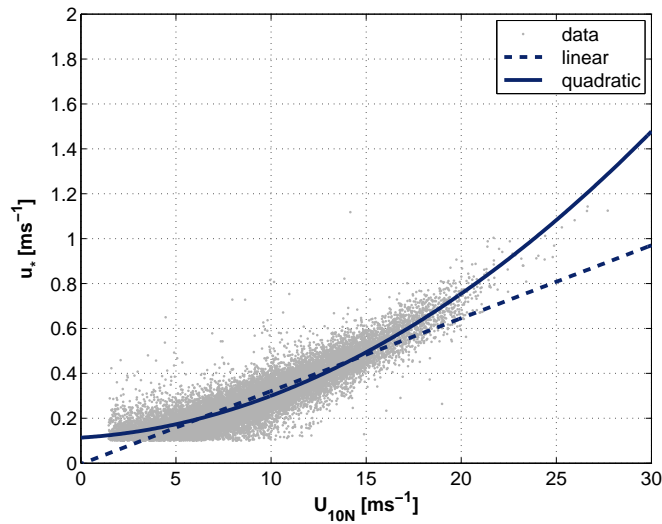


Figure 3.9: Eddy correlation friction velocity versus 10 m neutral wind speed.

Correction of wind stress measurement for elevation

Here, friction velocity (u_*) values have been corrected to surface values using the following expression derived by [Donelan \(1990\)](#):

$$u_{*s} = \frac{u_*(z)}{\sqrt{1 - \frac{\alpha_0 f_c z}{u_*(z)}}}, \quad (3.15)$$

where u_* is the friction velocity, f_c is the Coriolis parameter ($f_c = 1.181 \cdot 10^{-4} \text{s}^{-1}$ at 54° latitude) and $\alpha_0 = V_{gs}/u_*$ is assumed constant ($\alpha_0 = 12$) following [Donelan \(1990\)](#) with V_{gs} the component of the geostrophic wind normal to surface wind. The subscript s denotes atmospheric values at the surface. The uncertainty in friction velocity measurements was estimated to be about $\pm 10\%$.

Measurements from 40m to 10m were related using the common power-law profile ([Panofsky and Dutton 1984](#)):

$$U(z_2)/U(z_1) = (z_2/z_1)^\alpha, \quad (3.16)$$

where $U(z_1)$ and $U(z_2)$ are the wind speeds at heights z_1 and z_2 , respectively, with $z_2 > z_1$ and α is the power-law exponent that varies depending on the stability of the atmosphere.

For offshore conditions, the IEC standard ([IEC61400-1 2005](#)) considers a mean value of 0.14. At the FINO1 location, the mean value of the power law exponent α was found to be 0.024 over the period analyzed.

After all corrections and quality controls had been carried out, the data availability ranged from 61% to 82% at different heights for the sonic anemometers and about 85% for the profile data used in this study.

Oceanographic Data

Together with meteorological measurements, wave measurements are recorded continuously at the FINO1 location. Data from a wave rider buoy (WAVEC Datawell) moored at a distance of about 200 m from the platform are used. Data were provided by the German Federal Maritime and Hydrographic Agency (Bundesamt für Seeschifffahrt und Hydrographie, BSH). Parameters of special

interest to this study are the significant wave height (H_s), peak periods and mean wave directions, which were all derived from directional wave spectra. The scale accuracy of the sensor system is about 3%. The averaging period is 30 min.

The most important factors that control the wave growth are wind speed, wind duration and fetch. The dependence of wave height on the wind speed at FINO1 is shown in Fig. 3.10 over the period investigated.

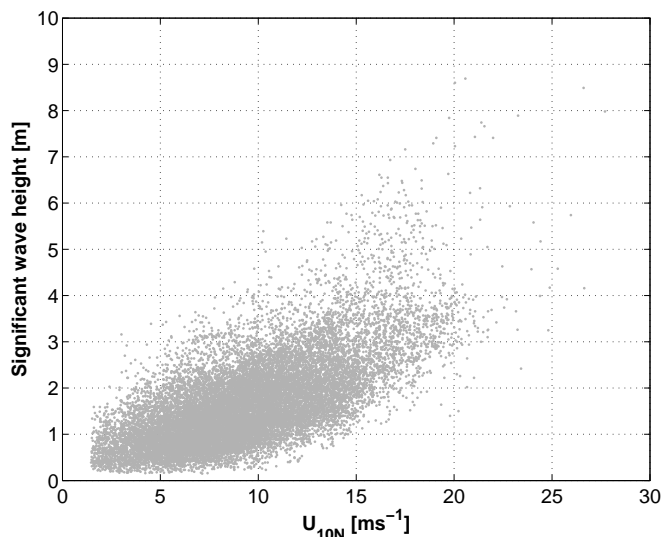


Figure 3.10: Significant wave height (H_s) versus wind speed at 10 m height and corrected for buoyancy effects.

As expected, wave height increases with increasing wind speed. The relatively large scatter could be associated with different weather situations at the same wind speed. The maximum observed significant wave height is 9.8 m.

When wind calms down and becomes slower than the wave propagation speed, it can no longer feed energy to the waves. Long waves that do not scale with the local wind are called swell, which include also those waves propagating from distant storms.

A frequently used parameter to describe the development of the wave field, the so-called wave age parameter, $C_p u_*^{-1}$, is plotted in Fig. 3.11, where C_p is the phase velocity of the dominant wave at the peak frequency in the wave spectrum and u_* is the friction velocity. For a young wind-sea, the dominant waves are in the high-frequency part of the spectrum, yielding relatively small values of the peak phase velocity compared to the boundary layer wind speed. In the case of a sea surface dominated by swell, the dominant waves propagate much faster compared to the wind speed resulting from large wave age values. Because of the relatively shallow water depth at the

measuring site, the general dispersion relation for inviscid water waves has been used to calculate the peak phase velocity:

$$\omega_p = \frac{2\pi}{T_p} = \sqrt{gk \tanh kh}, \quad (3.17)$$

where ω_p is the angular frequency of the dominant wave, T_p is the peak period, k is the wave number and h is the water depth. The dominant wave number, k , is calculated from Eq. 3.17. The peak phase velocity is then calculated as:

$$C_p = \frac{\omega_p}{k} \quad (3.18)$$

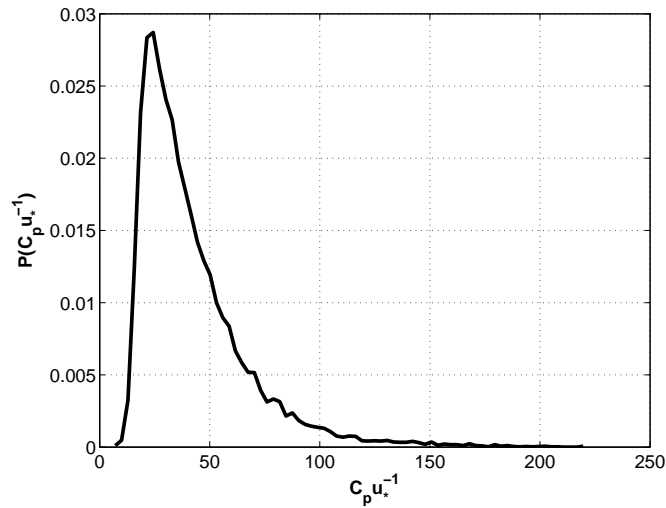


Figure 3.11: *Wave age probability density function.*

As can be seen from Fig. 3.11, 26% of the data have a wave age less than 21 (criterion used for wind waves), indicating a pure wind sea state and 74% of the data have a wave age higher than 21, indicating swell/mixed sea-state. Pure and dominant wind seas are frequent in coastal regions, and bounded seas, and during high wind events, but swell are generally presented in the open ocean (Drennan et al. 2003).

3.5 Results

The aim of this section is to investigate the functional dependence of sea state on the momentum transfer between the atmosphere and the sea surface. From Eq. 3.8, the drag coefficient (C_{10N}) and surface roughness (z_0) are interconnected under neutral conditions and therefore one can investigate the functional dependence with either variable. Here, both parameters are analyzed.

3.5.1 Relationship between Drag Coefficient and Sea State

Traditionally, the surface drag coefficient is calculated as a unique function of the surface wind speed (Large and Pond 1981). Here this relationship is investigated taking into account the state of the sea. To do so, the drag coefficient ($C_{DN} = (u_*/U_{10N})^2$) versus wind speed (U_{10N}) is plotted, both at 10 m and stability corrected to 'neutral' values as described earlier using a sea state criterion based on the wave age parameter.

Here, the criterion for sea state is based on the wave age parameter ($C_p u_*^{-1}$) and categorized as: (1) pure wind sea ($C_p u_*^{-1} < 21$) or (2) swell/mixed sea ($C_p u_*^{-1} > 21$).

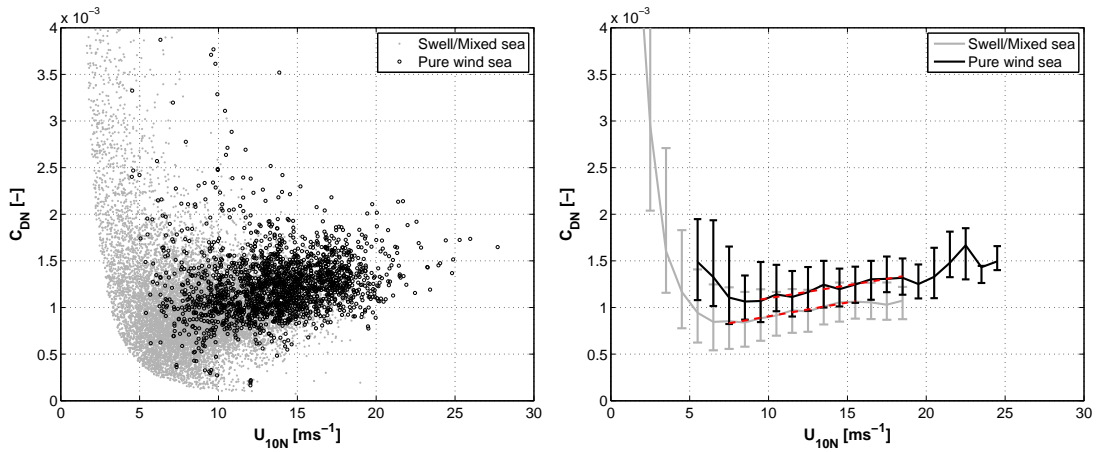


Figure 3.12: Drag coefficient versus wind speed, both at 10 m neutral. Pure wind sea data are distinguished from the swell and mixed sea cases using the criterion on wave age. Bin-median values with the error bar representing one standard deviation are shown on the left side of the panel.

A scatter plot based on 2 years' worth of 30 min averaged data is shown on the left side of the panel of Fig. 3.12, while on the right side of the panel of the same figure, the same data are shown but bin-median value averaged on 1 ms^{-1} bin width in order to investigate trends. The spread of the data is significantly higher for lower winds than in high winds. At low wind speeds ($U_{10N} <$

6 ms^{-1}), the neutral drag coefficient increases with decreasing wind speed and has a much higher value much than at higher wind speeds. A linear fit (dashed line on the right panel of Fig. 3.12) is considered to be the functional dependence of drag coefficient on neutral 10 m wind speed. When fitting data, wind speeds lower than 7 ms^{-1} were omitted due to the high spread of the data and therefore considered statistically unrepresentative. It is evident from Fig. 3.12 that the drag coefficient is significantly lower for mixed and swell sea compared to pure sea, in agreement with previous observations (e.g. Smith (1980); Donelan (1990); Drennan and Shay (2006)).

The linear relation between drag coefficient and neutral 10 m wind speed is expressed as:

$$C_{D10N} = A \cdot (U_{10N}) + B. \quad (3.19)$$

The coefficients A and B are reported in Table 3.2 separately for Swell/mixed sea and Pure sea.

Sea state	$A \cdot 10^{-3}$	$B \cdot 10^{-3}$
Pure	0.028	0.823
Swell/mixed	0.030	0.608

Table 3.2: Parameters describing functional dependence of drag coefficient on neutral 10 m wind speed based on wave age criteria.

In both cases, the coefficient C_{DN} increases with wind speed at almost the same rate (as seen from the A coefficients), with lower values for C_{DN} in swell/mixed seas (B coefficients).

Table 3.3 provides an overview of coefficients found for the linear relation for 'Young wind sea' from different data sets showing a wide range of values (see references for further information).

Experiment [Reference]	$A \cdot 10^{-3}$	$B \cdot 10^{-3}$
MARSEN Geernaert et al. (1987)	0.0847	0.577
HEXMAX Smith et al. (1992)	0.091	0.50
RASEX Vickers and Mahrt (1997)	0.067	0.75
SWADE Drennan et al. (1999)	0.070	0.6

Table 3.3: a and b coefficients found using different data sets in the literature as well as those found in this study.

As can be seen, in our case the dependence of sea state (young wind sea) is lower than the ones shown in Table 3.3.

3.5.2 Relationship between Roughness and Sea State

In Fig. 3.13, the functional dependence of dimensionless roughness $z_0\sigma^{-1}$ on inverse wave age $u_*C_p^{-1}$ under rough turbulent flow conditions ($R = u_*z_0\nu^{-1} > 2.3$) is investigated. Here, σ is related to significant wave height H_s as $\sigma = H_s/4$ and z_0 values were derived from measurements using Eq. 3.9. This approach for seeking a relational dependence on wave age is more adequate than using the Charnock parameter ($z_{Ch} = gz_0/u_*^2$) due to self-correlation problems (u_* is present in both parameters, z_{Ch} and wave age), as proposed by several authors (e.g. Donelan (1990); Drennan et al. (2003)).

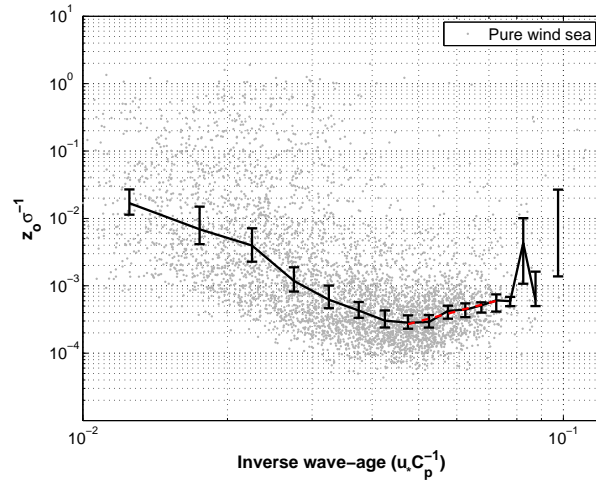


Figure 3.13: Dimensionless roughness versus inverse wave age for rough sea conditions ($R = u_*z_0\nu^{-1} > 2.3$). The solid black line represents bin-median values with one standard deviation error bar.

The scatter in the data is considerable and, as in the previous section, data have been bin-averaged in order to find the functional relationship between the two parameters.

Several authors (Drennan et al. (2003); Volkov (1970)) have already pointed out that, for smaller $u_*C_p^{-1}$ values, corresponding to fully developed conditions, the dimensionless roughness $z_0\sigma^{-1}$ decreases with inverse wave age (i.e. it increases with wave age), which is opposite to how it behaves at higher values (pure wind sea).

Here, the Volkov (1970) criterion of $u_*C_p^{-1} \geq 0.05$ which represents developing seas is used to find the dependence of dimensionless roughness ($z_0\sigma^{-1}$) on inverse wave age $u_*C_p^{-1}$ which is a power-law:

$$z_0\sigma^{-1} = a(u_*C_p^{-1})^b. \quad (3.20)$$

Coefficients a and b are given in Table 3.4 together with some experimental values given by other researchers.

Experiment [Reference]	a	b
HEXOS Donelan (1990)	1.84	2.53
FETCH Drennan et al. (2003)	13.4	3.4
FINO1 (This study)	0.084	1.88

Table 3.4: *Experimental Data.*

As can be seen, our values are not in close agreement with ones found by [Drennan et al. \(2003\)](#) ($z_0\sigma^{-1} = 13.4[u_*C_p^{-1}]^{3.4}$) which were derived from five deep water non-averaged data sets.

In addition, data cover a wide range of wave age (Fig. 3.14) with high variability in both friction velocity and wave phase speed, being a range similar to that used by [Drennan et al. \(2003\)](#), although covering higher wave phase speeds (up to 16 ms^{-1}). Therefore, the effect of spurious self-correlations in u_* are avoided ([Johnson et al. 2004](#); [Drennan et al. 2003](#); [Lange et al. 2004](#)). In other words, the wave age variation must be caused by the variation in C_p , not by the spreading in u_* .

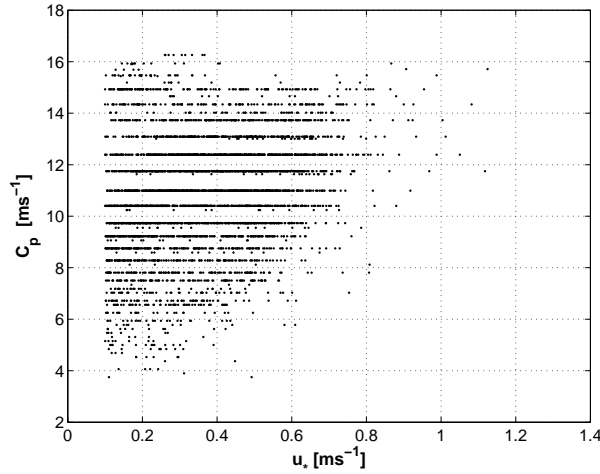


Figure 3.14: *Distribution of friction velocity u_* and peak phase speed C_p in rough sea conditions ($R = u_*z_0\nu^{-1} > 2.3$).*

3.6 Summary

The aim of this chapter was twofold: (1) to develop a database of reliable measurements to compare with the results of the LES simulations, (2) based on atmospheric data together with wave data, test under neutral conditions the dependence of wave age on surface stress.

First, data that have been corrected according to rigorous quality control and pre-processing procedures are presented through the chapter. Measurements from sonic anemometers were used as a primary source of data while cup anemometers, pressure and humidity are used when necessary (e.g. for corrections).

The eddy covariance method was used to derive the sensible heat fluxes and wind stress. The Obukhov length was then derived and the stability parameter (zL^{-1}) calculated. From the zL^{-1} values, it was found that at the FINO1 mast the boundary layer is often neutrally stratified (85% of time) with stable conditions for only 10% of the time ($zL^{-1} > 0.1$) and unstable stratification for 5% of the time ($zL^{-1} < 0.1$).

In addition, the Monin-Obukhov theory (MOST) was checked and was found to be in close agreement with the FINO1 data, although in the most stable situation there is a lot of scatter in the data. This may be related to the fact that in stable cases the measuring levels do not well represent surface conditions. Other sources could be attributable to sampling variability and large scale contributions.

In addition, wave data from a Wave-Rider Buoy located close to FINO1 mast were used to investigate the sea state dependence on the surface wind stress under neutral conditions and thus to gain a better description of the surface MABL. The so-called wave age parameter ($C_p u_*^{-1}$) was derived and used to classify the sea state, namely, pure wind-sea and swell. It has been shown that data present a general trend of increasing sea roughness with inverse wave age, in agreement with previous studies. However, from this investigation it became clear that the dependence of sea roughness with the sea state is less pronounced than the ones reported in the literature, which implies that the wave age affect in the drag coefficient is quite small. This can probably be explained by differences in data selection, mast location, data period as well as methods used to obtain the parameterization from data. It is worth mentioning that in this investigation the main difference to previous studies lies in the long period of data analysed. Future research must be considered to confirm this finding.

Due to the complexity of data processing, certain uncertainties remain, so this has to be taken into account in the values for derived quantities.

Chapter 4

Numerical Simulation.

Large Eddy Simulations of the Marine Boundary Layer: From Neutral to Stable Conditions

4.1 Introduction

In this Chapter, a numerical modelling approach, known as Large-Eddy Simulation (LES), is used for simulating the Marine Atmospheric Boundary Layer under neutral and stable conditions.

Idealized marine ABL simulations are performed over a flat and uniform surface where the Charnock equation is used on the bottom surface to characterize sea roughness. Initially, a neutral boundary layer is simulated, after which a progressive decreasing of heat flux at the surface (from -0.0 to -0.05 mKs^{-1}) is applied to stratify the layer. Mean and turbulent parameters as well as the impact of sub-grid scale (SGS) parameterization are analyzed depending on stability. In addition, sensitivity tests of the results on the grid resolution and domain size are performed. Finally, eddy structures are also presented through horizontal and vertical crosssections of the simulated flow. The simulation set-up is run several times, changing the geostrophic wind (8, 10, 12 and 14 ms^{-1}) in order to generate an LES database which will be compared to the FINO1 data in the next Chapter.

The analysis of these simulations is focussed on the lower spatial portion of the BL (i.e. first 300 m above surface) where wind turbines are placed. Throughout the Chapter, whenever possible, it is attempted to highlight the potential of PALM modelling in addressing important wind energy related issues.

The present Chapter is organized as follows. The LES code (PALM) used in this study is described with a brief review of the theoretical basis in Section 4.2. In Section 4.3, the minimum resolution required for modelling atmospheric conditions with a focus on wind energy is investigated. The model set-up strategy and simulation details are given in Section 4.4. Simulation results in neutral and stable regimes are discussed in Section 4.5 along with a sensitivity analysis on resolution and domain size. In Section 4.6, eddy structures are presented. Finally, a summary is presented in Section 4.7.

4.2 Large Eddy simulation: PALM code

This Section gives a general description of the **PARallel Large-Eddy Simulation Model (PALM)** in its dry BL mode as used in this study.

So far, PALM has been applied successfully to the investigation of turbulent flows in homogeneously (Schröter et al. 2001) and heterogeneously heated convective Boundary Layers (Raasch and Harbusch 2001; Letzel and Raasch 2003; Weinbrecht et al. 2004; Steinfeld et al. 2008) as well as in weakly Stable Boundary Layers (Beare et al. 2006; Steinfeld et al. 2007) and Neutral Boundary Layers (Letzel et al. 2006).

For additional details and features of the LES code, please refer to (Raasch and Schröter 2001) and to the on-line PALM documentation¹.

4.2.1 Governing Equations of Fluid Motion

The dynamics of the atmosphere are governed by partial differential equations, describing the conservation laws for momentum (Navier-Stokes equations, henceforth NSE), mass of dry air, internal energy (potential temperature) and other scalars. In Cartesian coordinates (x, y, z) , the NSE and the equation for conservation of mass and heat in the Earth's rotating frame of reference can be written as:

- Conservation of Momentum (Newton's Second Law):

$$\frac{\partial u_i}{\partial t} + u_k \frac{\partial u_i}{\partial x_k} = -\epsilon_{ijk} f_j u_k - \frac{1}{\rho} \frac{\partial p}{\partial x_i} - g \delta_{i3} + \nu_m \left\{ \frac{\partial^2 u_i}{\partial x_k^2} + \frac{1}{3} \frac{\partial}{\partial x_i} \left(\frac{\partial u_k}{\partial x_k} \right) \right\}, \quad (4.1)$$

- Conservation of Mass (Continuity Equation):

$$\frac{\partial \rho}{\partial t} = -\frac{\partial \rho u_k}{\partial x_k}, \quad (4.2)$$

- Conservation of Heat (First Law of Thermodynamics):

$$\frac{\partial \theta}{\partial t} + u_k \frac{\partial \theta}{\partial x_k} = \nu_h \frac{\partial^2 \theta}{\partial x_k^2}. \quad (4.3)$$

¹http://www.muk.uni-hannover.de/raasch/PALM_group/PALM_group.html.

The Equation of State (Ideal Gas Law) with specific gas constant for dry air R_L and temperature T completes the system of equations:

$$p = \rho R_L T \quad (4.4)$$

The velocity field is $u_i = (u, v, w)$, t is the time, ρ is air density, p is air pressure, $f_i = (0; 2\Omega \cos\phi; 2\Omega \sin\phi)$ is the Coriolis parameter with Ω the angular velocity of the Earth ($\Omega = \frac{2\pi \text{radians}}{24\text{h}} = 7.27 \times 10^{-5} \text{ s}^{-1}$) and ϕ the latitude, g is the gravitational acceleration, δ_{ij} is the Kronecker delta ($\delta_{ij} = 1$ for $i = j$, 0 otherwise), ϵ_{ijk} is the alternating unit tensor, $\nu_m = \frac{\mu}{\rho}$ and ν_h are the molecular viscosities (or diffusion coefficients) for momentum and temperature respectively. In an analogous way to Eq. 4.3, conservation laws can be derived for passive scalars, omitted here for the sake of brevity.

Potential temperature is defined as:

$$\theta = T \left(\frac{p_0}{p} \right)^{\frac{R}{c_p}} \quad (4.5)$$

where T and p are the current absolute temperature and pressure of air, p_0 is the standard pressure, usually taken as 1000 hPa , R is the gas constant of dry air and c_p is the specific heat capacity at a constant pressure.

The NSE describe all flow structures at all times and length scales. The largest structures are on the turbulent flow scale with the geometry of the problem incorporated e.g. the boundary layer height ($\sim 10^3 \text{ m}$), while the smallest scale is the size of the dissipative eddies ($\sim 10^{-3} \text{ m}$) (Stull 1998).

In total, a system of seven equations with seven variables have to be solved. Due to the nonlinear terms in Eqs. 4.1 and 4.3, no general analytic solution of the system exists for high Reynolds number as is the case for atmospheric flows. Therefore, the system has to be solved numerically.

In the upper equation and further in this Chapter, wherever the same index appears twice in a term, a summation over the index range is implied following the Einstein summation convention.

4.2.2 Filter Operation

In the LES, all the field variables $\psi(x_i, t)$ are decomposed into resolved and unresolved (sub-grid, SGS) parts. This is done by low pass filtering the governing equations (Eqs. 4.1-4.3) with a filtering function which removes all the finer fluctuations.

Instead of applying an explicit filter as described, however, the PALM model uses a finite-volume discretization of the flow equations on a numerical mesh (grid-volume averaging) as an implicit filter tied to the numerical resolution. In this way, turbulent scales smaller than the numerical mesh spacing are unresolved, whereas, the larger scales are resolved and associate the computed velocity field with a filtered velocity:

$$\bar{\psi}(x, y, z, t) = \frac{1}{\Delta x \Delta y \Delta z} \int_{x_1 - \frac{\Delta x}{2}}^{x_1 + \frac{\Delta x}{2}} \int_{y_1 - \frac{\Delta y}{2}}^{y_1 + \frac{\Delta y}{2}} \int_{z_1 - \frac{\Delta z}{2}}^{z_1 + \frac{\Delta z}{2}} \psi(x', y', z', t) dx' dy' dz'. \quad (4.6)$$

Based on the so-called Reynold's decomposition ([Reynolds 1895](#)), the difference between the filtered values $\bar{\psi}$ and the unfiltered values ψ is called the fine structure, small scale portion or SGS portion ψ' :

$$\psi = \bar{\psi} + \psi' \iff \psi - \bar{\psi} = \psi' \quad (4.7)$$

The application of the Reynold's decomposition requires some averaging rules for the turbulent value ψ' , which are termed Reynold's postulates:

- $\overline{\psi'} = 0$
- $\overline{\psi\phi} = \bar{\psi}\bar{\phi} + \overline{\psi'\phi'}$
- $\overline{\overline{\psi}\phi} = \overline{\psi\phi}$
- $\overline{a\psi} = a\bar{\psi}$
- $\overline{\psi + \phi} = \bar{\psi} + \bar{\phi}$

with ϕ being a second atmospheric variable while a is a constant.

In PALM, (4.6)–(4.7) translate as follows: $\bar{\psi}(x_i, t)$ represents the mean value of an atmospheric variable averaged over the grid volume at time t and $\overline{\psi'}(x_i, t)$ is the sub-grid scale (SGS) or local fluctuation at time t that is not resolved by the model and has to be parametrized.

4.2.3 Filtered Governing Equations

Applying the grid-volume averaged operator (Eq. 4.6) to the governing equation (Eqs. 4.1– 4.3) of the flow, yields the resulting governing equations of PALM. The filtered, non-hydrostatic ($\bar{w} = 0$), Boussinesq-approximated² Navier-Stokes equations (conservation of momentum) imply incompressibility through the continuity equation (conservation of mass) and the 1st law of thermodynamics (conservation of energy):

$$\frac{\partial \bar{u}_i}{\partial t} = -\frac{\partial}{\partial x_k} (\bar{u}_k \bar{u}_i) - \frac{1}{\rho_0} \frac{\partial \bar{p}^*}{\partial x_i} - (\epsilon_{ijk} f_j \bar{u}_k - \epsilon_{ij3} f_3 u_{gk}) + g \frac{\bar{\theta}^*}{\theta_0} \delta_{i3} - \frac{\partial}{\partial x_k} (\overline{u'_k u'_i}), \quad (4.8)$$

$$\frac{\partial \bar{u}_k}{\partial x_k} = 0, \quad (4.9)$$

$$\frac{\partial \bar{\theta}}{\partial t} = -\frac{\partial}{\partial x_k} (\bar{u}_k \bar{\theta}) - \frac{\partial}{\partial x_k} (\overline{u'_k \theta'}). \quad (4.10)$$

where the variables have the same meaning as before but, now, \bar{u}_i is the filtered velocity, $\bar{\theta}^*$ is the filtered potential temperature, \bar{p}^* is the filtered modified pressure and u_g is the geostrophic wind defined by $\rho_0^{-1} \partial_{x_i} p_0 = \epsilon_{ij3} f_3 u_{gk}$. Viscous dissipation and molecular diffusion have been neglected due to the high Reynolds number of the ABL.

The above equations govern the evolution of the large, energy-carrying, scales of motion where the instantaneous small-scale contributions are removed by the filter, but their effects on the large-scale motions remain in the unclosed residual terms ($\tau_{ki} = \overline{u'_k u'_i} = \overline{u_k u_i} - \bar{u}_k \bar{u}_i$ called Reynold stresses (per unit density) and $\overline{u'_k \theta'} = \overline{u_k \theta} - \bar{u}_k \bar{\theta}$ called Reynold fluxes), representing the influence of subgrid scales on the resolved scales. These additional residual terms must be modelled (parametrized) in order to close the system of equations. This parameterization must be such as to simulate the transfer (or removal) of the variance cascade from resolvable small scales of motion to unresolvable subgrid scale (Deardorff 1973).

Derivatives are approximated by finite differences ($\partial x_i \approx \Delta x_i, \partial t \approx \Delta t$). The model variables are staggered using an Arakawa C-grid (Arakawa and Lamb 1977). Vertical grid spacing can be stretched. Advection of momentum is formulated using a second-order scheme that conserves the integral of linear and quadratic quantities up to very small errors (Piacsek and Williams 1970). Non-divergent flow is assured by solving a Poisson equation for the so-called pressure perturbation using Fast Fourier Transforms (Uhlenbrock 2001).

²This approximation neglects density fluctuations but not the buoyancy (gravitational) term. This is because the acceleration of gravity is relatively large in comparison with other accelerations in the equation.

This system of differential equations is advanced in time using an explicit multistage PALM's default third-order Runge-Kutta scheme (Butcher 2003). By default, the time step is computed based on the following criteria,

$$\Delta t = 0.9 \cdot \min(\Delta t_{CFL}, \Delta t_{diff}) \quad (4.11)$$

where Δt_{CFL} (Courant-Friedrich-Levy-number) refers to the *advection criteria* and Δt_{diff} refers to the *diffusion criteria*.

In case of a non-zero geostrophic wind the coordinate system can be moved along with the mean wind in order to maximize the time step (Galilei-Transformation). PALM uses a constant density $\rho_0 \equiv 1 \text{ kgm}^{-3}$.

4.2.4 Subgrid-Scale Modelling

4.2.4.1 Turbulence Closure: TKE-based (Eddy-Viscosity) Model

The transition from Eqs. (4.1)–(4.3) to Eqs. (4.8)–(4.10) leads to a system of differential equations with more unknown parameters than equations. The second-order moments (covariances), $\overline{u'_k u'_i}$ and $\overline{u'_k \theta'}$ in the Boussinesq equations in Eq. 4.8 and Eq. 4.10 contain unknown subgrid-scale fluctuations (unresolved scales) and need to be parametrized (using an SGS model) in terms of the resolved-scale quantities to close the equations,

$$\overline{u'_k u'_i} = -K_m \left(\frac{\partial \bar{u}_i}{\partial x_k} + \frac{\partial \bar{u}_k}{\partial x_i} \right) - \frac{2}{3} \bar{e} \delta_{ij}, \quad (4.12)$$

$$\overline{u'_k \theta'} = -K_h \left(\frac{\partial \bar{\theta}}{\partial x_k} \right), \quad (4.13)$$

The turbulent diffusion coefficients for momentum and heat, K_m and K_h , are parametrized by the subgrid-scale turbulent kinetic energy (SGS-TKE), $\bar{e} = \frac{1}{2} \overline{u_i'^2}$, according to:

$$K_m = C_m l \sqrt{\bar{e}}, \quad (4.14)$$

$$K_h = \left(1 + \frac{2l}{\Delta}\right) K_m, \quad (4.15)$$

where $C_m = 0.1$ is the so-called Smagorinsky coefficient (which determines the magnitude of the mean rate of SGS dissipation of kinetic energy), $\Delta = \sqrt[3]{\Delta x \cdot \Delta y \cdot \Delta z}$ is a characteristic grid length and l is the mixing length (or SGS length scale) defined as:

$$l = \begin{cases} \min \left(\Delta, 0.7z(k=1), 0.76 \left(\frac{\sqrt{\bar{e}}}{N} \right) \right) & \text{stable stratification,} \\ \min \left(\Delta, 0.7z(k=1) \right) & \text{otherwise.} \end{cases} \quad (4.16)$$

$z(k=1)$ is the normal distance to the nearest bottom surface. The last expression for stable stratification was suggested by Deardorff (1980), where N is the local Brunt-Väisälä frequency defined by $N^2 = \frac{g}{\theta_0} \frac{\partial \bar{\theta}}{\partial z}$, where $\frac{g}{\theta_0}$ is the buoyancy coefficient.

The last remaining unknown is the SGS-TKE \bar{e} itself which requires an additional prognostic equation with further parametrization,

$$\frac{\partial \bar{e}}{\partial t} = \underbrace{-\frac{\partial}{\partial x_j} (\bar{u}_j \bar{e})}_A - \underbrace{\tau_{ij} \frac{\partial \bar{u}_i}{\partial x_j}}_S + \underbrace{\left(\frac{g}{\theta_0} \right) \overline{u'_3 \theta'}}_B - \underbrace{\frac{\partial (\overline{u'_j e})}{\partial x_j}}_{T_r} - \underbrace{\frac{1}{\rho_0} \frac{\partial (\overline{u'_j p'})}{\partial x_j}}_{P_r} - \epsilon \quad (4.17)$$

Eq. 4.17 governs the nature of production and destruction in the boundary layer in which the following terms appear from left to right: local TKE storage or tendency, TKE advection (A), shear (S), buoyancy production or consumption (B), turbulent TKE transport (T_r), pressure correlation term (P_r) and energy dissipation (ϵ). The mechanical or shear production terms (S) are usually, but not always, a source of turbulence energy. The buoyancy term (B) can either add to turbulence due to buoyant motions during free convection, or it can consume turbulence energy by converting it into potential energy in statically stable environments. The advection term (A) moves turbulence by the mean wind, while the turbulent transport term (T_r) moves TKE by action of turbulent gust. The pressure correlation term (P_r) is poorly understood and difficult to measure, but is not necessarily small. The molecular dissipation term (ϵ) is always a loss term and is the rate at which turbulent kinetic energy is converted into inertial energy (i.e. heat) by working against viscous stress.

Turbulence forms in response to flow instabilities and works in such a way as to reduce the instability via mixing of air. Because of molecular dissipation, TKE is not a conserved quantity.

The last two terms in Eq. 4.17 are unknowns and therefore they must be parametrized. According to Kolmogorov's theory, the SGS-TKE dissipation rate (i.e. the decay of turbulent eddies into heat) is defined as:

$$\epsilon = \left(0.19 + 0.74 \frac{l}{\Delta} \right) \cdot \frac{\bar{e}^{\frac{3}{2}}}{l} \quad (4.18)$$

and for turbulence energy and pressure fluctuations as:

$$\overline{u'_k \left(e + \frac{p'}{\rho_o} \right)} = -2K_m \frac{\partial \bar{e}}{\partial x_j} \quad (4.19)$$

4.2.5 Boundary Conditions

The **surface boundary conditions** require calculation of the instantaneous (filtered) local surface shear stress and surface heat flux at each surface grid point. This is accomplished through the application of Monin-Obukhov similarity theory (Monin and Obukhov 1959) between the surface and the local (filtered) velocity and potential temperature fields, which provides wall functions which account for the surface roughness length z_0 and stratification effects important in atmospheric flows.

The surface shear stress related to the friction velocity according to $u_* = (|\tau_{ij}/\bar{\rho}|)^{\frac{1}{2}}$ is computed from the mean resolved horizontal velocity at the first vertical model level (i.e. at a height of $z = z(k=1) = \Delta_z/2$) as follows:

$$u_* = \begin{cases} \frac{\kappa |\overline{v}(z)|}{\ln\left(\frac{z}{z_0}\right) + 5Rif\left(\frac{z-z_0}{z}\right)} & \text{for } Rif \geq 0, \\ \frac{\kappa |\overline{v}(z)|}{\ln\left(\frac{z}{z_0}\right) - \ln\left(\frac{(1+A)^2(1+A^2)}{(1+B)^2(1+B^2)}\right) + 2(\arctan(A) - \arctan(B))} & \text{otherwise} \end{cases} \quad (4.20)$$

where $\kappa = 0.4$ is the von Kàrman constant, z_0 is the roughness length, $A = (1 - 16Rif)^{\frac{1}{4}}$ and $B = (1 - 16Rif\frac{z_0}{z})^{\frac{1}{4}}$ and Rif is the Richardson flux number defined as:

$$Rif = \frac{z}{L} = -\frac{\overline{\kappa g w' \theta'_0}}{\bar{\theta}_0 u_*^3} z. \quad (4.21)$$

which accounts for the surface-layer stability correction. In a similar manner, the surface heat flux $\overline{w' \theta'_0} = -u_* \theta_*$ is computed from the instantaneous (filtered) local potential temperature at $z = \Delta_z/2$ through:

$$\theta_* = \begin{cases} \frac{\kappa(\bar{\theta}(z) - \bar{\theta}(z_0))}{\ln\left(\frac{z}{z_0}\right) + 5Rif\left(\frac{z-z_0}{z}\right)} & \text{for } Rif \geq 0, \\ \frac{\kappa(\bar{\theta}(z) - \bar{\theta}(z_0))}{\ln\left(\frac{z}{z_0} + 2\ln\left(\frac{1+A}{1+B}\right)\right)} & \text{otherwise} \end{cases} \quad (4.22)$$

with $A = (1 - 16Rif)^{\frac{1}{2}}$ and $B = \left(1 - 16Rif\frac{z_0}{z}\right)^{\frac{1}{2}}$, where $\bar{\theta}(z_0)$ and θ_* denote the surface potential temperature and characteristic temperature at the first model level, respectively.

A damping layer is implemented at the **upper boundary** of the model domain to avoid the development of gravity waves and their reflection from the top of the model. Lateral boundary conditions are cyclic, i.e periodic in both horizontal directions.

4.3 Setting of Simulation Resolution: Minimum Time-step

The main interest in setting the time-step or grid-resolution in an LES model is to make sure that all relevant turbulent information in the application of interest (wind energy, in our case) is sampled/solved in sufficient detail. So far, the dynamic response of the wind turbine system on turbulent elements (eddies) is still under continuous investigations and there is not a clear and consistent answer to this matter. Aerodynamic loads on the wind turbine could give a preliminary insight into the minimum sampled step or grid resolution required and thus optimize the computational cost.

4.3.1 Offshore wind turbine

As an example of an offshore wind turbine, the Multibrud M5000 turbine is considered in this study with technical data summarized in Table 4.1.

Rated power	5 MW
Number of blades	3
Rotor Orientation	Upwind
Rotor Diameter	116 m
Hub Height	90 m
Cut-In, Rated, and Cut-Out Wind Speed	4 ms ⁻¹ , 12 ms ⁻¹ , 25 ms ⁻¹
Design Tip Speed ratio	8
Maximum Blade Speed	90 ms ⁻¹

Table 4.1: Technical data for Multibrud M5000. Source: <http://www.multibrud.de/>.

As given in Table 4.1, the turbine has a rotor diameter of 116 m with a rated power of 5 MW produced at a rated wind speed of 12 ms⁻¹. Rotor speed increases up to the wind speed needed to maximize energy capture, and it remains constant at higher wind speed, with increased blade pitch into the wind to hold the mean power close to the rated power. Hub height is 90 m.

4.3.2 Wind Turbine Operating in Turbulent Flow

When a wind turbine is in operation, its rotor rotates through a three-dimensional turbulence wind field which varies in space, time and direction. A momentary representation of such a wind field is shown in Fig. 4.1.

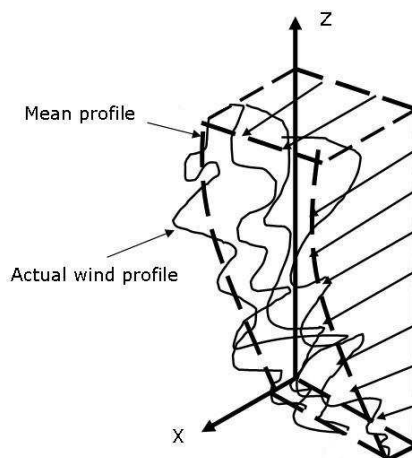


Figure 4.1: Actual wind speed profile.

From Fig. 4.1, it is clearly seen that the mean wind speed increases with height due to **wind shear**. Furthermore, the actual wind speed at any location varies in time and direction around its mean value due to the effect of **turbulence**.

When a rotating blade passes through an eddy, it experiences a short period of higher and lower wind speed as well as different wind angles since the wind over the whole rotor swept area is not constant. Because the size of the eddy is such that a blade will pass through the eddy several times, the turbine structure will experience a load peak at the **rotation frequency of the rotor**, called 1P. This eddy slicing will create not only a load peak at the frequency of 1P but also at the frequency of all the blades passing through it: $N_b P = 3P$ for a three-bladed turbine. To avoid resonance, the rotor structure should be designed such that its first natural frequency does not coincide with either 1P or 3P excitation (van der Tempel 2006).

To take this effect into account within the turbulence spectrum, the stationary turbulence spectrum can be transformed into a rotational spectrum (Fig. 4.2).

The corresponding 1P rotational frequency is giving by:

$$f_{1P} = \frac{\lambda U_o}{\pi D_{rotor}} \quad (4.23)$$

where Ω is the rotor angular velocity, U_o is the undisturbed wind velocity, D_{rotor} is the rotor diameter and λ is the tip speed ratio (ratio between the speed of the blade tip and the wind speed), which is given by:

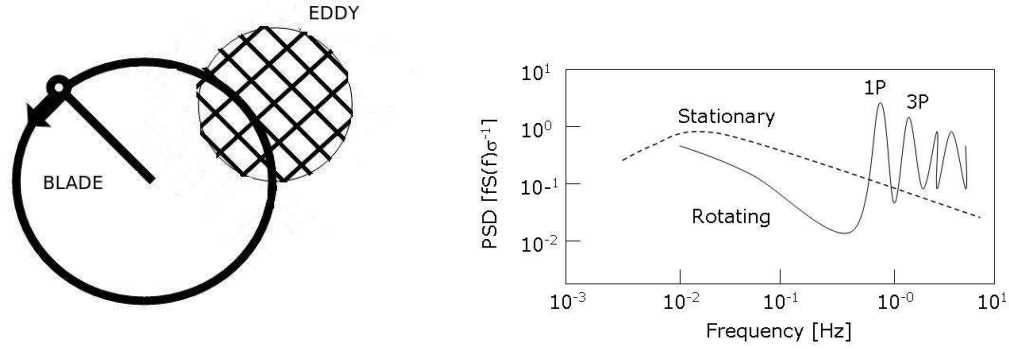


Figure 4.2: Blade passing through a turbulent eddy (left-side panel). Stationary and rotationally sampled turbulence spectrum (right-side panel).

$$\lambda = \frac{U_{tip}}{U_o} = \frac{\Omega R}{U_o} = \frac{f_{1P}\pi D_{rotor}}{U_o} \quad (4.24)$$

with U_{tip} the velocity which takes the rotor to make one full revolution.

This means that for a fixed (optimal) tip speed ratio, the rotational frequency will decrease when the diameter increases. The results of Eq. 4.23 for a rated wind speed of $U_{rated} = 12 \text{ ms}^{-1}$ (the wind speed at which the generator reaches maximum power), $\lambda = 8$ and rotor diameters of 116 m are given in Table 4.2. Another important frequency to take into account is the **root flatwise bending moment** which has a load peak at a frequency of about 1 Hz for the offshore wind turbine considered in this study. A summary of the frequencies of interest over the rotor plane is given in Table 4.2.

ID	f_{max} [Hz]
1P, rotational frequency	0.26
3P, rotational frequency	0.79
root flatwise bending moment frequency	1.0

Table 4.2: Frequencies of interest over rotor plane.

Therefore, 1 Hz is the highest required solving frequency ($f_{Nyquist}$), being the corresponding time step in the time domain:

$$\Delta f = 1/(2f_{Nyquist}) = 0.5 \text{ sec}. \quad (4.25)$$

Thus, it is considered that to assure that the simulated wind flows include frequency contributions of the same order of magnitude that are important for WT dynamics, simulations with a time of at least 0.5 sec time resolution are needed.

In order to get an idea about the minimum spatial resolution, it is assumed the blade thickness (5 m) of the wind turbine rotor is the limit. For modern multi-MW wind turbines with blade lengths of about 60 m, this means about 5 m as the minimum resolution. This gives us a value for the inflow conditions on the blade element, and therefore the connected aerodynamic forces. It is not necessary in this study (and computationally almost impossible for a domain size of several km's) to simulate the flow around the blade element surface. It is also beyond the aim of this work to study special flow effects, e.g. the vortex generation at the blade tip.

4.4 Model Set-up Strategy

A series of LES simulations for neutral (NBL) and stable (SBL) marine atmospheric boundary layers with increasing stability were performed using the PALM code. The set up methodology followed in this study was similar to the one used in [Jiménez and Cuxart \(2005\)](#).

Each simulation is run for 123,200 sec time period (~ 32.2 hours), with a neutrally stratified boundary layer developed during the first 80,000 sec and a potential temperature assumed constant over the entire domain (settled at $\theta_0 = 290.5$ K, based on the mean value determined from the FINO1 data) and zero surface heat flux. Afterwards, during the next 43,200 sec of the run, the surface heat flux is progressively reduced from 0 to -0.05 mKs^{-1} to generate a stable ABL with different grades of stratification. The surface cooling procedure is applied as follows: after every two hours of simulation time (considered long enough to guarantee quasi-steady conditions³) the surface heat flux is changed to the next value, such that all values of $\overline{w'\theta'}_s = -0.005, -0.01, -0.02, -0.03, -0.04$ and -0.05 mKs^{-1} are applied each two hours during a period of 12 hours. This forcing method for developing the SBL has been used previously by several authors (e.g. [Saiki et al. \(2000\)](#); [Ding et al. \(2001\)](#); [Jiménez and Cuxart \(2005\)](#)).

Cyclic or periodic boundary conditions are applied in both horizontal directions. The Coriolis parameter is set to $f_c = 1.181 \cdot 10^{-4} \text{ s}^{-1}$, corresponding to a latitude of about 54° N (where the FINO1 platform is located). The bottom-surface is uniform and flat and, in order to take into account the roughness over the sea (z_0), the Charnock equation ([Charnock 1955](#)) is used⁴ where z_0 is computed at each time step.

The grid spacing (see Table 4.3) is isotropic along all directions except vertical, where in order to limit the number of grid points a stretching factor (8%) is applied above 600 m up to the top of the model where the maximum resolution allowed is 10m. This saves computational time. The last hour of each section is used to compute the statistics for analysis.

For all simulations performed, the LES model is initialized by prescribing an initial temperature profile, geostrophic wind speed in the barotropic environment (u_g (in the East-West direction) and $v_g = 0$), surface roughness length z_0 , and Coriolis parameter (f_c). Based on these parameters a

³In the stable regime, it must be referred to as a quasi-equilibrium since the PBL will keep evolving with time as a result of surface forcing.

⁴This parameterization assumes that the roughness length z_0 depends on surface stress (u_*) and gravity ($z_0 = (z_{Ch}/g)u_*^2$ with $z_{Ch} = 0.0185$).

one-dimensional (1D) equilibrium solution for the wind profile under quasi-steady conditions is calculated. With this 1D solution, the whole 3D-model domain is then initialized assuming a horizontally homogeneous state. In addition, random perturbations are applied to trigger turbulence.

For different simulation runs, different combinations of grid size, domain size and geostrophic winds (u_g) are given in Table 4.3. Here L_x , L_y , L_z are the widths of the computational domain, N_x , N_y , N_z are the number of grid points and Δ_x , Δ_y , Δ_z define the grid size in the x-, y- and z-directions, respectively.

ID	(u_g, v_g)	$L_x \times L_y \times L_z [m^3]$	$N_x \times N_y \times N_z^5$	$\Delta_x \times \Delta_y \times \Delta_z [m^3]$
NS1	(8, 0)	$2560 \times 1280 \times 1371$	$512 \times 256 \times 152$	$5 \times 5 \times 5$
NS2	(10, 0)	$2560 \times 1280 \times 1371$	$512 \times 256 \times 152$	$5 \times 5 \times 5$
NS3	(12, 0)	$2560 \times 1280 \times 1371$	$512 \times 256 \times 152$	$5 \times 5 \times 5$
NS4	(14, 0)	$2560 \times 1280 \times 1371$	$512 \times 256 \times 152$	$5 \times 5 \times 5$
NS5	(10, 0)	$1280 \times 640 \times 1388$	$640 \times 320 \times 390$	$2 \times 2 \times 2$
N6	(10, 0)	$1280 \times 640 \times 1375$	$128 \times 64 \times 87$	$10 \times 10 \times 10$
N7	(10, 0)	$2560 \times 1280 \times 1375$	$256 \times 128 \times 87$	$10 \times 10 \times 10$
N8	(10, 0)	$5120 \times 2560 \times 1375$	$512 \times 256 \times 87$	$10 \times 10 \times 10$

Table 4.3: Summary of the LES simulations. The runs prefixed with NS refer to a neutral and stable regime and the runs prefixed with N refer to a neutral regime only. Note that Δ_z is constant below 600m.

This configuration set-up is motivated by the following reasons:

- Runs with several levels of geostrophic wind allow us to generate an LES database which will be used for comparison with observational data (see next chapter). At the same time, temporal surface forcing provides a range of different ABL regimes (from neutral to different grades of stable stratification) and the evolution can be investigated in order to get a better understanding of turbulence in both regimes (runs NS1 to NS4).
- A coarse grid resolution enables us to identify the strengths and/or weaknesses of the SGS model by performing a sensitivity analysis (Basu and Porté-Agel 2006) (runs NS2, NS5 and N7).
- Different domain sizes are used to carry out a sensitivity test and thus evaluate their effect on the simulation results (runs N6 to N8).
- Forcing parameters are intended to represent a MABL.

It is worth mentioning that over the sea, a stable BL can form by advection of warmer air over cooler water with an associated overlaying stable internal BL. For all simulations in this work, the initial

potential temperature profile was formulated with a neutral stratified layer up to the upper part of the domain. Nevertheless, a simulation with a finite stratification aloft was performed (not shown) and no differences below 300 m were found in the turbulence statistics.

We have to keep in mind that the size of such a simulation is inevitably large and therefore computationally very expensive for practical engineering calculations. Moreover, as the wind speed increases, the computational effort increases because of the small time step (limited by the numerical stability criterion). The simulation set-up was selected as a compromise between a model resolution as high as possible and the available computational resources.

All simulations were performed on an SGI Altrix ICE 8200 Plus machine of the 'Norddeutscher Verbund für Hoch- und Höchst-leistungsrechnen' (HLRN) in Hannover/Berlin, Germany. A simulation took on average 24 hours CPU time for the runs prefixed with 'NS' (see Table 4.3) using 512 processors (Intel Xeon Harpertown).

4.4.1 Theoretical maximum surface heat flux

Following [Saiki et al. \(2000\)](#) and [Jiménez and Cuxart \(2005\)](#), the maximum heat flux that can be supported in the SBL is checked by using the theoretical expression derived by [Derbyshire \(1990\)](#):

$$(\overline{w\theta_s})_{max} = \frac{\theta_0 R_{fc}}{g\sqrt{3}} u_g^2 |f_c|, \quad (4.26)$$

where R_{fc} is the critical flux Richardson number, f_c is the Coriolis parameter, g is the gravitational acceleration and θ_0 is the reference value for the temperature. $|\cdot|$ denotes the absolute value.

$u_g [m s^{-1}]$	$R_{fc} = 0.2$	$R_{fc} = 0.25$	$R_{fc} = 0.3$
8	-0.025	-0.032	-0.038
10	-0.040	-0.050	-0.061
12	-0.058	-0.072	-0.087
14	-0.079	-0.098	-0.119

Table 4.4: Maximum surface heat fluxes [$mK s^{-1}$] derived from Derbyshire's formula for each u_g and different values of R_{fc}

Table 4.4 shows the maximum possible values of the surface heat flux according to Eq. 4.26 for each prescribed geostrophic wind, while varying the value of R_{fc} . As was pointed out in [Jiménez and Cuxart \(2005\)](#), this formula must be treated with caution, since it is based on the following hypothesis over land: (i) quasi-steady state, (ii) SBL considered as closed system, (iii) inertial equilibrium and

(iv) constant R_{fc} with height inside the stable BL. It can be seen that the values of $\overline{w\theta}_s$ are quite sensible with the value chosen for R_{fc} . A value of $R_{fc} = 0.25$ is commonly used to determine the maximum value allowed although, to have a safe margin on the highest value allowed, $R_{fc} = 0.2$ was used here due to the uncertainties in this formulation. Therefore, for geostrophic winds of $u_g = 12 \text{ ms}^{-1}$ and $u_g = 14 \text{ ms}^{-1}$, the maximum lies above the highest surface heat flux ($(\overline{w\theta}_s)_{max} = -0.05$) applied in the current simulations. Instead, for simulations with $u_g = 8 \text{ ms}^{-1}$ and $u_g = 10 \text{ ms}^{-1}$, a $\overline{w\theta}_s$ prescribed as $\overline{w\theta}_s = -0.02$ and $\overline{w\theta}_s = -0.04$ are allowed, respectively.

These results are consistent with simulations which are associated with drastic changes in surface temperature (runaway cooling), as shown in Fig. 4.3 (left-side panel). Results of the study from (Jiménez and Cuxart 2005) are also shown (Fig. 4.3 (right-side panel)), presenting a similar behaviour. However, simulations in this study present higher cooling at the surface. As the cooling that is applied increases (increasing negative surface heat flux) the surface temperature decreases.

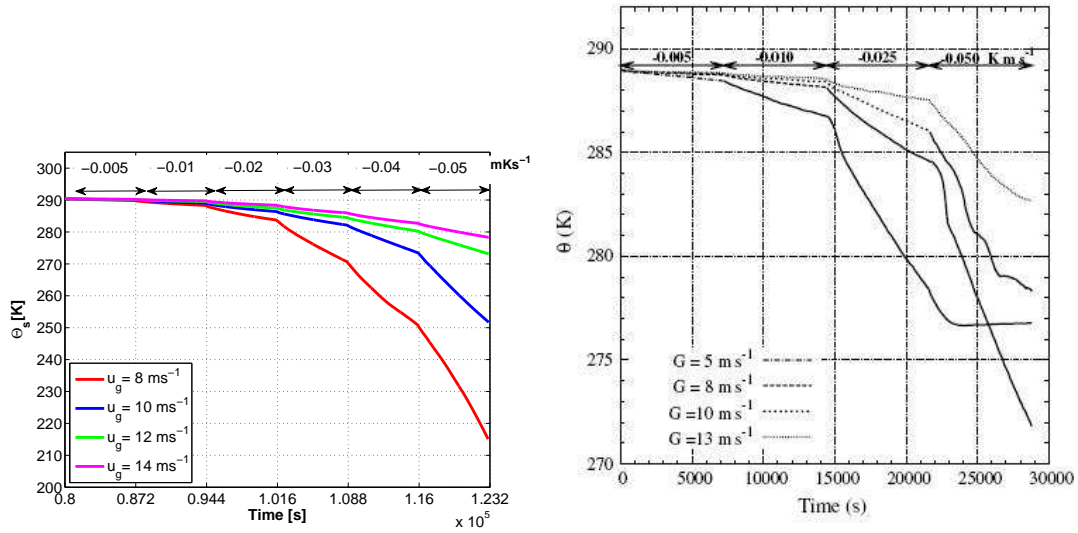


Figure 4.3: Temporal evolution of the surface potential temperature for each geostrophic wind from the present study (left) and from Jiménez and Cuxart (2005) study.

4.5 Results and Discussions

In the present section, the results from PALM used in an idealized setting to simulate offshore atmospheric conditions are reported. Results are focussed on the lower vertical part of the boundary layer (first 300 m above the surface), where the wind turbines are placed. Note that simulations of runaway cooling are also considered.

4.5.1 Bulk Parameters

The Tables in sections 4.5 to 4.8 provide a summary of the resulting bulk parameters typically examined in BL studies and computed during the last hour of each section as the heat fluxes decrease and for all geostrophic winds simulated. Parameters included in this summary are: turbulent BL height (δ), stability parameter (zL^{-1}), friction velocity (u_*), averaged time step (dt) and strength of surface cooling⁶ ($\overline{\Delta\theta_s}$). This summary allows us to investigate the sensitivity of the model to geostrophic wind and range of stability regime for both stratifications.

The turbulent boundary layer height (δ) is computed as $(1/0.95)$ times the height at which the horizontal shear stress has dropped to 5% of its surface value (Kosović and Curry 2000; Saiki et al. 2000; Beare and Macvean 2004; Basu and Porté-Agel 2006). It can be seen that, as stability increases, the turbulent BL height decreases for a fixed geostrophic wind. For a fixed surface heat flux, the height is reduced as the geostrophic wind decreases due to the decrease of shear. For the higher stability cases, values of δ are smaller than 148 m which implies that the rotor blades of the WT could experience very different inflow conditions (e.g. turbulent and non-turbulent periods).

To assess the strength of the stability, the ratio (zL^{-1}) is used where L is the Obukhov length (typical length of the eddies in SBL) defined as:

$$L = -\frac{u_*^3 \theta_0}{kgw\theta}, \quad (4.27)$$

It is common to use $z = 10$ m as a reference height. Here, due to vertical discretization, the values of L at 7.5 m and 12.5 m are computed and averaged to get a value at 10 m.

⁶This is defined as the difference between the residual layer air, $\overline{\theta_0}$, and the near-surface air, $\overline{\theta_s}$, and accounts for the amount of cooling that has occurred since SBL formation for each section.

The following stability classification ([Mahrt 1998](#)) is considered here:

- $0.0 < zL^{-1} < 0.06$: weakly stable regime,
- $0.06 < zL^{-1} < 1$: moderately stable regime,
- $zL^{-1} > 1$: very stable regime.

Note that the limits in this classification are not sharply defined, for instance [Högström \(1996\)](#) showed that $zL^{-1} > 0.5$ corresponds to a very stable regime.

In the weakly stable BL, the turbulence is more continuous in time and space and is more likely described by the existing similarity theory in both the outer layer and surface layer. This involves applying a small negative heat flux at the surface and/or imposing a high geostrophic wind (u_g) ([Mahrt 1998](#)). The very stable BL is highly intermittent with turbulence and is less continuous in time and in space and is no longer described by the similarity theory. Horizontal layering can develop.

Values for the runs simulated in this study show that zL^{-1} are below 1 except for simulations that suffer from runaway cooling, the values of which are larger than 1. Moreover, it can be seen that decreasing geostrophic wind speed generates faster stable conditions than decreasing surface heat flux.

Friction velocity increases and geostrophic wind increases in both stability regimes approximately by the same order of magnitude.

Regarding the time step, it decreases as the wind speed increases as expected. All runs satisfied the minimum time step required (see Section [4.3](#)).

ID	$\overline{w\theta_s} [mKs^{-1}]$	$\delta [m]$	$zL^{-1} [-]$	$u_* [ms^{-1}]$	$dt [sec.]$	$\overline{\Delta\theta_s} [K]$
N	0.0	741	0.00	0.21	0.50	-
S0	-0.005	720	0.15	0.15	0.50	0.6
S1	-0.01	90	0.44	0.14	0.49	1.9
S2	-0.02	-	1.00	0.13	0.47	5.9
S3	-0.03	-	3.55	0.10	0.44	17.0
S4	-0.04	-	5.40	0.09	0.41	35.5
S5	-0.05	-	16.15	0.08	0.40	65.2

Table 4.5: Bulk parameters of the simulated BL evolution computed for the last hour of each section and for $u_g = 8 \text{ ms}^{-1}$. Runs that suffer from runaway cooling (according to Eq. 4.26) are labelled in bold.

ID	$\overline{w\theta_s} [mKs^{-1}]$	$\delta [m]$	$zL^{-1} [-]$	$u_* [ms^{-1}]$	$dt [sec.]$	$\overline{\Delta\theta_s} [K]$
N	0.0	947	0.00	0.26	0.40	-
S1	-0.005	257	0.05	0.22	0.40	0.3
S2	-0.01	130	0.18	0.18	0.39	1.3
S3	-0.02	105	0.43	0.17	0.38	3.6
S4	-0.03	100	0.67	0.17	0.36	7.5
S5	-0.04	90	1.27	0.15	0.35	15.0
S6	-0.05	85	3.73	0.12	0.34	33.8

Table 4.6: Same as Table 4.5, but for $u_g = 10 \text{ ms}^{-1}$.

ID	$\overline{w\theta_s} [mKs^{-1}]$	$\delta [m]$	$zL^{-1} [-]$	$u_* [ms^{-1}]$	$dt [sec.]$	$\overline{\Delta\theta_s} [K]$
N	0.0	980	0.00	0.32	0.35	-
S1	-0.005	973	0.03	0.27	0.34	0.3
S2	-0.01	260	0.07	0.25	0.33	0.9
S3	-0.02	125	0.22	0.22	0.32	2.7
S4	-0.03	124	0.35	0.22	0.30	5.4
S5	-0.04	115	0.49	0.21	0.29	9.3
S6	-0.05	105	0.82	0.20	0.30	15.7

Table 4.7: Same as Table 4.5, but for $u_g = 12 \text{ ms}^{-1}$.

ID	$\overline{w\theta_s} [mKs^{-1}]$	$\delta [m]$	$zL^{-1} [-]$	$u_* [ms^{-1}]$	$dt [sec.]$	$\overline{\Delta\theta_s} [K]$
N	0.0	1140	0.00	0.37	0.29	-
S1	-0.005	1095	0.02	0.33	0.29	0.2
S2	-0.01	375	0.04	0.31	0.28	0.7
S3	-0.02	225	0.10	0.28	0.27	1.9
S4	-0.03	150	0.19	0.26	0.26	4.1
S5	-0.04	145	0.28	0.25	0.26	7.1
S6	-0.05	135	0.40	0.24	0.25	11.2

Table 4.8: Same as Table 4.5, but for $u_g = 14 \text{ ms}^{-1}$.

4.5.2 Mean and Turbulent Vertical Structure

With a horizontally homogeneous surface layer, the main direction of variability is in the vertical direction, so here the influence of atmospheric stability on the vertical structure of the atmosphere through inspection of several vertical profiles is analyzed. The Figures in sections 4.4 to 4.7 show the vertical profiles of:

- Horizontal wind speed ($U = (\overline{u^2} + \overline{v^2})^{1/2}$),
- Wind angle ($\arctan(\frac{v}{u})$),
- Turbulent Intensity, $TI = \frac{\sqrt{\frac{2}{3}TKE_{total}}}{U}$
- Non-dimensional horizontal kinematic shear stress ($(\overline{wu^2} + \overline{wv^2})^{1/2}u_*^{-2}$),
- Potential temperature (θ),
- Brunt-Väisälä frequency (N), $N^2 = (g/\theta_0)(d\theta/dz)$

for each geostrophic wind prescribed and as the surface heat flux decreases (starting from the neutral regime). Profiles presented are both time-averaged (last hour of each section) and averaged over horizontal directions.

From the evolution of the mean wind speed profiles, there can be seen a clear increase of the shear (increase of wind speed with altitude) as the stability increases, which displays a low level jet (LLJ) near the top of the boundary layer in the last stage of stable profiles.

Numerous authors have reported evidence of marine low level jets in offshore flow (e.g. [Smedman et al. \(1995\)](#); [Källstrand \(1998\)](#)). The low level jet is a well known phenomenon due to inertial oscillation caused by frictional decoupling from the surface when warm air flows over cooler water. The decoupling occurs because the turbulence near the surface collapses partly due to buoyancy destruction. Sea breeze circulation and thermal winds are other phenomena which may give rise to LLJs ([Bergström 2001](#)). The low level jet can act as a second source (beyond the production by near surface wind shear) of turbulence in the SBL due to the shear above and below the wind speed maximum that is detached from the surface ([Mahrt 1998](#)).

Wind shear (both magnitude and direction) under stable conditions is much larger in comparison to that during neutral conditions. These results are similar to those from [Jiménez and Cuxart \(2005\)](#),

except in this study the simulation exhibits much stronger gradients close to the surface and therefore a lower low level jet (LLJ) maximum position due to the lower surface roughness length.

The asymmetry of the incoming wind flow will make the rotor blades in the upper rotational sector, due to higher wind speed, more exposed to higher loads than in the sector near the ground. A similar asymmetry is produced by crosswinds which are caused by fast changes in wind direction.

The angle between the surface wind direction increases with stability and does not change significantly when the geostrophic wind increases for a given surface vertical temperature flux. Values obtained range from about 11° in the neutral regime to about 30° in the stable regime.

As expected, the turbulence intensity (TI) is strongest near the ground, decreasing from a high to zero. An evident reduction of TI as stability increases is apparent.

The non-dimensional horizontal shear stress decreases almost linearly with height from a maximum value of about 1.0 on the surface to zero at the top of the boundary layer for all stabilities. This is an indication that the flow has reached a quasi-steady state. Moreover, as the boundary layer gets more stable, the shear stress decreases.

The potential temperature profiles clearly show a two-layer structure in the stable profiles: a stable surface layer with strong gradients and a constant θ layer (zero gradient). The strength of inversion increases with the (negative) surface heat flux which thereby leads to an increased suppression of turbulent mixing and hence a decay in the turbulent layer height. The most stable case presents drastic changes in the profiles of potential temperature and wind speed, experiencing runaway cooling.

Brunt-Väisälä, or buoyancy frequency, is the frequency at which a vertically displaced parcel will oscillate within a statically stable environment. Higher stabilities near the surface support a wider range of frequencies than those higher up in the SBL. In a residual layer of neutral stratification, vertically propagating waves are not supported. Waves that propagate upward within the SBL eventually reach the level where their frequency matches the ambient Brunt-Väisälä frequency, at which point they reflect back down towards the ground. Waves within the SBL are thus trapped between the ground and the neutral layers above, resulting in horizontally propagating waves. In the simulations, the frequency has a maximum value near the ground, decreasing with height. Moreover, the Brunt-Väisälä frequency increases as the geostrophic wind decreases (more stable regime).

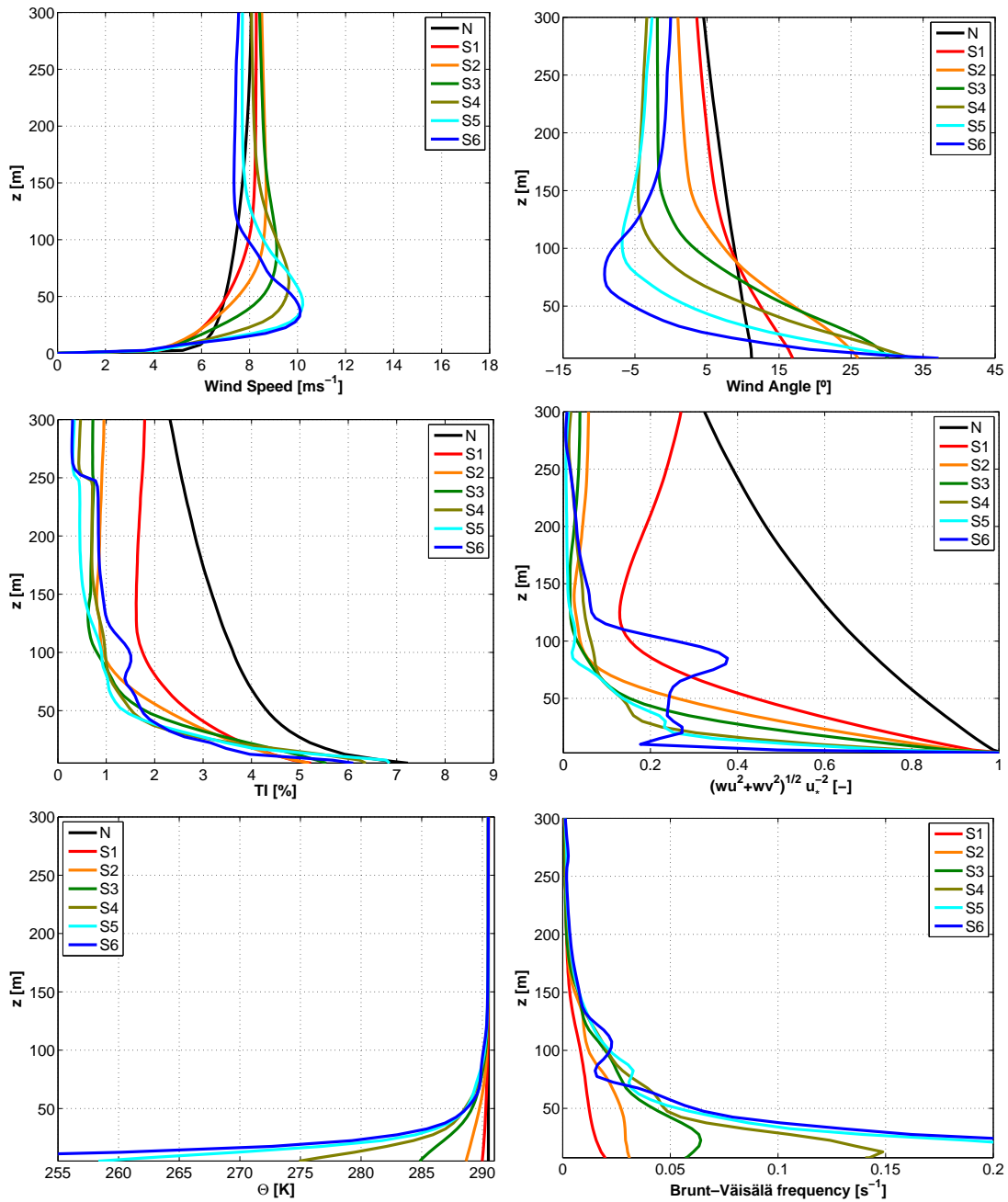


Figure 4.4: Evolution of the mean profiles as surface cooling increases: wind speed (left-side upper panel), wind angle (right-side upper panel), Turbulent Intensity (TI) (left-side middle panel), non-dimensional horizontal kinematic shear stress (right-side middle panel), potential temperature (θ) (left-side lower panel) and Brunt-Väisälä frequency (N) (right-side lower panel) for $u_g = 8 \text{ ms}^{-1}$. See Table 4.5 for acronyms shown in the legend. Note that only the first 300 m above the surface are plotted.

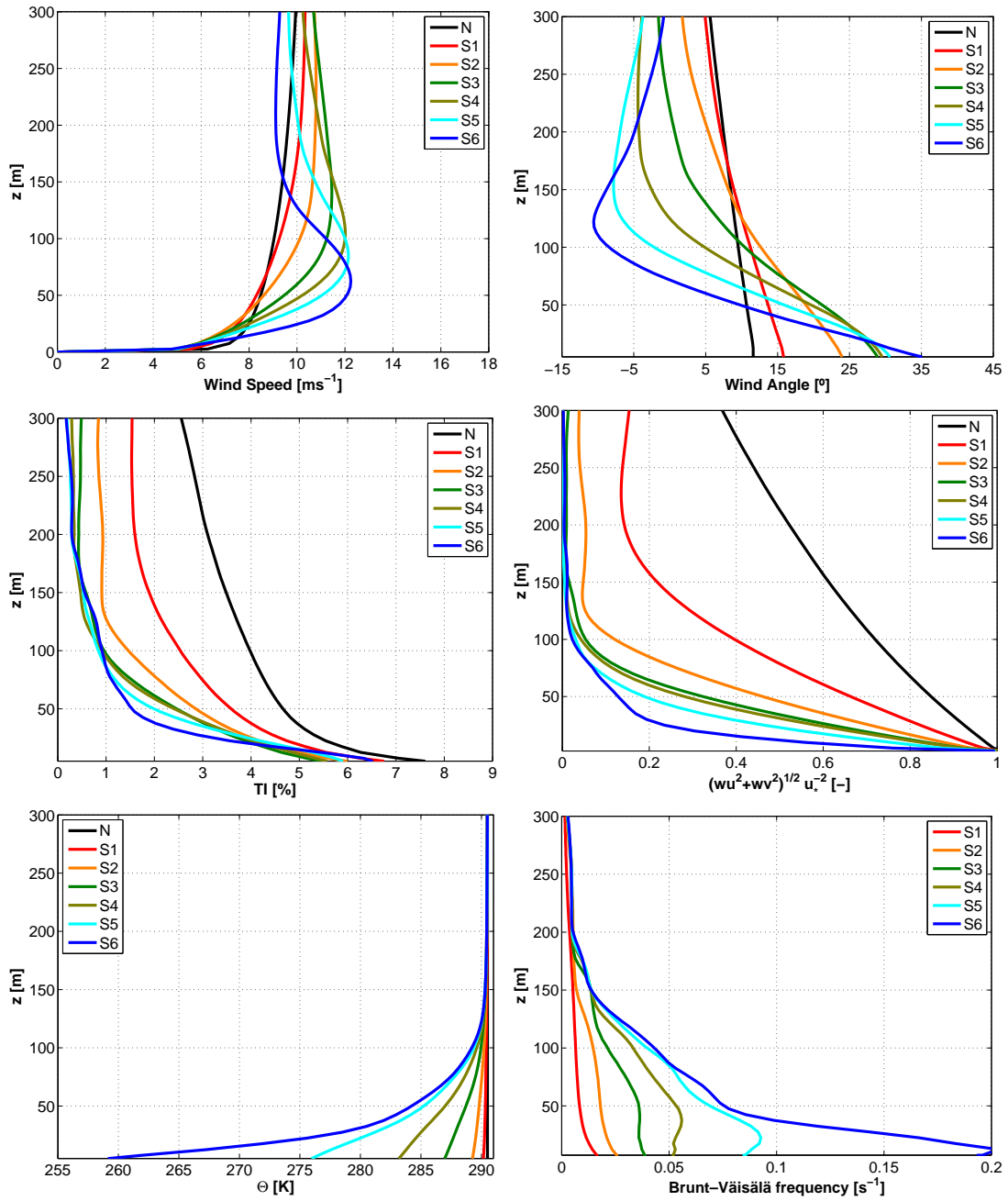


Figure 4.5: Same as Figure 4.4, but for $u_g = 10 \text{ ms}^{-1}$.

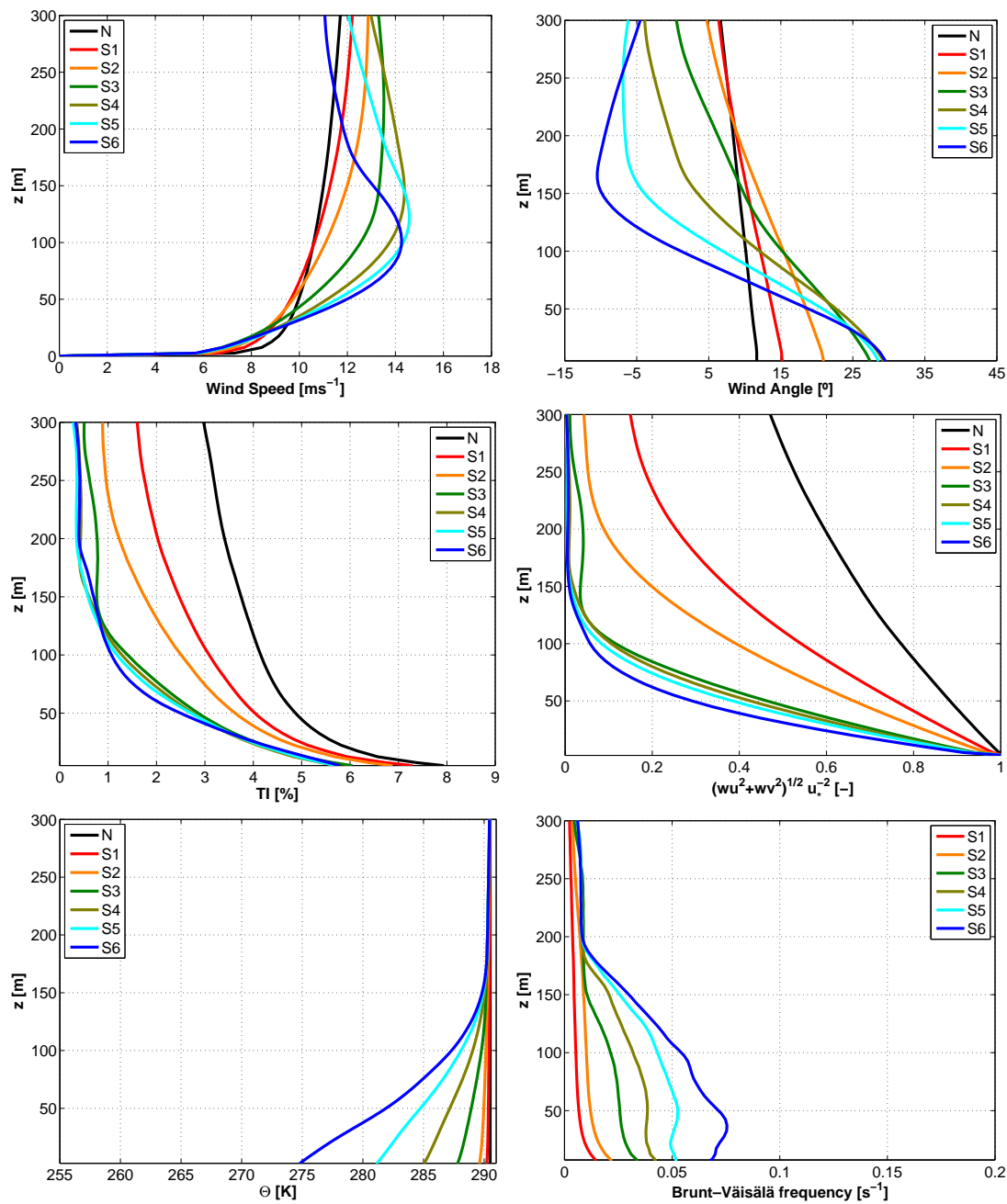


Figure 4.6: Same as Figure 4.4, but for $u_g = 12 \text{ ms}^{-1}$.

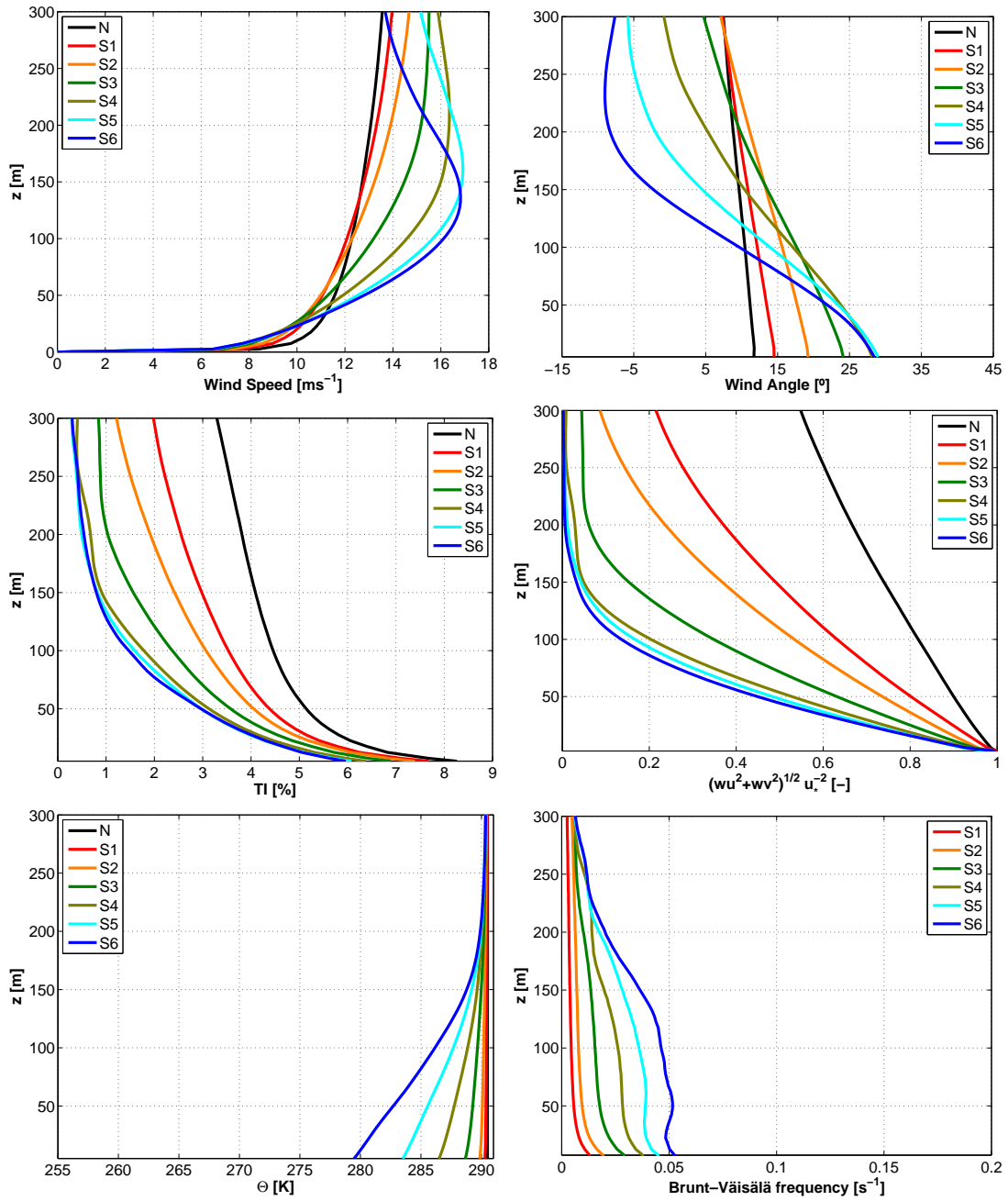


Figure 4.7: Same as Figure 4.4, but for $u_g = 14 \text{ ms}^{-1}$.

4.5.3 Contribution of SGS Parameterization to Total TKE

It is well known that the size of the dominant turbulent eddies decreases as the atmospheric stability increases and therefore smaller grid resolutions are necessary in order to resolve most of the turbulent motion of the flow. Otherwise the contribution of the SGS model comes into play and the results can be quite sensitive to the type of parameterization used to represent the subgrid scales (smaller than the grid size). A stable LES intercomparison study ([Beare et al. 2006](#)), where PALM code was also involved, highlighted that LESs of moderately SBLs are quite sensitive to SGS models at a relatively fine resolution of 6.5 m.

Near the surface, it is expected that as the stability increases from neutral to stable, the ratio between the SGS scale and the total TKE (right side of the panel) should increase for a fixed geostrophic wind. It can be clearly seen that for the most stable cases simulated, the opposite is found (even for cases that exhibit no runaway cooling) where a collapse of the SGS-total TKE near the surface is presented. This unphysical behaviour of the profiles has been found by other authors ([Mason and Derbyshire 1990](#); [Andr n 1995](#); [Saiki et al. 2000](#)) and has been attributed to a failure of the SGS model. That problem is a well-known limitation in modeling where such a flow conditions are very difficult to simulate due to the intermittent nature (turbulent burstings in the midst of a laminar flow) of the turbulence.

Therefore, in order to simulate the most stable cases (which do not suffer from runaway cooling), a higher resolution should be used.

In the neutral regime, the contribution of the SGS scale is below 9% (at 32.5 m) decreasing with height for all geostrophic winds simulated. This means that most of the turbulence in this regime is resolved. Whereas for the stable case 'free of any problem' the contribution of the SGS scale is below 15% (at 32.5 m).

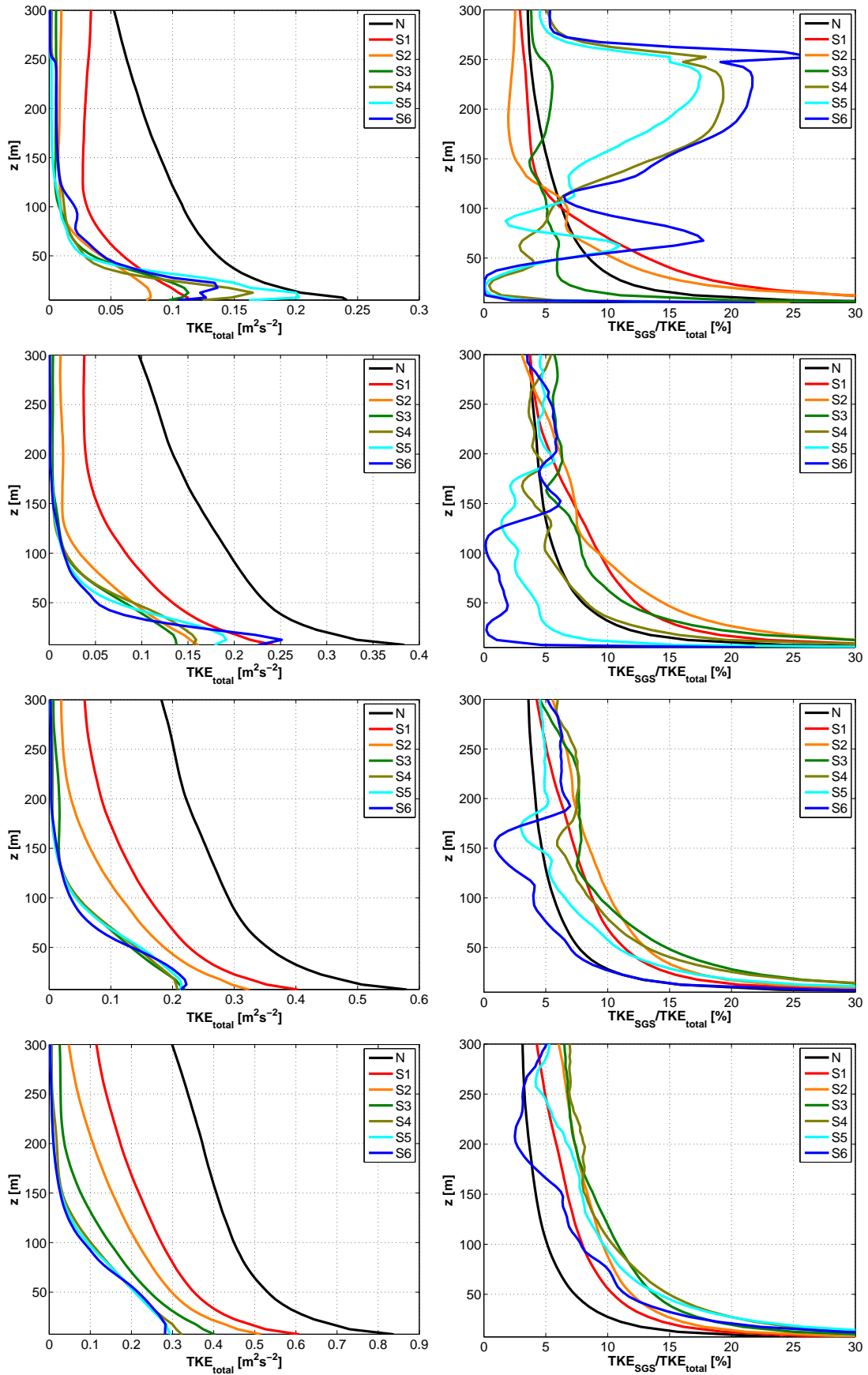


Figure 4.8: Mean profiles of the total TKE (left side of the panel), subgrid TKE (middle panel) and ratio between TKE_{SGS} and TKE_{total} (right side of the panel) for increasing u_g (Top to bottom). Blue (black) lines correspond to neutral (stable) regime.

Therefore, taking into account the findings reported above, simulations free of known failures (run-away cooling and SGS model) are summarized in the following table:

$u_g [ms^{-1}]$ \ $w\theta_s [mKs^{-1}]$	N	S1	S2	S3	S4	S5	S6
8	x	x					
10	x	x	x				
12	x	x	x	x			
14	x	x	x	x	x		

Table 4.9: Runs with an 'X' correspond to successful runs (free of known failures).

4.5.4 Sensitivity Tests

Several factors have to be considered when selecting the domain size and resolution of an LES simulation. First, the domain size should be large enough that the largest eddies in the boundary layer are resolved and such that a further increase in domain size does not change significantly the mean and turbulent fields. Second, the resolution should be fine enough that further increase of resolution does not change the turbulent statistics drastically. Third, when computational cost is unaffordable, one has to balance the above factors and sensitivity studies with an appropriate domain size and grid resolution for the case simulated have to be performed.

4.5.4.1 Sensitivity to Grid Size or Resolution

Insensitivity to grid resolution is always desirable in LES modelling and its existence is usually attributed to the strength of the SGS model (Beare and Macvean 2004).

In order to test the effect of grid size on the simulation results, a higher resolution simulation was performed for a geostrophic wind of $u_g = 10 \text{ ms}^{-1}$ (see Table 4.3, run NS5). Then, profiles of the horizontal wind speed, potential temperature and total TKE and SGS TKE profiles as the stability increases (Figs. 4.9 and 4.10) are compared with the grid resolution used in this study (5 m).

As the resolution increases, the height of the jet maximum in the wind speed profiles decreases and its magnitude increases, which leads to higher shear values. This behaviour is clearly seen in Fig. 4.9 (upper panels) for the most stable cases (from S3 to S6). Therefore, the simulation at 2 m resolution generates more stable conditions near the surface than the one at 5 m resolution

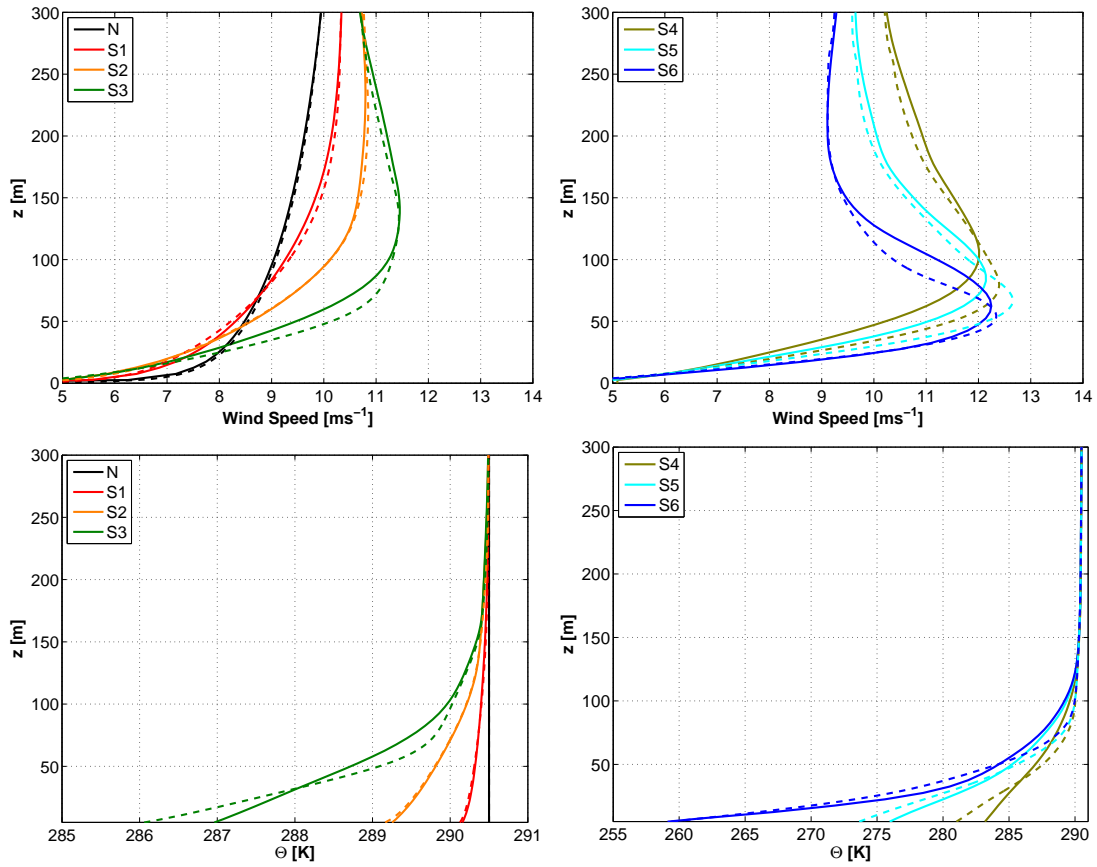


Figure 4.9: Mean profiles at 5 m resolution (solid lines) and 2 m resolution (dashed lines) of horizontal wind speed (upper panel) and potential temperature (bottom panel)

since the cooling in the first level is greater, corresponding to a decrease in the SBL depth (Fig. 4.9 (bottom panels)).

For the neutral regime as expected, close to the surface the subgrid (SGS) contribution to energy is larger in the 5 m resolution simulation than with 2 m resolution, since at lower resolution a larger part of the TKE is resolved leading to an increase in the total TKE. Moreover, TKE_{total} in the higher resolution model is smaller than in the lower resolution model since the stability is larger as for TKE_{SGS} because the contribution of smaller scales is reduced when the resolution increases.

The comparison also shows that for the most stable cases the TKE_{SGS} profiles (see Figure 4.10 (bottom panels) stabilities from S4 to S6) do not fall to zero for the 2 m resolution run which could be attributed to that the contribution of the sub-grid model is lower at higher resolution. However, even a resolution of at least 1 m or less would be necessary to check whether the code is able to simulate these stabilities.

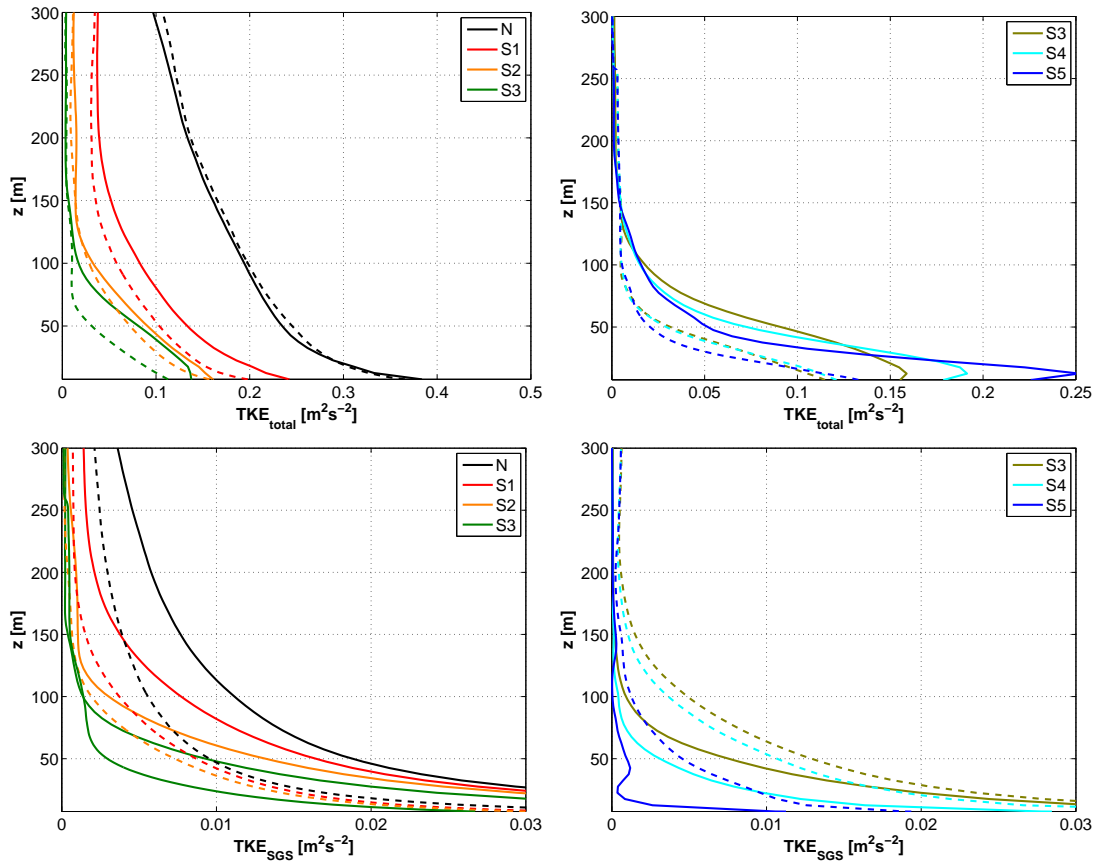


Figure 4.10: Mean profiles at 5 m resolution (solid lines) and 2 m resolution (dashed lines) of TKE_{total} (upper panel) and TKE_{SGS} (bottom panel)

These results are in qualitative agreement with many LES studies (e.g. (Beare and Macvean 2004; Jiménez and Cuxart 2005)).

4.5.4.2 Sensitivity to Domain Size

Here, it is focused on the neutral regime and perform a sensitivity analysis to assess the sensitivity to domain size, since the eddies in the neutral regime are larger than those in the stable regime and therefore a larger domain is required. Note that in the stable regime, domain sizes of $400\text{ m} \times 400\text{ m}$ are used in LES studies. (Beare and Macvean 2004) found no significant effects on simulation statistics when doubling the domain size for stable intercomparison.

Simulations N7, N8 and N9 (see Table 4.3) are used to investigate the effect of model domain size on the LES solutions by plotting the profiles of horizontal wind speed, resolved non-dimensional variances and total (solid lines) and SGS scale (dashed lines) TKE (Fig. 4.11). For the results shown, the domain height is fixed at 1400 m and the domain width is expanded by increasing the number of computational cells by a factor of 2.

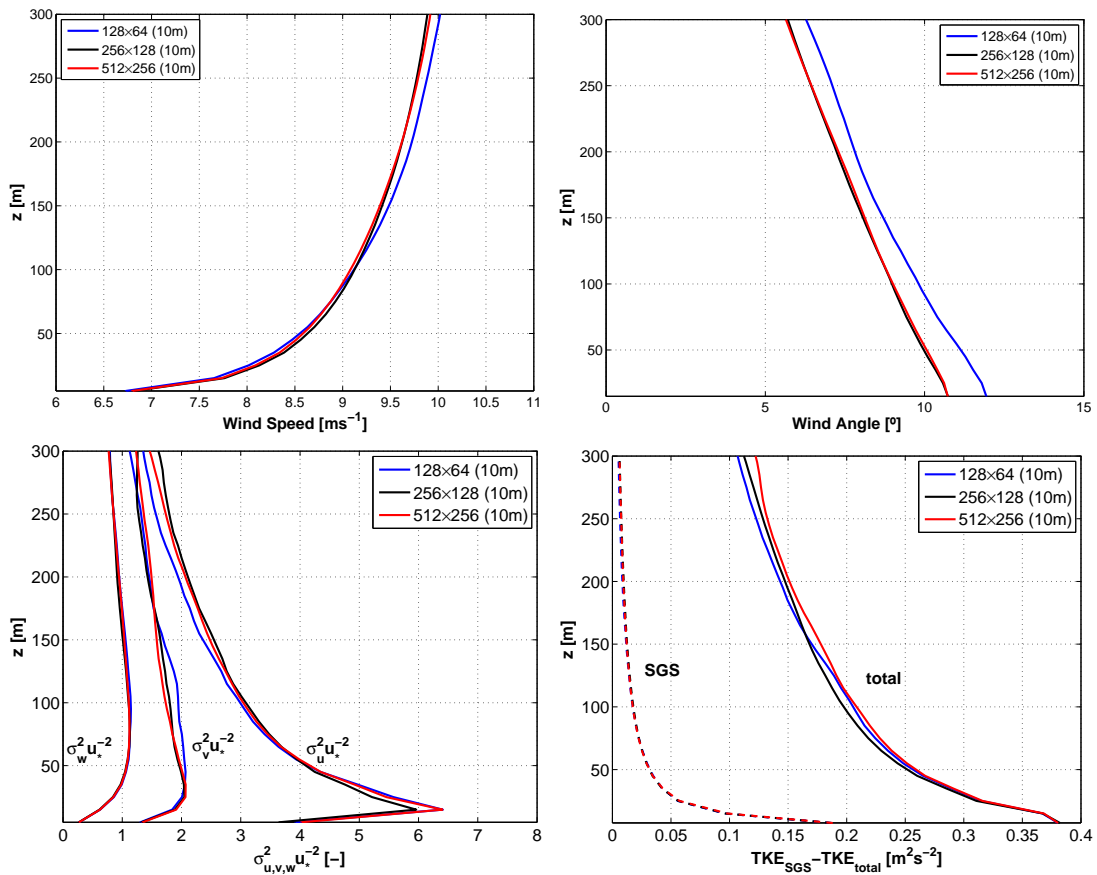


Figure 4.11: Profiles of Horizontal wind speed (upper left panel), wind angle (upper right panel) resolved non-dimensional variances (lower left panel) and total and SGS TKE (lower right panel) with varying domain width. Legend shows number of grid points in the horizontal direction. In brackets the resolution used.

It can be seen that there is a negligible change between the largest domains and it is expected that the TKE is slightly higher for the largest domain since the model is expected to resolve larger eddies containing more energy. On the contrary, for smaller domain sizes, larger differences are found, for instance the wind direction has an offset of about 1.5° compared to the other domain sizes.

With regard to the three components of resolved velocity fluctuations (variances), in neutrally stratified ABL flows, the observed peak normalized velocity variances occur near the surface and are of magnitude: $\sigma_u^2/u_*^2 \sim 6.0$, $\sigma_v^2/u_*^2 \sim 2.02$ and $\sigma_w^2/u_*^2 \sim 1.12$.

In general, no big differences between the three domain sizes investigated were found, however it was decided that simulations with a horizontal domain with 256×128 grid points (10 m grid size) was sufficient.

Note that for the higher grid resolution (2 m) considered in Section [4.5.4.1](#), a smaller domain was used as a compromise between domain size and resolution limited by computational time.

4.6 Flow visualization: Eddy structure

Coherence and anisotropy structures within the PBL play an important role in the dynamics and energetics of flow and have been widely studied by several authors (Brown 1972; Deardorff 1972; Etling and Brown 1993; Andr en et al. 1994; Lin et al. 1997; Drobinski et al. 1998; Drobinski and Foster 2002; Carlotti 2002; Drobinski 2004; Foster et al. 2006; Drobinski et al. 2007). Streak-like structures are known to occur in shear-driven flows.

Kelley (1994); Hand et al. (2003); Kelley et al. (2005) identified large loading events resulting from the interaction between the turbine rotor and organized or coherent turbulent structures in the inflow.

A common way to show the eddy structures within the ABL is through horizontal and vertical cross-sections of the u -component of the wind. Figs. 4.12 to 4.15 present the evolution of the eddy structures as the stability increases for $u_g = 10 \text{ ms}^{-1}$ and for $u_g = 14 \text{ ms}^{-1}$ (left (right) side of the panel respectively in each figure). For each column of figures, three horizontal cross-sections at three different heights encompassing the rotor plane (bottom tip at 32 m, hub height at 90 m and top tip at 100 m) as well as the corresponding vertical cross-section, are presented. This set of figures corresponds to neutral (Fig. 4.12), $\overline{w\theta}_s = -0.01 \text{ mKs}^{-1}$ (Fig. 4.13), $\overline{w\theta}_s = -0.02 \text{ mKs}^{-1}$ (Fig. 4.14), $\overline{w\theta}_s = -0.03 \text{ mKs}^{-1}$ (Fig. 4.15) stability regimes.

Deardorff (1972) found that, close to the surface for neutral stratification, the downstream velocity component (\overline{u}) eddies were organized into distinct 'bands' or 'strikes' orientated 15° right of the surface wind (Northern Hemisphere). Moreover, the length of the band was much larger than its width because of wind shear effects. For the \overline{v} component, eddies were more irregular but usually elongated with a greater angle of alignment of about 25° .

A similar picture is found in Figure 4.12 for the cross-sections of \overline{u} closer to the surface. It shows the existence of organized areas aligned with the mean wind of alternating low and high wind speed.

In the stable regime, a similar picture is found as in the neutral regime, with the size of the eddies smaller as the stability increases for a given u_g , since the stability stratified conditions tend to suppress turbulence. When the shear increases, the flow is more turbulent and less stable. Therefore, the eddy size is larger for $u_g = 14 \text{ ms}^{-1}$ than for $u_g = 10 \text{ ms}^{-1}$. Regarding the vertical cross-sections, under weakly stable conditions the turbulent motions occupy the whole domain whereas under conditions of greater stability the turbulence is confined to levels close to the ground.

It can be seen how the lower tip of the rotor (bottom tip) can experience velocity differences of 2 ms^{-1} compared to the upper tip (top tip). The velocity differences are more pronounced as the stability increases.

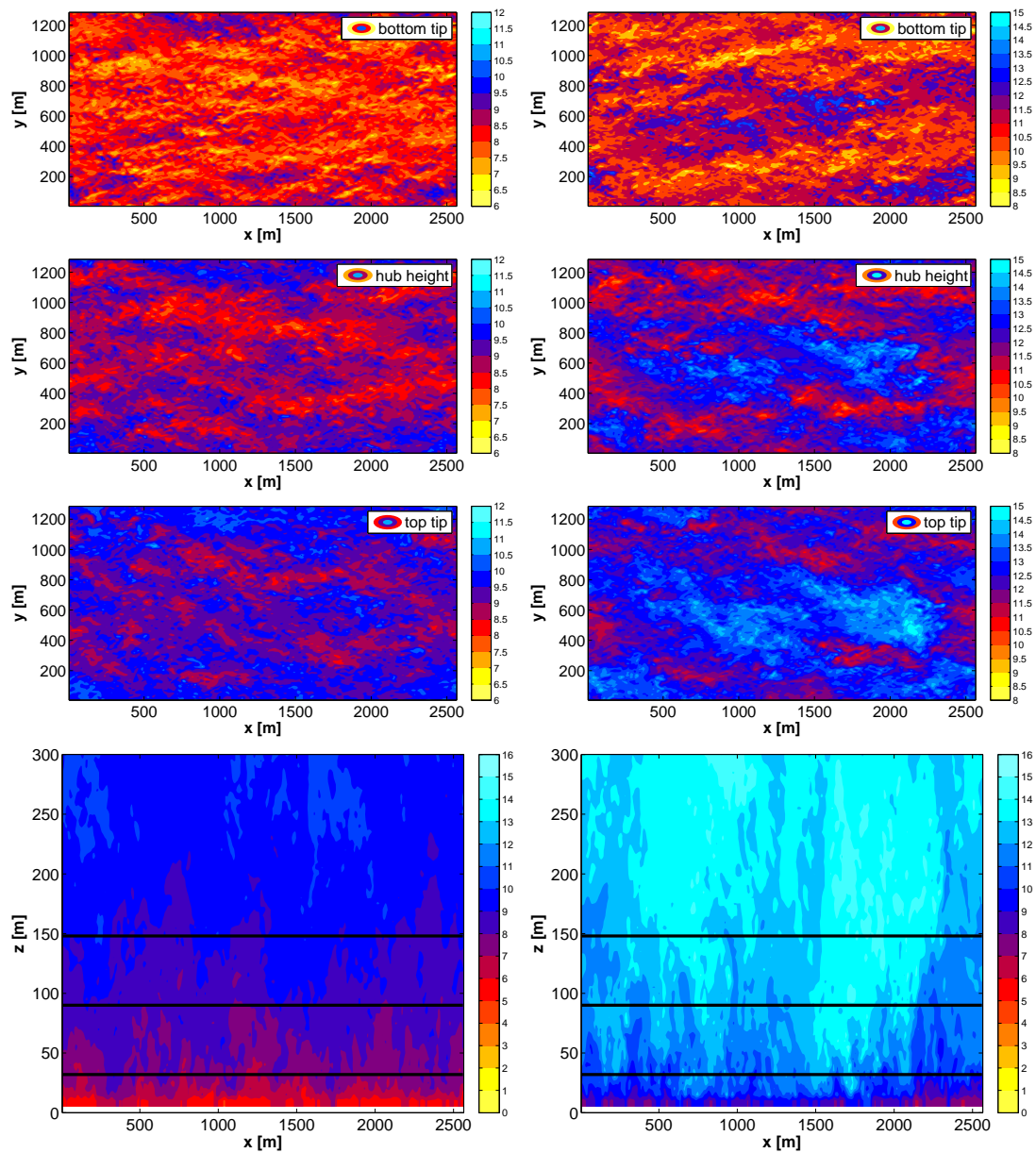


Figure 4.12: Horizontal cross-sections (three first rows) at 40 m, 100 m and 160 m heights and vertical cross-sections at $y = 600$ m for the longitudinal wind velocity (u [ms^{-1}]) for neutral conditions ($u_g = 10 \text{ ms}^{-1}$ (left-side panel) and $u_g = 14 \text{ ms}^{-1}$ (right-side panel)).

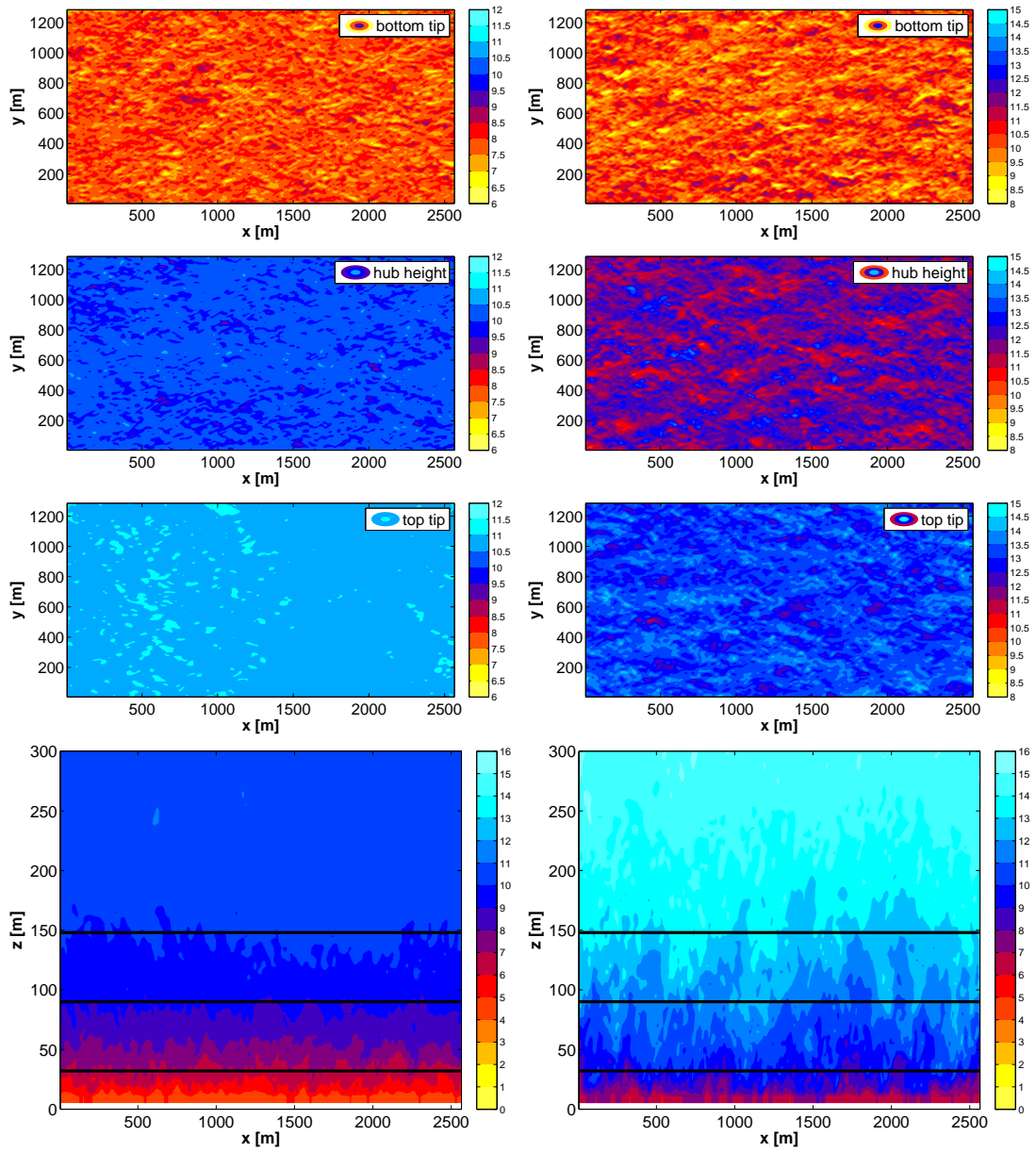


Figure 4.13: Same as Figure 4.12, but for $\overline{w\theta}_s = -0.01 \text{ mKs}^{-1}$.

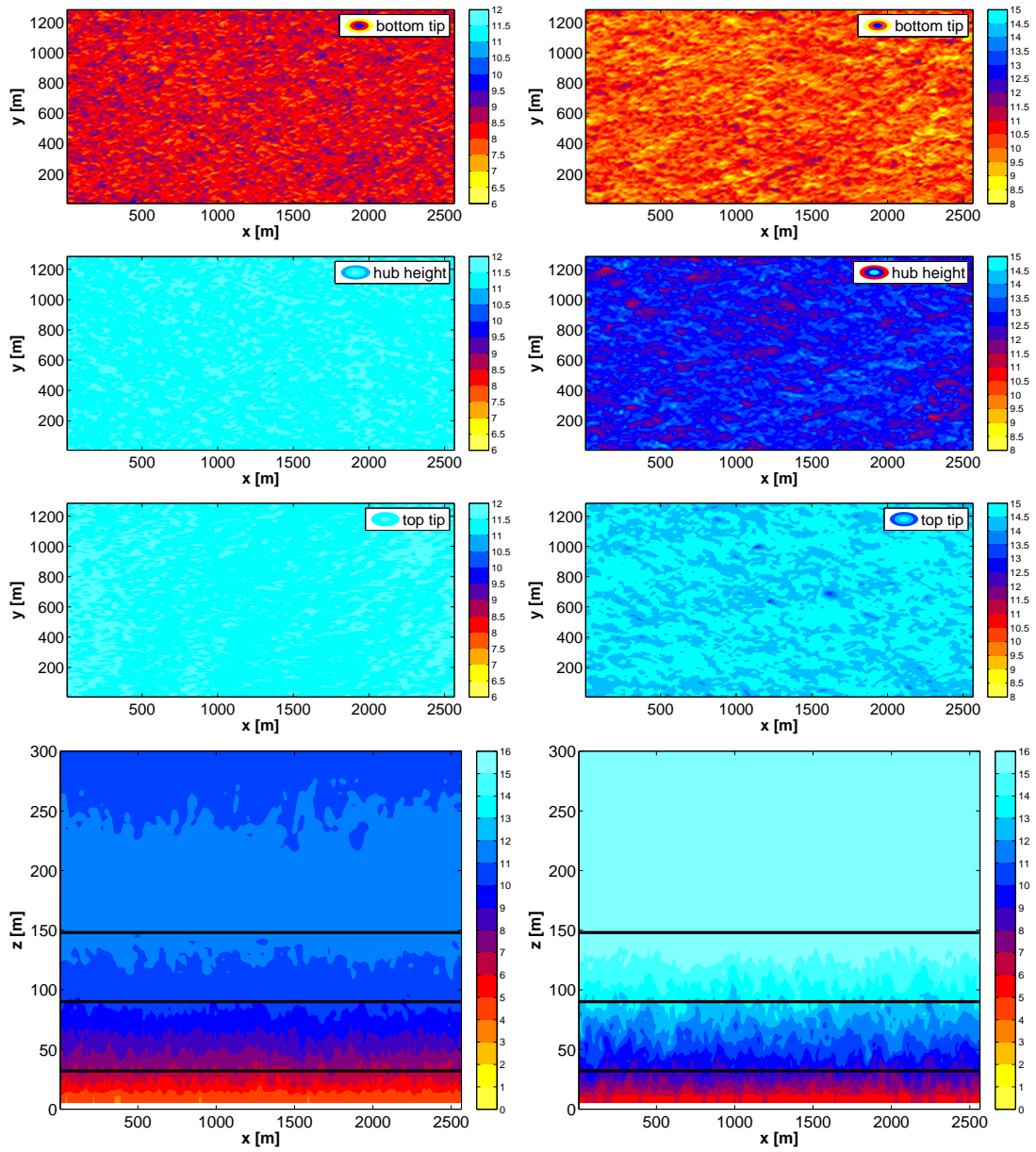


Figure 4.14: Same as Figure 4.12, but for $\overline{w\theta}_s = -0.02 \text{ mKs}^{-1}$.

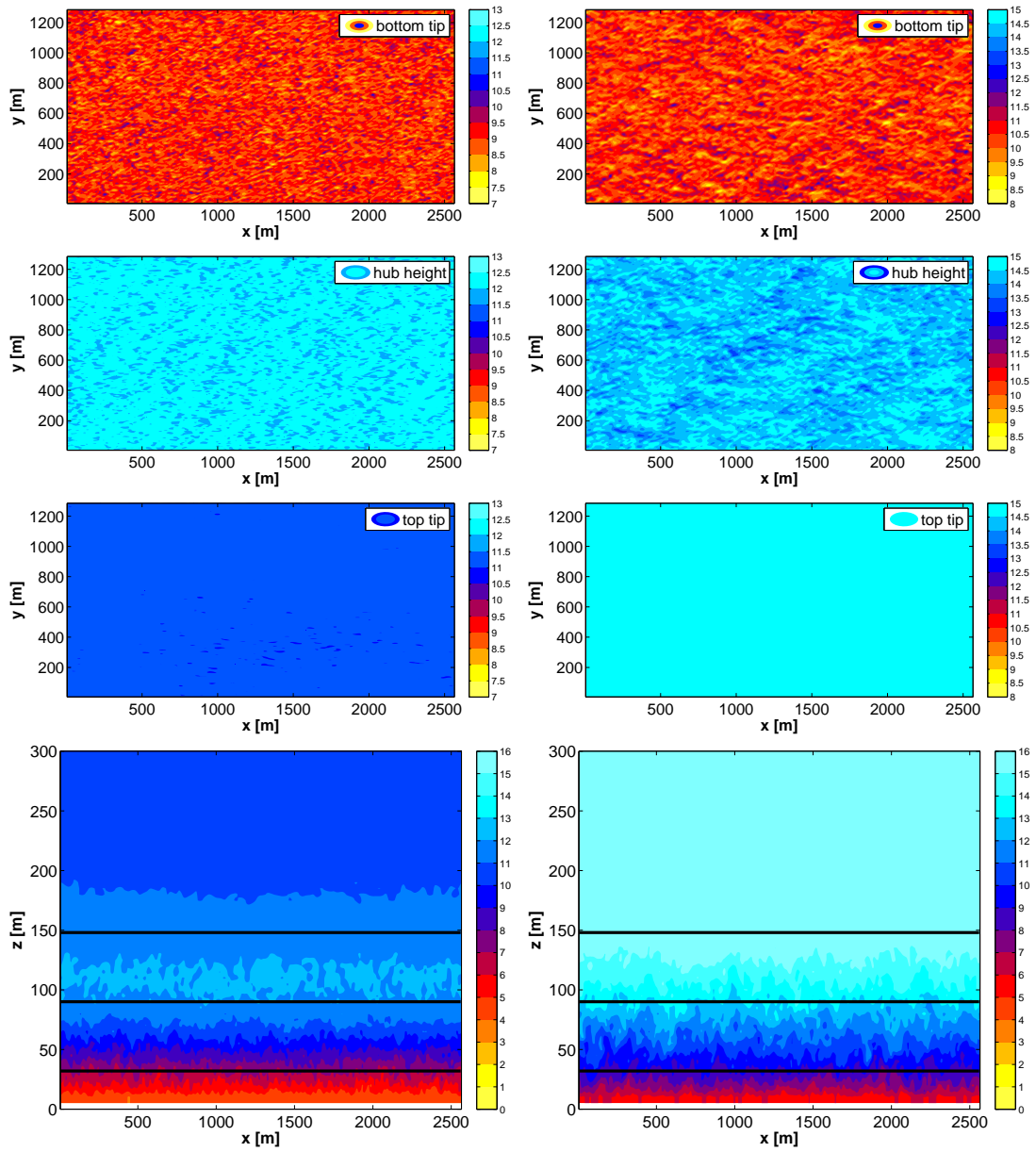


Figure 4.15: Same as Figure 4.12, but for $\overline{w\theta}_s = -0.03 \text{ mKs}^{-1}$.

4.7 Summary

In this Chapter, the results of three-dimensional LES simulations of an ABL evolving from Neutral to Stable conditions have been presented, using the PALM code.

Based on the simulations carried out, the following conclusions can be drawn:

- The simulations carried out correspond to an idealized ABL where the most important flow forcing parameters are: geostrophic wind, thermal stratification (through the prescribed heat flux) and surface roughness.
- Overall, the model which is based on a TKE turbulence closure with M-O theory (MOST) used for fluxes at the surface, reproduces the flow characteristics well, however under conditions of high stability, unphysical profiles in both mean and turbulent quantities are found.
- A resolution of 5 m and domain size of $2560 \times 1280 \times 1371$ turned out to be adequate from a numerical point of view to represent the essential features of the ABL under Neutral and Stable conditions up to weakly stable cases.
- To perform LESs of the most stable cases presented in this study, a smaller resolution must be used to reduce the influence of the SGS parameterization.
- Results are consistent with the features of a Marine Atmospheric Boundary Layer. Moreover, our results are in qualitative agreement with many LES studies.
- Furthermore, a robust LES database has been generated which can be compared to experimental data to check the performance of the model as will be done in the next Chapter.
- As elaborated throughout the Chapter, the LES modelling framework shows great promise in addressing several practical wind energy related issues.

Chapter 5

Comparison: LES-simulations and FINO1-observations

5.1 Introduction

In this Chapter, the results of the LES simulations performed in the previous chapter are compared with the FINO1 offshore dataset.

Note that since the LES simulations performed in this work are idealized cases, a quantitative agreement between the simulation results and the observations is not expected but this will give us a guide to the relative performance and sensitivity of the model.

The present chapter is split into two major parts. In the first part, a comparison through vertical profiles (bulk properties of the flow) is carried in the neutral and weak-moderate stability regimes. Three parameters of importance in wind energy applications are considered, namely vertical wind shear, wind direction and turbulence intensity. In this comparison, the two-year period FINO1 dataset analyzed in Chapter 3 is used, where data are classified according to the two forcing parameters applied in the LES simulations (surface heat flux and geostrophic wind). This comparison is limited to the three sonic anemometers available at the FINO1 location and placed at heights of 40, 60 and 80 m.

In the second part, we complement the mean profile comparison with an basic analysis (using a time series) which accounts for unsteady effects due to turbulence and according to a statistical approach (spectral analysis, probability density function and autocorrelations) in order to get a more complete picture of the flow. Moreover, a brief investigation of the strength of LES data to solve short-term

extreme wind events (wind gust) is carried out. This part is confined to the neutral regime where a representative neutral case was selected from the FINO1 database.

The Chapter is organized as follows. In Section 5.2, the comparison of profiles is presented and discussed together with a description of the data selection procedure. In Section 5.3, the power spectral density (5.3.1), probability density function (5.3.2) and autocorrelation (5.3.3) are evaluated to obtain quantitative information regarding flow structure. The Chapter concludes with a brief investigation of the strength of LES data to solve short-term extreme wind events (wind gust) in Section 5.4. Finally, a summary is presented in Section 5.5.

5.2 Profile Comparison

In this section, the LES simulations performed in Chapter 4 are tested along vertical profiles by selecting three parameters of considerable practical interest from a wind energy perspective: vertical wind shear (α), relative wind direction ($dir_{ref} - dir$) and Turbulent Intensity (TI) defined as follows:

- vertical wind shear,

$$\alpha = \sqrt{\left(\frac{\partial u}{\partial z}\right)^2 + \left(\frac{\partial v}{\partial z}\right)^2}, \quad [s^{-1}] \quad (5.1)$$

- relative wind direction

$$dir = dir_{ref} - dir, \quad [^\circ] \quad (5.2)$$

- Turbulent Intensity (TI)

$$TI = \frac{\sqrt{\frac{2}{3}TKE_{total}}}{U}, \quad [\%] \quad (5.3)$$

where TKE is the Turbulent Kinetic Energy (total=resolved + SGS scale), U is the horizontal wind speed ($U = \sqrt{u^2 + v^2}$), and dir the horizontal wind direction ($dir = atan(\frac{v}{u})$) with dir_{ref} the wind direction at a reference height (here at 30 m) and z the height above the surface. Only the three sonic anemometers available on the FINO1 mast and placed at 40, 60 and 80 m above sea level are used for this comparison. The anemometers were sampled with an accuracy of $\pm 0.1 \text{ ms}^{-1}$ (see Chapter 3 for further details). Note that 40 m is relatively far from the surface which means that the influences of the known shortcomings of the SGS-scale model closer to the surface should be avoided.

5.2.1 Data Selection for Comparison Purposes

In order to perform the comparison between observations (FINO1) and the idealized LES simulations, the FINO1 database (analyzed in Chapter 3) is classified according to surface heat flux and geostrophic wind. The classification is accomplished in two steps:

- First of all, FINO1 surface heat flux data ($\overline{w\theta_s}$) are categorized into different ranges according to the surface heat flux forcing applied in LES simulations (see Table 5.1). As before, the class N represents neutral stability; while S3 represents a moderately stable regime. The comparison, for the stable regime, has been restricted to prescribed surface heat fluxes up to -0.03 mKs^{-1} .
- Second, the observed wind at 30 m is used (since no estimates of geostrophic winds are available from FINO1 data) to perform a subclassification for each range of observed surface heat flux (Table 5.1) according to the simulated wind at 27.5 m (the closest height to 30m) (see Table 5.2).

Moreover, rain-period and humidity above 70% are excluded. This methodology is similar to the one used by Jimenez (2005).

Class	Range of $\overline{w\theta_s}$
N	$[-0.0025, +0.0025)$
S0	$[-0.0075, -0.0025)$
S1	$[-0.0150, -0.0075)$
S2	$[-0.0250, -0.0150)$
S3	$[-0.0350, -0.0250)$

Table 5.1: Surface heat flux ($\overline{w\theta_s}$) range considered.

It is worth mentioning that only 60% of the data remain from the 2-year dataset (after data post-processing and excluded periods) where about 40% correspond to values of surface heat fluxes $\overline{w\theta_s} \leq 0.035 \text{ mKs}^{-1}$ (neutral and stable conditions).

u_g	N	S0	S1	S2	S3
8	[6.0, 7.0)	[6.0, 7.0)	[6.0, 7.0)	[6.5, 7.5)	[8.0, 9.0)
10	[7.5, 8.5)	[7.0, 8.0)	[7.0, 8.0)	[7.5, 8.5)	[8.0, 9.0)
12	[9.0, 10.0)	[8.5, 9.5)	[8.5, 9.5)	[8.5, 9.5)	[9.0, 10.0)
14	[10.5, 11.5)	[10.0, 11.0)	[10.0, 11.0)	[9.5, 10.5)	[9.5, 10.5)

Table 5.2: 30 m wind speed ranges used to classify the FINO1 data according to the values obtained from the LES results at 27.5 m.

Note that runs suffering from runaway cooling or the SGS failure may have wrong wind speed values at 27.5 m. Nevertheless, this value is considered for the classification of the observations and then in the comparison.

After classification, the FINO1 dataset is drastically reduced. A large percentage of the remaining dataset corresponds mostly to simulations with higher geostrophic winds which have not been simulated here. Moreover, as was discussed in Chapter 3, strongly stable cases were not found in the

ID	$8ms^{-1}$	$10ms^{-1}$	$12ms^{-1}$	$14ms^{-1}$
N	10.2	13.8	15.7	10.7
S0	5.2	6.1	7.8	13.4
S1	0.3	1.5	3.8	4.9
S2	0.1	0.2	1.4	2.5
S3	0.0	0.0	0.6	1.8

Table 5.3: *Percentage of the number of observed events [%] in FINO1 that have been simulated with LES.*

FINO1 dataset (see Fig. 3.6 in Chapter 3) and for that reason only a very low percentage of data are found for higher stabilities in Table 5.3. However, the number of cases that fall in categories where the LES suffers from runaway cooling is very small or non-existent. Due to low data availability, the profile comparison is restricted to values up to -0.02 mKs^{-1} surface heat flux (S2).

5.2.2 Results: Profile Comparison

A comparison of the profiles from the last hour of physical time in the LES simulations for each section (shown in blue) with those computed from FINO1 measurements (shown in red) is shown in Figs. 5.1 to 5.4). FINO1 data are depicted as bin-median values with bars representing one standard deviation of the data in each range (see Table 5.3). These profiles are depicted as the stability increases (up to -0.02 mKs^{-1}) and for all geostrophic wind cases simulated. Note that suspicious simulations due to either runaway cooling or failure of the subgrid model are shown in dashed blue lines (see the previous Chapter for more information).

The selection of these three parameters is motivated by the great importance of having detailed knowledge for wind turbine design applications as well as for a detailed calculation of the wind potential, especially for the large rotor diameters planned for offshore sites.

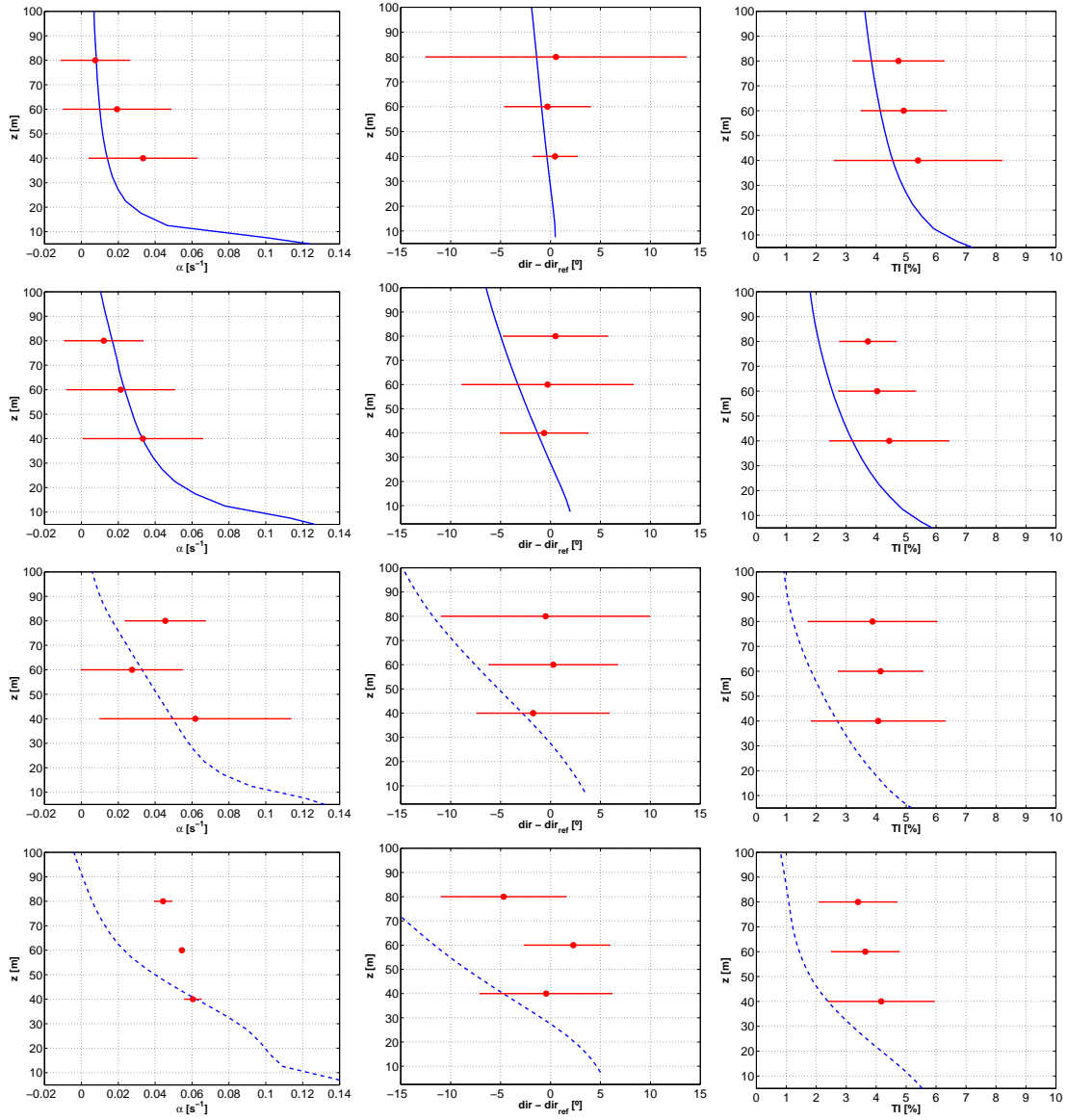


Figure 5.1: Comparison of profiles between simulated (blue) and measured (red) data for $u_g = 8 \text{ ms}^{-1}$. Vertical wind shear (left side of the panel), horizontal wind direction (middle side of the panel) and Turbulent Intensity (TI) (right side of the panel) as cooling surface increases: Neutral (first panel row), S0 ($\overline{w\theta}_s = -0.005 \text{ mKs}^{-1}$) (second panel row), S1 ($\overline{w\theta}_s = -0.01 \text{ mKs}^{-1}$) (third panel row) and S2 ($\overline{w\theta}_s = -0.02 \text{ mKs}^{-1}$) (fourth panel row). Profiles marked with blue dashed lines correspond simulations which suffer from runaway cooling or SGS failure.

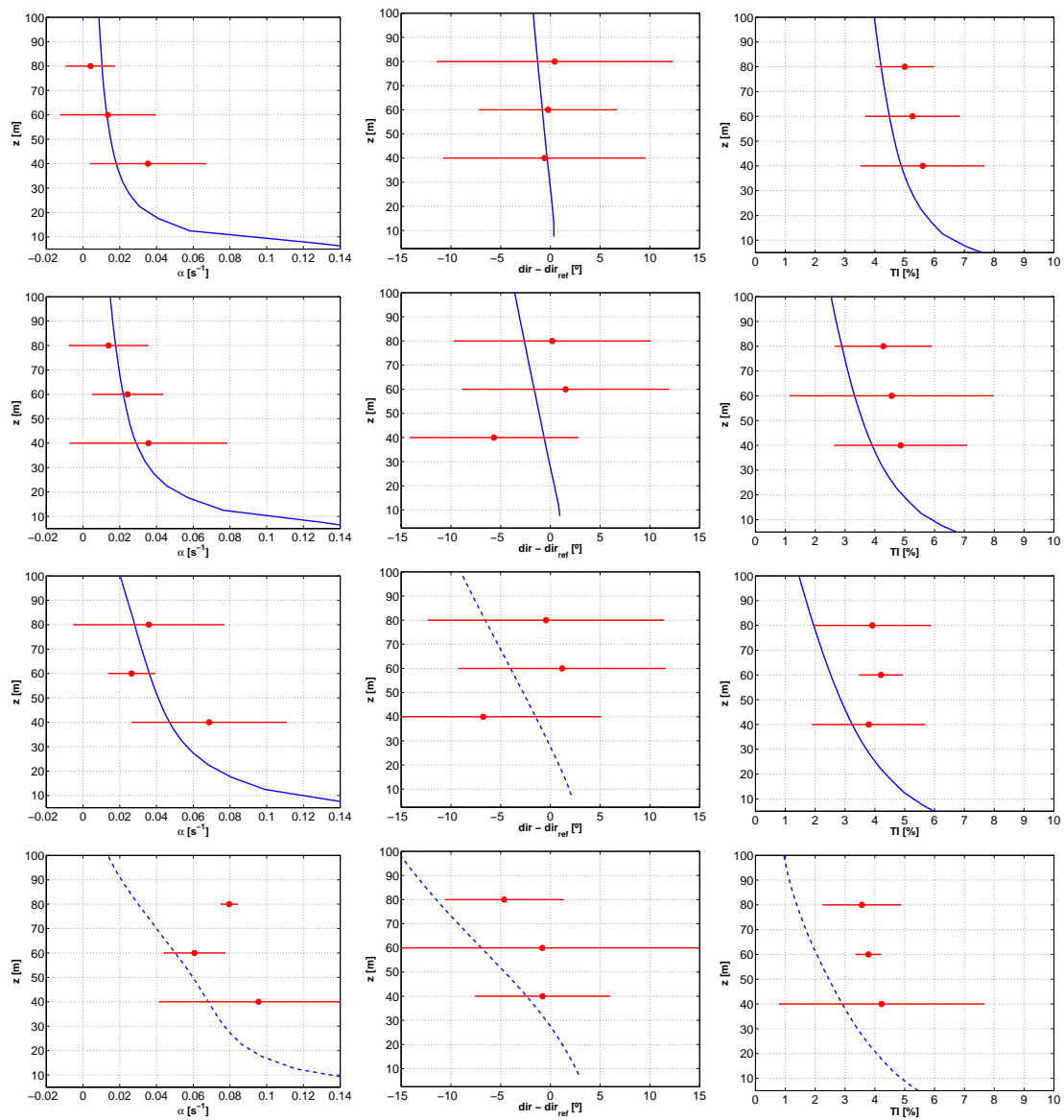


Figure 5.2: Same as Fig. 5.1, but for $u_g = 10 \text{ ms}^{-1}$.

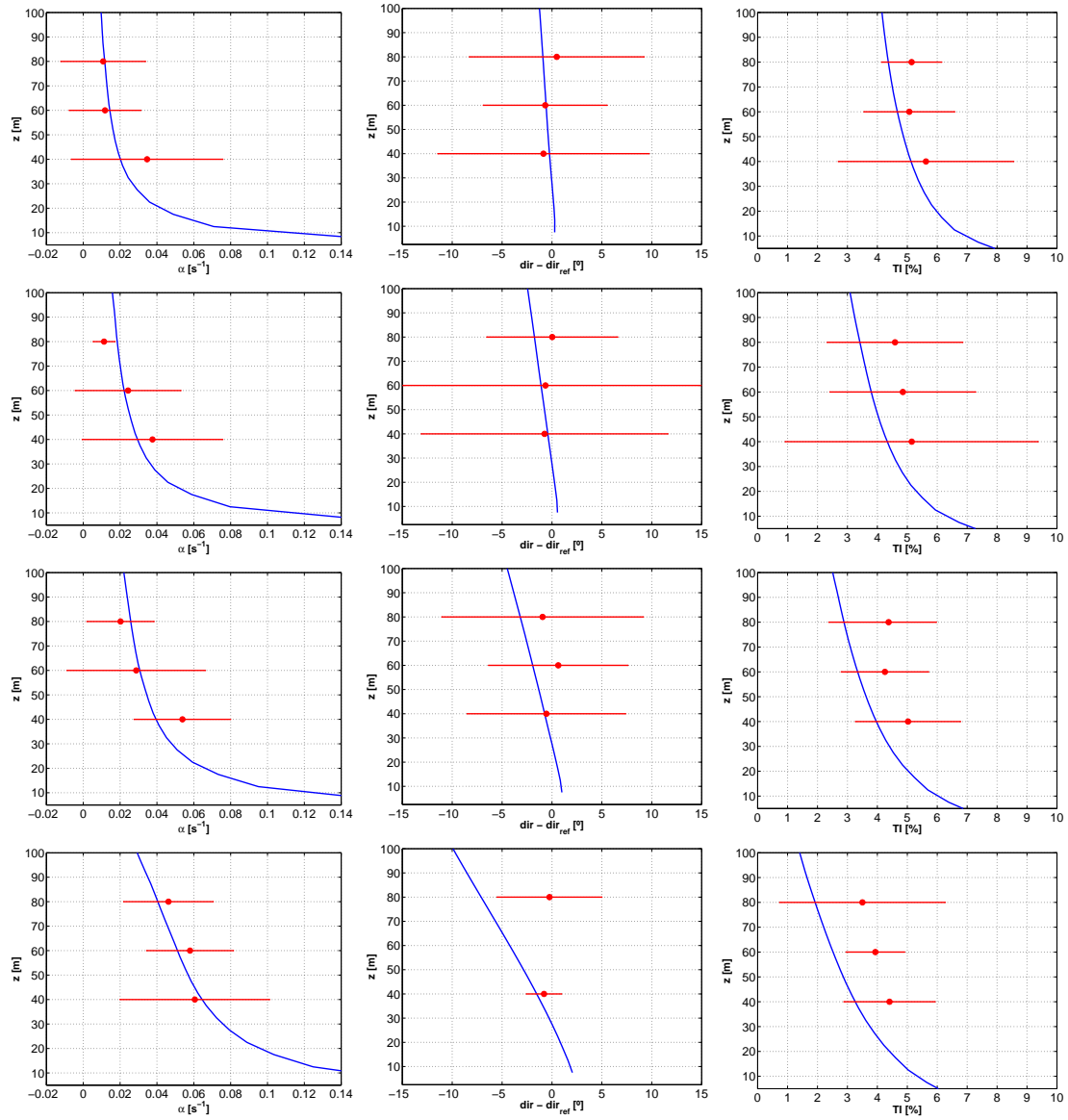


Figure 5.3: Same as Fig. 5.1, but for $u_g = 12 \text{ ms}^{-1}$.

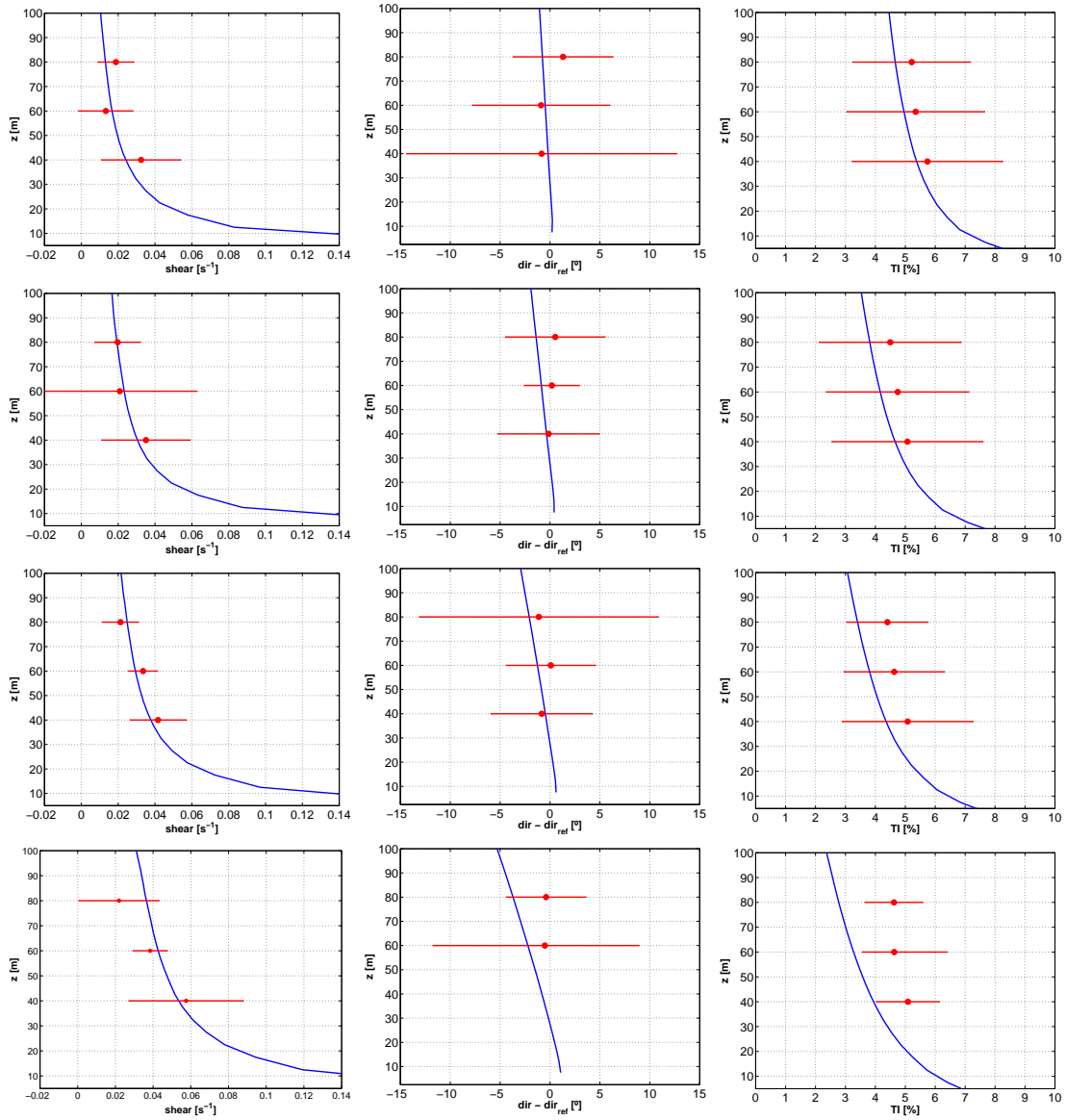


Figure 5.4: Same as Fig. 5.1, but for $u_g = 14 \text{ ms}^{-1}$.

Atmospheric measurements reveal a rather large scatter. This can be explained mainly by the complex interplay of different forces in the real atmosphere. Nevertheless, the qualitative agreement between both sets of data is rather good with most of the simulation results falling within the error bars of the FINO1 data. In general, neutral LES results agree better with observed data. Although, for moderately stable cases the comparison gives acceptable results. Keep in mind that the data bases are limited for most stable conditions and whether the comparison is truly representative should be treated with caution. Moreover, the calculation of the surface heat fluxes from the FINO1 data used for the data classification are in some ways not free of uncertainties and this can generate some discrepancies in the classification.

On the other hand, LES simulations have also several uncertainties and their results are sensitive to grid resolution and initial conditions, amongst others, especially under stable conditions (see section 'Sensitivity Tests' in chapter 4). Therefore, LES simulations must be considered also with error bars although here they are not shown because the sensitivity tests reported in the previous chapter were carried out only for $u_g = 10 \text{ ms}^{-1}$.

Generally, good agreement is found for wind shear values between the two datasets. As shown, wind shear is higher closer to the surface, decreasing with height. In comparison to land surfaces, the shear is clearly lower due to the very small surface roughness length used in the simulations to characterize offshore conditions. In both regimes, the vertical wind shear increases with geostrophic wind which is stronger under stable conditions as anticipated. Values of wind shear lie well below the wind energy IEC standard value considered for offshore conditions ($\alpha = 0.14$) (IEC61400-1 2005) at the heights considered.

The horizontal wind directions depend on roughness, latitude and turbulence and therefore they are lower than over land surfaces. On the other hand, angles do not change significantly when the geostrophic wind increases, for a fixed $\overline{w\theta}_s$. The profiles displayed in the figures show relatively good agreement. FINO1 shows an approximately constant variation with height for all cases whereas the simulations show a larger variation with height for the most stable case.

Lastly, as the geostrophic wind (u_g) increases, the surface roughness increases and so TI also increases in both regimes. Within the SBL, TI decreases as the stability increases, corresponding to an increase of $\overline{w\theta}_s$ for a fixed u_g or a decrease of u_g for a fixed $\overline{w\theta}_s$. For the NBL, TI increases as u_g increases. For all cases, the TI decreases towards the top, as the effect of surface roughness decreases. Moreover, TI values are much lower than over land surfaces and are lower than used in the standards applying to offshore conditions (12%).

It can be summarized that taking into account the different nature of both datasets, the qualitative agreement is very good where measured data are very close to simulated data. However, an increase of the LES resolution could improve the comparison with observations, especially for the stable case.

It is worth mentioning that the measured values shown in the profiles have been contrasted, whenever possible, with values reported in ([Türk and Emeis 2007](#)) which are based on the same measured database.

5.3 Further Analysis: Time Series

The profile comparison performed in Section 5.2 provided a measure of the mean characteristics of turbulent flow, although when information about unsteadiness (eddy structures) is desired, a statistical approach is required and therefore a time series is needed.

For this purpose, one point at the centre of the LES domain has been selected to generate a time series at 80 m and 40 m of the horizontal wind velocity components (longitudinal (u), transverse (v)) to compare with one-point FINO1 measurements. A neutral simulation for $u_g = 10 \text{ ms}^{-1}$ was chosen.

We are aware that for this study only one case has been selected from the FINO1 database although more cases are needed to consider the results to be statistically representative, however this study allows us to get a better understanding of the LES approach.

Special care has been taken to select a period that is 'comparable' with the 'idealized' LES simulation. The case selected for the comparison was September 10th 2005 from 12 00 to 15 00 UTC as representative for neutral conditions. The synoptic situation (from NCEP operational data base, not shown) was characterized by high pressure over the North Atlantic, therefore synoptic-driven events like fronts, rainfall, etc., were not present, and large-scale conditions were relatively homogeneous during the day. Moreover, from the FINO1 dataset, it was corroborated with almost zero heat flux and relative humidity below 70%. Mean velocity was about 9 ms^{-1} .

The following sections are divided into two parts: first the methodology is given and then results are presented and discussed. The sections cover: Power Spectral Density (PSD) (5.3.1), Probability Density Function (PDF) (5.3.2) and Autocorrelation (5.3.3). Moreover, a brief investigation into the ability of LES data to resolve short-term extreme wind events (wind gusts) is carried out (5.4).

5.3.1 Horizontal Wind Velocity Turbulence Power Spectrum

The Power Spectrum Density (PSD) of horizontal wind velocity fluctuations is evaluated in order to obtain qualitative information about the flow structure of these two types of data (simulations and measurements).

5.3.1.1 Spectrum Methodology

The methodology used for the computation of spectra is mainly based on the monographs of [Kaimal and Finnigan \(1994\)](#) and [Stull \(1998\)](#).

To transform the time series (simulations and observations) into the frequency domain, a Fast Fourier Transformation (FFT) technique is used. Before doing so, time series are linearly de-trended and mean value removed. Moreover, a tapered window is applied to minimize spurious frequencies in the spectral distribution which are caused by non-periodicity of the finite time series. To enhance the readability of the spectrum, a log-log scale is used.

The resulting power spectrum for horizontal wind ($S_U(f)$) then has the interpretation that $S_U(f)df$ is the variance of the horizontal wind due to eddies with frequency between f and $f + dk$. Variance is often used to quantify the 'energy' of a signal, thus the PSD displays the amount of wind energy over a range of frequencies. Similarly, the total variance of the horizontal wind is the area under the power spectrum:

$$\sigma_U^2 = \overline{U'^2} = \int_0^\infty S_U(f)df, \quad (5.4)$$

For comparison, power spectra are normalized by their variances so that they integrate to unity and conventionally are weighted by frequency (Eq. 5.5). Frequency weighting gives the spectra the units of variance (e.g. m^2s^{-2}) rather than variance per logarithmic frequency interval.

$$S_U(f)^* = \frac{f \cdot S_U(f)}{\sigma_U^2} \quad (5.5)$$

5.3.1.2 Spectrum Results

Comparison between different grid resolutions

Before we compare the simulations with observational data, the PSD of the LES simulation for three different grid resolutions (10 m, 5 m and 2 m) is obtained in order to facilitate the understanding of the LES filtering approach (Fig. 5.5). LES runs were performed with the same simulation parameters, only the grid resolution and therefore time-step was changed (only the 2 m resolution horizontal model dimensions were reduced to half for CPU-time reasons). The black line shows the theoretical

slope of a Kolmogorov inertial sub-range ($f^{-2/3}$). The vertical line is a roughly estimated cut-off frequency (f_{cutoff}) for the LES simulation which corresponds to the frequency at which the results of LES begin to decline in comparison with measurements. Theoretically, the simulation cannot predict frequencies higher than f_{cutoff} and, therefore, above that value it is better not to derive any conclusions from the spectra.

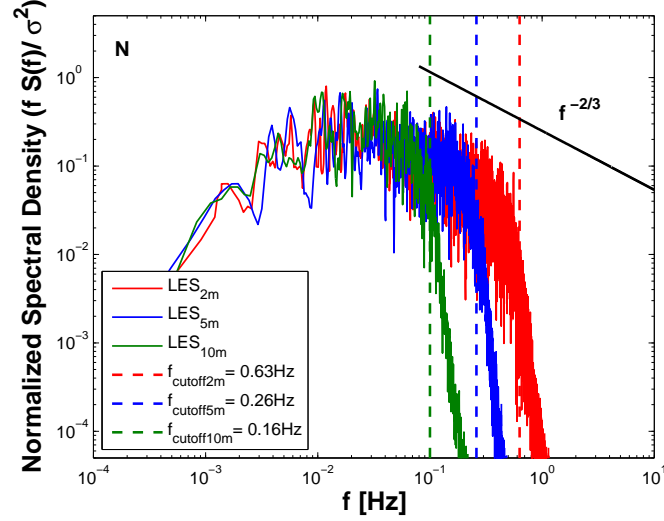


Figure 5.5: Normalized one-dimensional spectra of the horizontal wind velocity fluctuations for LES simulations: 10 m (green), 5 m (blue) and 2 m (red) grid spacing

As can be seen, at higher resolutions the resolved frequencies move into the inertial sub-range which is foreseen for LES simulations. This guarantees that a substantial portion of the turbulent energy is resolved by the model, since the maximum frequency f_{max} (which characterizes the size of the largest eddies contained in the flow) is much smaller than f_{cutoff} . Only when the grid spacing is smaller than the filter scale f_{cutoff} , is it expected to obtain grid size independent simulations, a basic requirement in numerical modelling (van Dop and Axelsen 2007), thus:

$$f_{res} \gg f_{cutoff} \gg f_{max} \quad (5.6)$$

or, in length scales:

$$\Delta \ll l_{cutoff} \ll l_{max} \quad (5.7)$$

as illustrated in Fig. 5.6 for the 2 m resolution simulation. Three vertical lines represent the spectral maximum f_{max} corresponding to the relevant length scale l_{max} , the frequency cut-off corresponding to filter scale l_{cutoff} and the frequency resolution f_{res} corresponding to grid spacing Δ .

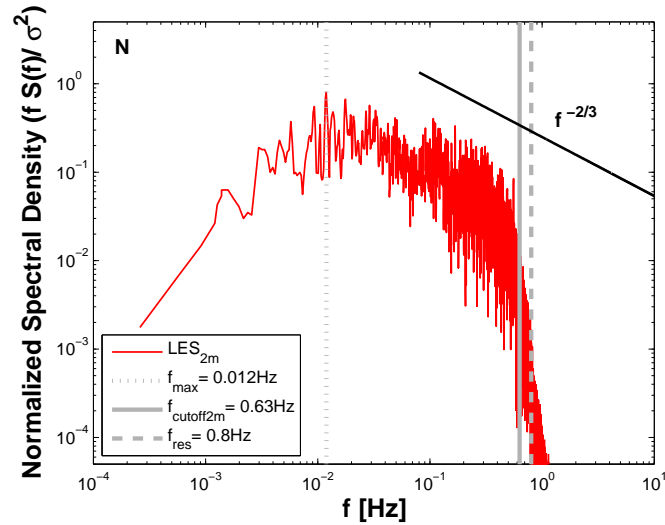


Figure 5.6: Normalized one-dimensional spectra of the horizontal wind velocity fluctuations for LES simulations: 2m (red line) grid spacing

The spectral fall-off in all spectra at frequencies considerably lower than the Nyquist frequency¹ is due to the implicit filtering of the discretization which dampens smaller scales. This means that the model dissipates kinetic energy at quite a high rate. At 10m resolution no sign of the inertial sub-range is found (see Fig. 5.5).

In order to calculate the size of the eddies, Taylor's frozen turbulence assumption is used and it is assumed that the turbulent structures are advected past the sensor at the mean wind speed \bar{U} , enabling us to transform frequency into streamwise wavenumber k (i.e. wavenumber in the direction of the mean wind) or wavelength λ using $k = \frac{2\pi}{\lambda} = \frac{2\pi f}{\bar{U}}$. For 2 m the highest resolved wavenumber is $\frac{1}{2\Delta}$ with $\Delta = 2$ m the grid resolution, which means that two computational grids are required to solve a turbulent eddy of 2 m.

Comparison between 2 m resolution LES-simulation and FINO1 data

PSD obtained from the FINO1 data and LES simulation (2m resolution) is shown in Fig. 5.7 in the neutral regime. In addition, a Kaimal model spectrum (Kaimal et al. 1972), commonly used in wind energy (IEC61400-1 2005), is plotted for reference, taking the following form:

$$\frac{f \cdot S(f)}{\sigma^2} = \frac{a \cdot f}{(a + b \cdot f)^{\frac{5}{3}}} \quad (5.8)$$

¹The Nyquist frequency is a fundamental limit to frequency information which can be extracted from a time series of finite frequency (length).

where a and b are coefficients which depend on the mean speed and the length scale of the turbulence eddies (Burton et al. 2001).

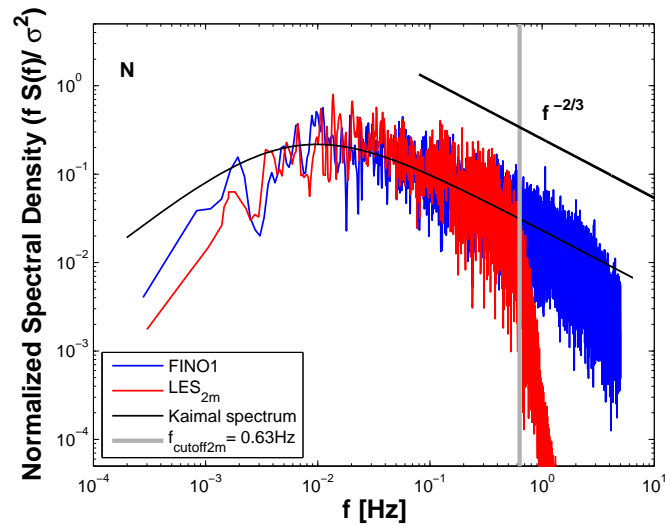


Figure 5.7: Normalized one-dimensional spectra of the horizontal wind velocity fluctuations: LES simulations (blue) and FINO1 data (red)

Due to the limited resolution of the grid, the turbulent spectra from the LES simulations do not show the extended inertial range found in the measured data, as anticipated. However, at low frequencies, the spectral shape of the simulation follows measurements reasonably well (Fig. 5.7).

As discussed in (Gluhovsky and Agee 1994), field data must be filtered in order to make meaningful comparisons with LES model results. They propose the need for high-pass filtering of field data in order to eliminate the effects of larger frequency structures that might be present, which are not allowed in the more limited LES model domain. Although for a comparison of second-order moment statistics, the data should not only be subjected to high-pass filtering (because of the limited model domain), but also to low-pass filtering (because of the grid size) (Agee and Gluhovsky 1999).

In this study, data filtering is achieved by using a top-hat filter at the cut-off frequency (f_{cutoff}) at which the results of the LES begin to decline in comparison with the measurements as explained before. From here onwards, the comparison between the two data sets will be carried out with LES simulations and FINO1-filtered time series.

5.3.2 Probability Density Function of the Horizontal Wind Velocity

From the Probability Density Functions (PDFs), the probability for each value is considered (whereas from the LES profiles each value is assumed to have the same probability). Since the mean values can be studied directly from the LES mean profiles, here we concentrate on the tails of the PDFs, which correspond to extreme events with low probability.

In this section, we look at the PDFs of horizontal wind velocity fluctuations contained in LES simulations and FINO1 measurement time series at 80 m and 40 m heights. The shape of the PDFs will be explained through inspection of the statistical moments.

5.3.2.1 Methodology

A random variable x (for instance, the horizontal wind velocity fluctuation) can be plotted as a probability distribution by splitting the overall range of values of the random variable into a number of class intervals (or bins). The vertical axis then represents the probability of occurrence of the random variable for a given class interval. If the number of observations of the random variable is increased indefinitely (to infinity) and the class width correspondingly approaches zero, the probability distribution will approach a continuous curve. When the height of such a curve is scaled so that the area underneath the curve is equal to unity, a probability density function results, as defined in Eq. 5.9 where $P(x)$ denotes the PDF. The probability (P) that the random variable x falls within the range $x_1 < x < x_2$ is given by integrating the PDF between the limits x_1 and x_2 (Eq. 5.10)

$$\int_{-\infty}^{\infty} P(x) dx = 1 \quad (5.9)$$

$$P(x_1 < x < x_2) = \int_{x_1}^{x_2} P(x) dx \quad (5.10)$$

Since, in the present study, the time series (LES and FINO1) are made over a finite sampling interval, the probability density functions represent only finite approximations to the theoretically continuous probability density function.

In order to better contrast differences between the two distributions and their Gaussian distributions, the PDFs are normalized as follows:

$$P(x) = P\left(\frac{x - \bar{x}}{\sigma_x}\right) \quad (5.11)$$

where σ_x and \bar{x} are the standard deviation and mean of the flow variable x . Normalization centralizes the distribution so that the mean is equal to zero. This allows a better comparison of different PDFs. To inspect the tails of the PDFs (which correspond to extreme events with low probability) a log coordinate axis (Probability) is used. Notice that the exponential tails are linear using this graphical representation.

From the PDFs, it is possible to derive the mean values of different powers of x , called moments (Tennekes and Lumley 1972) and defined as:

$$\bar{x} = \int_{x_1}^{x_2} xP(x) dx \quad (5.12)$$

$$\sigma_x^2 = \overline{x^2} = \int_{x_1}^{x_2} (x - \bar{x})^2 P(x) dx \quad (5.13)$$

$$S_x = \frac{\overline{x^3}}{\sigma_x^3} = \frac{1}{\sigma_x^3} \int_{x_1}^{x_2} (x - \bar{x})^3 P(x) dx \quad (5.14)$$

$$K_x = \frac{\overline{x^4}}{\sigma_x^4} = \frac{1}{\sigma_x^4} \int_{x_1}^{x_2} (x - \bar{x})^4 P(x) dx \quad (5.15)$$

The first moment is the familiar *mean* value (Eq. 5.12), the second (central) moment is the *variance* (Eq. 5.13) which indicates the mean-square departure from the mean value. The square-root of the variance is the standard deviation σ_x . The third moment is the *Skewness* (Eq. 5.14) which measures the degree of asymmetry of the distribution about its mean, where $S_x = 0$ indicates symmetry (e.g. Gaussian distribution), $S_x > 0$ indicates a longer tail to the right of the mean, and $S_x < 0$ indicates a longer tail to the left of the mean. And the fourth moment is the *Kurtosis* or flatness factor (Eq. 5.15) which is a measure of the 'peakedness' of the PDF. For a Gaussian distribution, the kurtosis factor is 3. If $K_x < 3$, the PDF has shorter tails and a wider mean region, and if $K_x > 3$ the PDF has longer tails and a thinner mean region.

5.3.2.2 Results

The PDFs for the normalized horizontal wind velocity fluctuation time series of the LES simulation (blue dotted line) and FINO1 measurements (red dotted line) at 40 m, 80 m as well as their differences are shown in Fig. 5.8. To inspect the tails of the distributions, figures are plotted on semi-logarithmic axes.

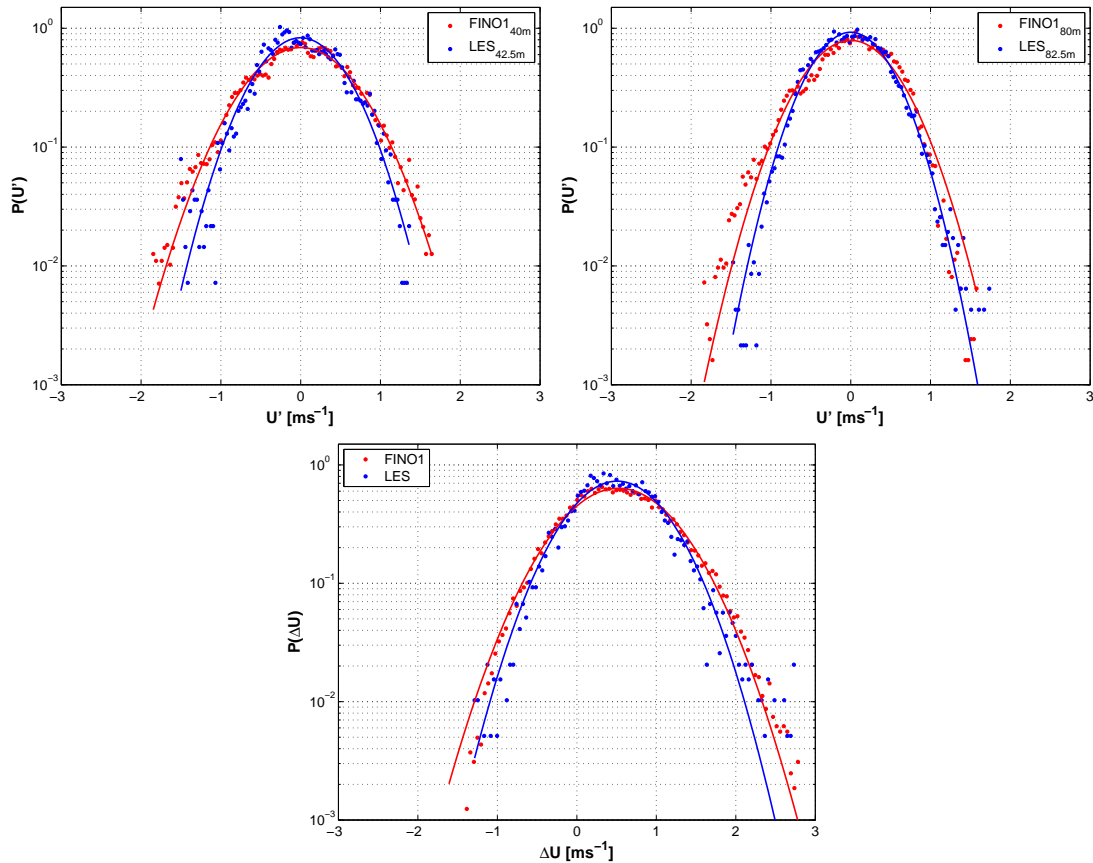


Figure 5.8: PDFs of the horizontal wind velocity fluctuations at 40 m (upper left panel) and at 80 m (upper right panel) and velocity differences (bottom panel). Blue (red) dotted lines represent simulated (measured) data. The standard Gaussian distribution is indicated by the solid lines.

Fig. 5.8 indicates that PDFs are predominantly Gaussian according to the Kolmogorov-Smirnov test (not shown) with only slight differences in the values of skewness (S) and kurtosis (K) with respect to the Gaussian values ($S = 0$ and $K = 3$) (see Table 5.4). In addition, these figures show that FINO1 PDFs have more open tails than the LES values suggesting higher extreme values present in FINO1 data. This discrepancy may be partly attributed to the sub-grid scheme used as pointed out in (MJiménez and Cuxart 2006). Moreover, FINO1 data could be influenced by large-scale eddy motion (i.e. associated with large perturbations from the mean) which might influence the shape of

pdfs (Chu et al. 1996). Very similar behaviour is found at both heights studied since a similar flow structure is expected at these heights in the regime analyzed.

The PDF of the ΔU distribution displays very similar attributes, but is 'shifted' to the right (positive skewness) due to wind shear between both heights.

For further comparison with the Gaussian distribution, the skewness ($S = (x - \bar{x})^3 / \sigma_x^3$) and the kurtosis ($K = (x - \bar{x})^4 / \sigma_x^4$) factors for the PDF are summarized in the following table:

	<i>Skewness</i>	<i>Kurtosis</i>
$U'_{FINO140}$	-0.10	2.93
U'_{LES40}	-0.01	2.97
$U'_{FINO180}$	-0.09	3.03
U'_{LES80}	0.10	2.94
ΔU_{FINO1}	0.19	2.93
ΔU_{LES}	0.28	3.54

Table 5.4: Summary of Skewness and Kurtosis factors from the PDFs shown in Fig. 5.8.

5.3.3 Integral Scales of the Horizontal Wind Velocity

The integral scales are important in characterizing the structure of turbulence and are divided into the integral time scale (T_x) and integral length scale (L_x). They represent the average period and the average size of large eddies in unsteady flows, respectively.

5.3.3.1 Methodology

The time-scale can be estimated using the **autocorrelation function**. The temporal autocorrelation function, $R_x(\tau)$, for the fluctuating horizontal wind velocity is defined as:

$$R_x(\tau) = \frac{\overline{x_i(t)x_i(t+\tau)}}{\sqrt{\overline{x_i^2(t)}\sqrt{\overline{x_{i+\tau}^2(t)}}} = \frac{\overline{x_i(t)x_i(t+\tau)}}{\overline{x_i^2}} \quad (5.16)$$

where τ denotes the time lag between an original, $x_i(t)$, and a time shifted signal, $x_i(t+\tau)$. Therefore, autocorrelation quantifies the amount of common variation between an original variable ($x_i(t)$) sampled at time t and the same variable sampled at a later time $t+\tau$. The denominator of Eq. 5.16

normalizes the autocorrelation function so that if the two signals are perfectly correlated, the autocorrelation takes a value of ± 1 , and if the two signals are perfectly uncorrelated, then the autocorrelation will be equal to 0. An estimate of the large-eddy time-scale is provided from the autocorrelation function by the integral time scale, denoted T_x and defined only for positive τ as:

$$T_x = \int_0^{\infty} R_x(\tau) d\tau \quad (5.17)$$

The integral length-scale, L_x , can be estimated from the integral time-scale by using Taylor's frozen turbulence hypothesis (Taylor 1935), so integral length-scale (L_x) will be related to integral time-scale (T_x) by the mean flow velocity as:

$$L_x = T_x \bar{U} \quad (5.18)$$

So, the time-scale multiplied by the mean wind speed gives the average length scale of large eddies. This hypothesis only holds if the square turbulence intensity is small (Chu et al. 1996); that is, $I_U^2 = (\sigma_U/\bar{U})^2$ where \bar{U} is the mean velocity and σ_U its standard deviation, does not exceed 0.1. Then the substitution $dt = -dl/\bar{U}$ is a good approximation. For both series used in this study this condition holds.

5.3.3.2 Results

The temporal autocorrelation functions of the horizontal wind velocity fluctuations computed for the LES simulation (blue line) and FINO1 measurements (red line) are depicted in Fig. 5.9. Both graphs present similar decays to the first zero crossing, after which they become negative and proceed to oscillate about zero.

The area under these curves gives the average value of the time-scale of the eddies being carried past the measurement point (Eq. 5.17). There are different ways to calculate the integral scale as pointed out in O'Neill et al. (1994). In this study, the procedure used to estimate the time-scale is given by the time-average of the shifted product of the autocorrelation coefficients up to the first zero-crossing of the autocorrelation function (Kaimal and Finnigan 1994). The length-scales obtained are presented in the following table:

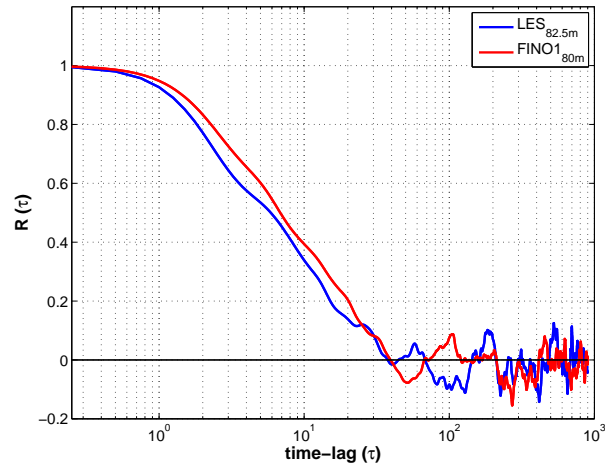


Figure 5.9: Autocorrelation function for the horizontal wind velocity fluctuations: LES simulation and FINO1 data.

Data	<i>time – scale[s]</i>	<i>length – scale[m]</i>
FINO1	10.8	101.5
LES	9.3	97.8

Table 5.5: Integral scales: LES simulation and FINO1 measurements

It is expected that the effect on integral time length of increasing the lag time would be to increase the integral time up to a limit where further increasing the lag time has little or no effect, at which point the integral time scale is considered to be accurate.

The integral time-scale values presented in Table 5.5 correspond to a time lag (τ) which has no further effect on the calculation for further increases.

5.4 Short-term Extreme Wind Events: Wind Gusts

In this section, a brief investigation of the ability of LES data to resolve short-term extreme wind events (wind gusts) is carried out.

5.4.1 Characterizing Gust Behaviour

In wind energy applications the atmospheric conditions are specified based on a 10 minute time series and TI. For fluctuations of wind speed on shorter time scales, a 'normal turbulence model' which assumes stationary spectral characteristics is considered as the basis for stochastic simulation of the inflow turbulence field. This synthetic turbulence wind field is then used for wind turbine design in order to predict wind turbine loads.

[Gontier et al. \(2007\)](#) carried out a comparison between different spectral models proposed in standards and found that any one of them reproduces well the extreme wind increments met in gusts.

While the tails of the PDFs for flow variables are influenced by large-scale eddy motion (i.e. associated with large perturbations from the mean), the tail of gradient PDFs are governed by short-lived eddy motion that departs significantly from the mean gradient ([Chu et al. 1996](#)). To achieve a more profound characterization of the gust, the statistics of velocity increments must be considered ([Peinke et al. 2004](#)) which are defined mathematically as follows,

$$U_{\tau}(t) := U(t + \tau) - U(t) \quad (5.19)$$

where $U_{\tau}(t)$ denotes the wind speed at time t and scale τ . It is evident from the definition of this quantity that it measures the fluctuations. Large values of U_{τ} and small times τ correspond to gusts. Based on this quantity U_{τ} and its statistics, we have analyzed whether LES simulations can provide this information by comparing both datasets. In Fig. 5.10, the probability density functions (PDFs) of the normalized U_{τ} for different τ values are shown along with the skewness (S) and the kurtosis (K) factors given in Table 5.6. The upper two curves in Fig. 5.10 have been shifted up one and two decades for clarity in the comparisons. As before, to accentuate the PDF tails, a log y-axis is used.

It is evident from the previous analysis that, for a more detailed mechanical load analysis, it seems that the LES model is able to generate an inflow time series which accounts for 'intermittent' flow.

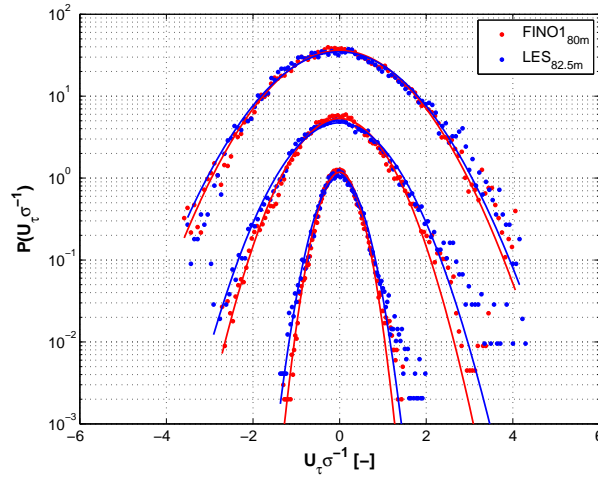


Figure 5.10: PDFs of velocity fluctuation increments at $\tau = 1, 3, 10$ sec respectively (bottom-up). Red (blue) filled circles denote measured (simulated) data. The standard Gaussian distribution is indicated by solid lines. PDFs are shifted vertically by an offset of 10.

	<i>Skewness</i>	<i>Kurtosis</i>
$FINO1_{U_{1sec}}$	0.23	3.48
$LES_{U_{1sec}}$	0.30	4.04
$FINO1_{U_{3sec}}$	0.21	3.53
$LES_{U_{3sec}}$	0.31	3.68
$FINO1_{U_{10sec}}$	0.16	3.12
$LES_{U_{10sec}}$	0.27	3.00

Table 5.6: Summary of Skewness and Kurtosis factors from the PDFs shown in Fig. 5.10.

5.4.2 Gust Factor

Gust factors measure the maximum expected deviation of the wind from its mean and is defined as:

$$K_p = \frac{U_{max}}{\bar{U}} \quad (5.20)$$

where K_p is the measured gust factor, U_{max} is peak wind speed, and \bar{U} is mean wind speed. The gust factor should be calculated over stationary records, thus the mean value of any segment should be equal to the mean value over the entire length of the record.

The gust factors as a function of duration time (1 sec, 3 sec and 10 sec) for several fixed averaging times (1 min, 2 min, 5 min, 10 min and 15 min) are presented in Fig. 5.11 for both data sets. The duration is the length of the time segment over which the peak value is being selected, that is, the duration of one segment used to collect a single sample peak.

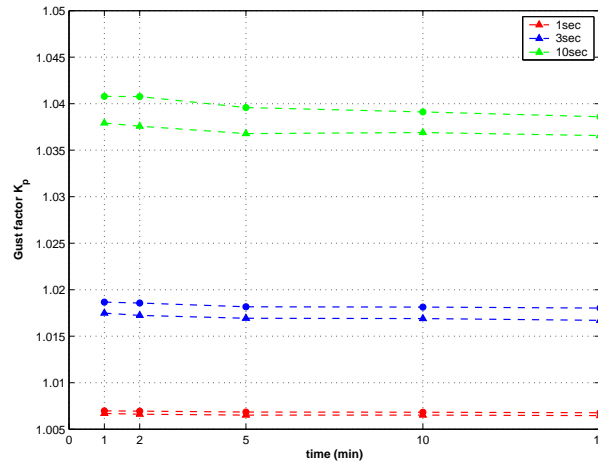


Figure 5.11: Gust factors as a function of duration time for several fixed averaging times: LES simulation (triangles) and FINO1 measurements (circles).

Typically, the calculated gust factor will increase with decreasing averaging time and increasing duration time, respectively, as can be seen in Fig. 5.11. The functional dependency is not very strong but model and observation are in good agreement

5.4.3 IEC Gust Shape

Extreme events are mentioned explicitly in IEC61400-1 (2005) and GL Offshore Guidelines (2005) as extreme load conditions which must be considered as ultimate load cases when designing a wind turbine. Within the framework of the IEC standard, these load situations are defined in terms of two independent site variables - a reference mean wind speed and a characteristic turbulence intensity. However, the gust events described in the IEC (IEC61400-1 2005) are formulated in terms of a coherent gust inherently deterministic in character, whereas the gusts experienced in real situations are of a stochastic nature with a limited spatial extension.

5.4.3.1 Deterministic Gust Model

The IEC deterministic gust model (IEC61400-1 2005) used for calculation of extreme gust during operation (EOG) is defined as:

$$V(z, t) = \begin{cases} V(z) - 0.37 \cdot V_{gustN} \cdot \sin\left(\frac{3\pi t}{T}\right) \cdot \left(1 - \cos\left(\frac{2\pi t}{T}\right)\right) & \text{for } 0 \leq t \leq T \\ V(z) = \bar{V}_{hub} \cdot \left(\frac{z}{z_{hub}}\right) & \text{otherwise} \end{cases} \quad (5.21)$$

$V(z)$ denotes the average wind speed as a function of height z above the ground. An assumed wind profile is used in the IEC standard to define the average vertical wind shear across the rotor swept area.

The gust speed V_{gustN} is defined (Eq. 5.22) in terms of the standard deviation of the horizontal wind turbulence.

$$V_{gust} = \text{Min} \left\{ 1.35(V_{e1} - V_{hub}); 3.3 \left(\frac{\sigma_1}{1 + 0.1 \left(\frac{D}{\Lambda_1} \right)} \right) \right\} \quad (5.22)$$

where Λ_1 is the prescribed turbulence scale parameter ($\Lambda_1 = 42m$ for $z_{hub} \geq 60m$), D is the rotor diameter and σ_1 is the standard deviation defined in the standard as:

$$\sigma_1 = I_{15} \left(\frac{15m/s + aV_{hub}}{a + 1} \right) \quad (5.23)$$

where $a=0.14$.

One of the main purposes of the IEC gust is to determine the response of the wind turbine controller to a fast rising gust. The duration of the gust, T , is specified as $10.5 s$ for 1 year and $14 s$ for 50 year return period.

The given IEC gust shape as well as the amplitude is basically arbitrary and is plotted for different turbulence intensities, 25 m/s mean wind speed and one year return period in the following figure:

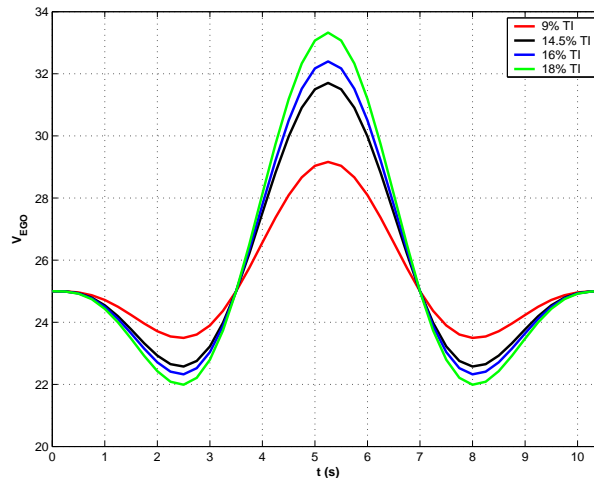


Figure 5.12: 'Mexican-hat-like' shape IEC gust for different turbulence intensities, 25 m/s mean wind speed and one year return period.

The procedure for identifying the individual EOG gust shape in LES simulations as well as in FINO1 measurements is made by correlating a moving 'window' of the same time length as the gust type considered (in this case an EOG gust with 10.5 s duration) along one hour time series. The gust is then selected when a high correlation is found between the series and the window, taking into account that if the correlation coefficients are similar during the half length of the window, they are not selected as a different gust since they are supposed to belong to the same gust.

Segments of the series with correlation coefficients higher than 85% are plotted in Fig. 5.13.

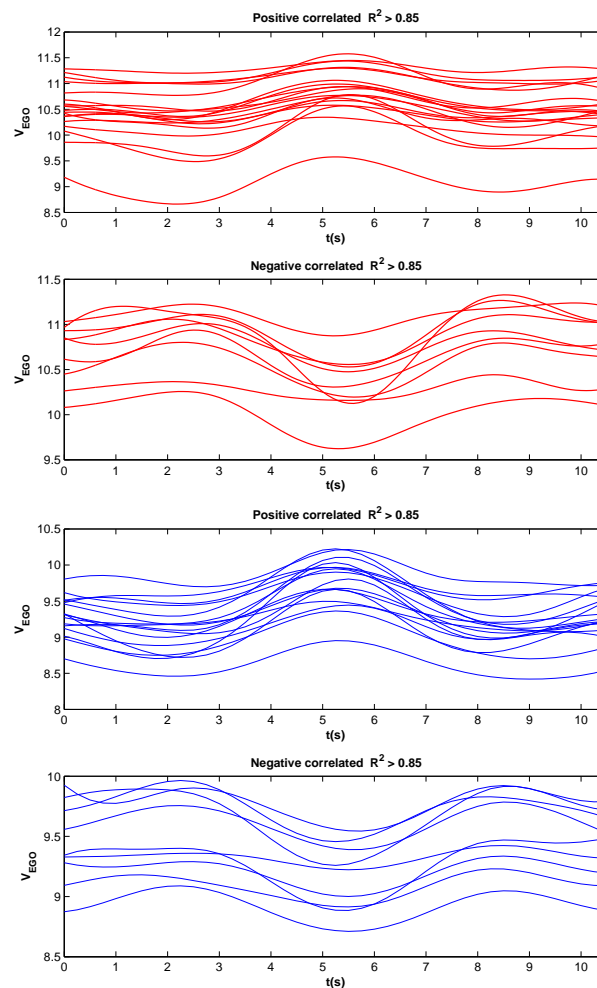


Figure 5.13: 'Mexican-hat-like' shape IEC gust found in the data: LES simulation (blue lines) and FINO1 measurements (red lines).

As can be seen in Fig. 5.13, the amplitude of the gusts is quite small compared with the IEC gust shape but it should be observed that a one hour time series is not enough and a longer one is required to obtain a larger amplitude gust, because the probability of occurrence of such gusts is small.

In Table 5.7, the number of gusts with a 'Mexican-hat-like' shape found in measurements and simulations is summarized for different correlation coefficients (- sign indicates negative correlation and + sign positive correlation)

R^2	0.85	0.90	0.95	0.99
FINO1	28 (9(-) 19(+))	10 (5(-) 5(+))	1 (-)	null
LES	25 (9(-) 16(+))	9 (4(-) 7(+))	2 (-)	null

Table 5.7: *Number of gusts with a 'Mexican-hat-like' shape*

Note that this study only gives a first idea about turbulent gusts but it is not possible to draw any conclusions since we have only used a one hour time series.

5.5 Summary

In this Chapter, the LES model performance has been tested over a number of stability regimes from neutral to moderately stable and for different geostrophic winds. The mean profiles of several parameters of great importance to wind energy applications have been compared. Moreover, in order to get a deeper understanding of the LES approach, a statistical analysis is performed by selecting a representative neutral case.

From the results obtained in this chapter, the following can be summarized:

- Comparison of numerical simulations with physical experiments is an essential test for assessing the performance of a model, however there are no standardized criteria to guide the validation.
- Only a qualitative comparison should be considered since model conditions are simpler than observed ones and only few forces are applied (the geostrophic wind, surface roughness and surface heat flux).
- The major differences between both data are presented in the most stable case. Nevertheless, most of the results fall within the error bars.
- Due to the unavoidable inherent uncertainties present in both sets of data, it is difficult to interpret the differences found. Nonetheless, in general good agreement is found between both datasets.
- The model output may be used to analyze different aspects of offshore winds in detail, which is not possible with existing observations.

Chapter 6

LES Application: Assessing the Power Density Error when Using Data from One Point at Hub Height as Representative of the Whole WT Rotor Area

6.1 Introduction

In wind energy applications, when conducting annual yield estimations or power curve measurements at a potential wind farm site, the accuracy of the assessment is critical to the profit of a project. Currently, the standard procedure for power curve measurements is given by the ([IEC61400-12 1998](#)) standard, where the wind speed at hub height is considered to be representative of the wind over the whole turbine rotor area. This assumption was good enough for small wind turbines. But for modern multi-MW wind turbines, that assumption is questionable and leads to considerable inaccuracies in wind power estimation. Wind varies temporally and spatially in the surface layer, therefore it is expected that the wind inflow will be non-uniform and unsteady over the rotor area. Moreover, the effect of this is amplified by the cubic relationship of available wind power with wind speed, which means that small differences in the wind speed causes big differences in wind power.

Several studies concerning this issue have been reported in the literature in the last years (Antoniou et al. 2007; Stefanatos et al. 2008; Walls and LaWhite 2009). For instance, Antoniou et al. (2007) used a wind profile from a wind mast and showed that the power performance measurements using a vertically resolved value of the wind over the rotor span is more accurate than the one using only the hub-height wind speed.

However all these studies account only for the shear variation along the rotor disk, where the influence of spatial and temporal variations of the wind due to turbulence are to some extent neglected. Therefore, in this study and for the first time, LES simulations which provide unprecedented temporal and spatial high resolution information across the turbine rotor span are used so as to offer an alternative choice to investigate variations in wind power for different rotor diameters and hub heights.

In the present Chapter, we investigate the relative percentage error when using the one-point measurement approach as representative of the whole rotor area for different combinations of rotor size, hub height and wind speed. To do so, we make use of the LES simulations performed in Chapter 4 under neutral and stable ($\overline{w\theta_s} = -0.1 \text{ mKs}^{-1}$) stratification boundary conditions for all simulated cases of geostrophic wind. To qualitatively assess the relative percentage error, an equivalent wind accounting for the spatial variation of the wind speed is defined and the difference of wind power between both approaches (error) is fitted to a normal distribution. Values of mean and variance of the Gaussian fit are given for all the cases investigated.

This Chapter starts in Section 6.2 with a short introduction on how the wind power density is affected by turbulent effects. Next, the methodology used is presented in Section 6.3. In Section 6.4 a method for describing the error is outlined and the chapter continues with results in Section 6.5. Finally, the Chapter finishes with a summary in Section 6.6.

6.2 Theoretical background

6.2.1 Power extracted from the wind

Wind turbines convert the kinetic energy content in the wind into electrical energy. The mechanical power, P , extracted from a wind turbine is given by the well-known expression:

$$P = \frac{1}{2}\rho AC_p U^3 = C_p \left(\frac{1}{2}\rho AU^3\right) = C_p P_{wind}, \quad (6.1)$$

where ρ is air density, A is the rotor 'swept area', U is the horizontal wind speed (Burton et al. 2001) and C_p is the aerodynamic efficiency or turbine's power coefficient defined by the ratio of turbine extracted power to wind power:

$$C_p = \frac{P}{P_{wind}} \quad (6.2)$$

This equation gives the theoretical expected power output for a given constant wind speed when turbulence effects are ignored.

6.2.2 Turbulence effects

Turbulent wind fluctuations are not only responsible for high mechanical loads (fatigue) on wind turbine components, which are important in the aerodynamic design, but also for variations in output power, which contribute to the expected power output value.

In order to reduce the uncertainties in the power calculation, turbulence effects must be taken into account not only in the temporal domain but also in the spatial domain. A graphical representation of the turbulence field is shown in Fig. 6.1. As the wind turbine blade sweeps around the 'rotor disk', areas of higher and lower wind speed are clearly distinguishable as the time evolves.

As the size of the rotor increases in relation to the typical sizes of turbulent eddies, the importance of wind speed variations across the rotor becomes greater.

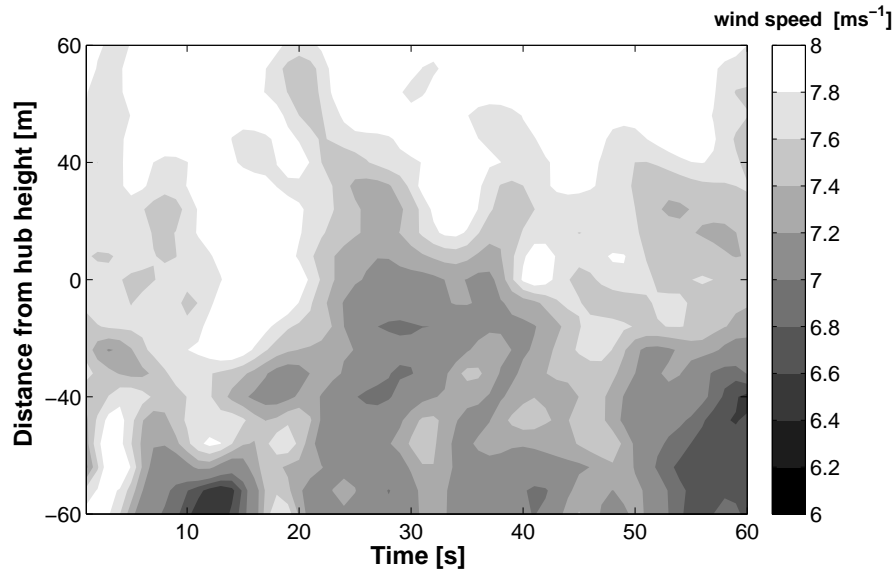


Figure 6.1: Wind field evolution over the rotor plane for a 120 m diameter wind turbine at 90 m hub height.

6.2.2.1 Temporal fluctuations

Here, we show in the temporal domain the influence of the turbulent wind fluctuation on the mean wind power production. By using the so-called Reynolds's decomposition the variation of the wind $u(t)$ can be divided into a mean part, \bar{U} , and a random fluctuating part, $u'(t)$,

$$u(t) = \bar{U} + u'(t) \quad (6.3)$$

Replacing $u(t)$ with U in Eq. 6.1 and assuming the air density constant, the expected wind power production for a wind turbine,

$$\overline{P(u(t))} \propto \overline{(\bar{U} + u'(t))^3} \quad (6.4)$$

becomes proportional to the average value of the third power of the actual wind speed. Therefore,

$$\overline{u(t)^3} = \overline{(\bar{U} + u'(t))^3} = \overline{\bar{U}^3 + 3\bar{U}^2 u'(t) + 3\bar{U} u'(t)^2 + u'(t)^3} \quad (6.5)$$

where the wind fluctuations ($u'(t)$) are assumed symmetrical about \bar{U} and therefore the mean value of $u'(t)$ is zero and hence this simplifies to:

$$\overline{u(t)^3} = \overline{U^3} + 3\overline{U}u'(t)^2 + \overline{u'(t)^3} \quad (6.6)$$

By definition, the mean square fluctuation about the mean is just the variance, σ^2 , and so the previous equation can be written as:

$$\overline{u(t)^3} = \overline{U^3} + 3\sigma^2\overline{U} + \overline{u'(t)^3}. \quad (6.7)$$

Using the definition of turbulence intensity ($TI = \sigma/\overline{U}$), this can be written as:

$$\overline{u(t)^3} = \overline{U^3}(1 + 3TI^2) + \overline{u'(t)^3}. \quad (6.8)$$

Therefore this reduces to:

$$\overline{P(u(t))} \propto \overline{U^3}(1 + 3TI^2) + \overline{u'(t)^3}. \quad (6.9)$$

Thus, the average power is determined by the third order mean value ($\overline{U^3}$) with a correction factor ($3TI^2$) plus the contribution of a higher order nonlinear term ($\overline{u'(t)^3}$) of the wind. Eq. 6.9 shows, for example, that in the special case of laminar wind flows (i.e. zero turbulent intensity, $TI = 0$) the expected power would simply be proportional to the steady $\overline{U^3}$ value, as shown above in Eq. 6.1, while that for the case of turbulent winds would not.

6.2.2.2 Spatial fluctuations

Another aspect is that the output power behaviour is also affected by non-uniform spatial wind fluctuations within the wind turbine rotor swept area, while wind measurements are only done at hub height. Especially for large rotor diameters, the variance of the wind speed becomes higher and therefore more uncertainties are expected.

The same technique of decomposition can be applied to a turbulent flow over space at a fixed time, $r(x_i)$, although here it is omitted for brevity.

These variations are obvious in Fig. 6.2 where the PDF of the wind speed differences between two points along the horizontal (left) and vertical (right) directions are plotted as a function of the the

distance between both positions (see figure legend). As expected, as the distance increases the wind variation increases.

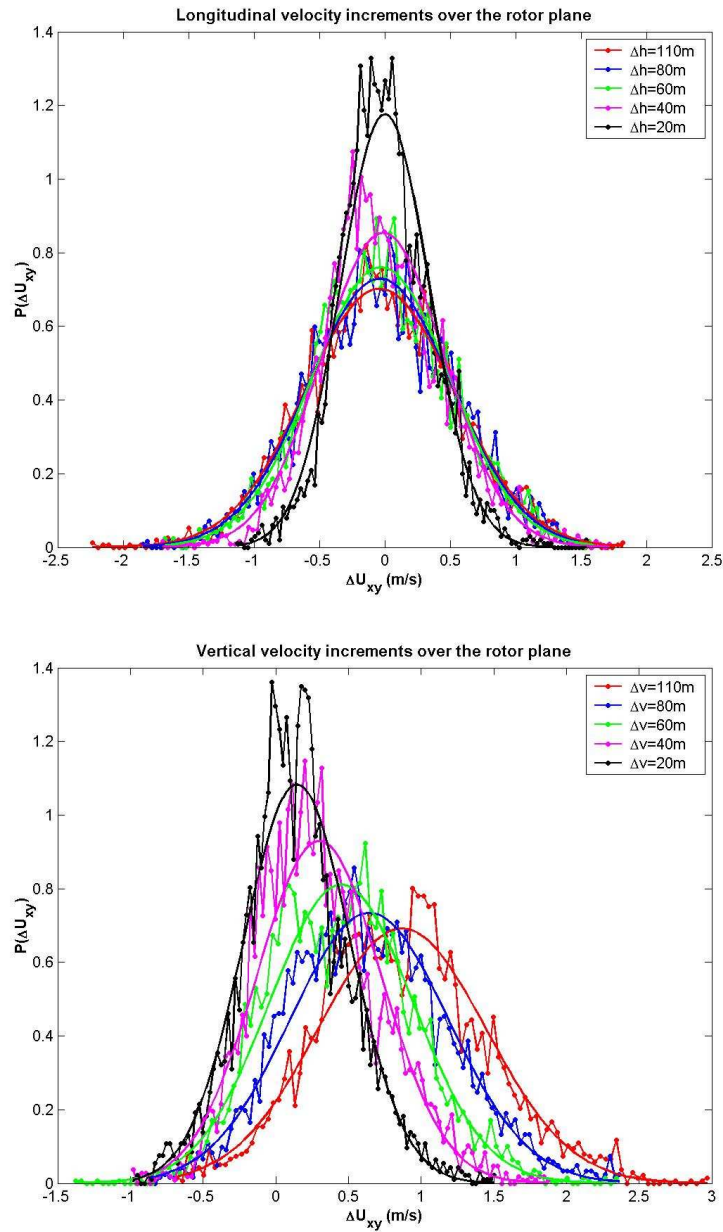


Figure 6.2: Example of longitudinal (upper panel) and vertical (bottom panel) PDF wind speed increments over the rotor plane (120 m diameter and 90 m hub height) for $u_g = 10 \text{ ms}^{-1}$.

Moreover for the vertical differences, in the PDFs figures the mean values are shifted further from 0 ms^{-1} as the distance between two heights increases, which can be attributed to the wind shear.

6.3 Methodology

One of the benefits of LES simulations lies in their ability to provide three-dimensional (y, z, t) arrays of instantaneous streamwise (u_i) and spanwise (v_i) velocity stationary fields encompassing the whole rotor plane, as depicted schematically in Figure 6.3 (left-side panel). Temporal and spatial resolutions are 5 m and 1 Hz respectively. Note that the temporal resolution of the simulations carried out in the previous Chapter is higher than 1 Hz, however for this study only data every 1 sec are used. The length of the time series is one hour.

From these time series of vertical YZ-cross-sections, the horizontal wind speed $U_i = (u_i^2 + v_i^2)^{\frac{1}{2}}$ is calculated where only data encompassing the swept rotor area (red circle in Fig. 6.3 (right-side panel)) and at the hub height selected are extracted for further study. Then, for instance, for a wind turbine of 120 m rotor diameter, horizontal wind speed ($U_i(y, z, t)$) information on 437 squares of $5 \times 5 \text{ m}^2$ are provided for each time step.

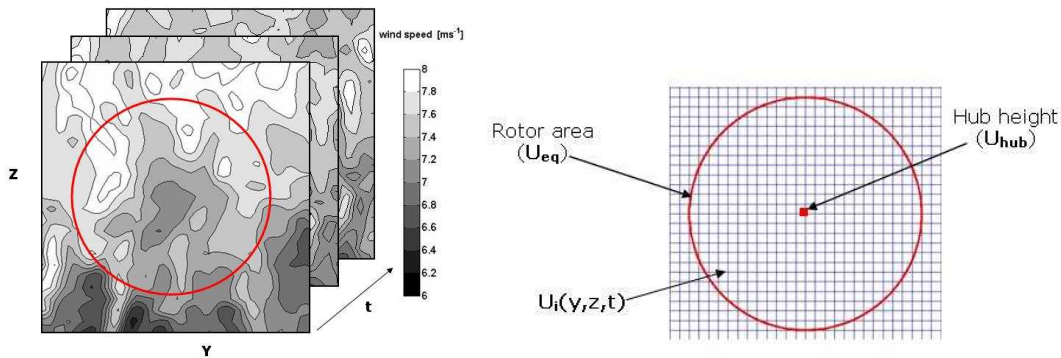


Figure 6.3: Schematic visualization of a 3D velocity field provided by the LES model (left panel). Swept rotor area divided into grids (5 m resolution) (right panel).

As mentioned previously, the main goal of this study is to assess the error committed when a single point at hub height is used as representative of the whole rotor area. For this purpose, a time series at hub height and a time series weighting the rotor plane information are needed for each rotor size, hub height and geostrophic wind investigated. These time series are obtained from the vertical cross-sectional time series of horizontal wind speed where the following two approaches of wind power density are compared,

- Standard approach: extracting the wind speed at one point located at the hub height position ($U_{hub}(t)$),

- Rotor area-weighted approach: a equivalent wind speed is calculated as,

$$U_{eq}(t) = \sqrt[3]{\frac{1}{A} \left(\sum_i u_{i,t}^3 \cdot A_i \right)} \quad (6.10)$$

where i denotes the specific value at the grid point over the rotor plane at position (y,z) , A_i is the square area (in this case, $5 \times 5 \text{ m}^2$) and A is the rotor planar area.

By using Eq. 6.10, the spatial variation of wind speed over the rotor plane is accounted for.

Next, the wind power density ($\frac{P}{AC_{pp}}$) is obtained for each time step by using Eq. 6.1 (denoted as P_{hub} and P_{eq}). In this analysis, it is assumed that all parameters in Eq. 6.1 remain constant except for the rotor radius ($A = \pi r^2$) and the wind speed.

Fig. 6.4 gives an example of the wind speed time series of (U_{hub}) and (U_{eq}) using the approaches mentioned before and for a wind turbine with 120 m rotor diameter and 90 m hub height.

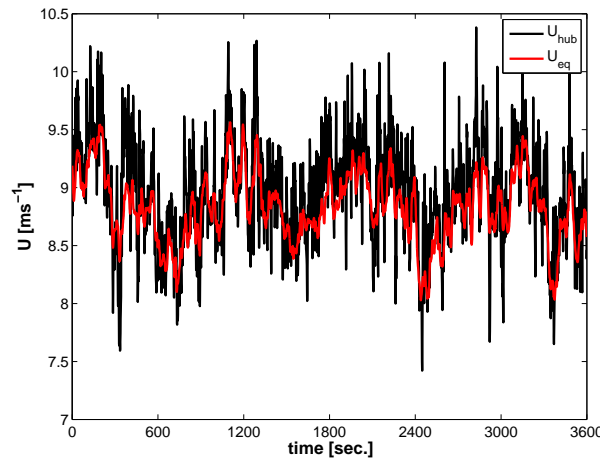


Figure 6.4: Example of time series of wind speed for one point located at hub height (90 m) (black line) and considering the whole rotor diameter (120 m) using Eq. 6.10 (red line).

As can be seen from the figure above, lower amplitude small-scale fluctuations are evident in the time series of U_{eq} compared to the U_{hub} time series. This can be attributed to spatial averaging, which in the temporal domain according to Taylor's hypothesis of 'frozen' turbulence ($t = \frac{D_{rotor}}{U_{eq}}$) would correspond to applying a running average filter of approximately 11.5 sec window width (for this case). Therefore, its effect will account for the error variance of the wind power density.

Moreover, in order to have further information about the vertical mean condition (one hour averaged) of the flows involved in this study, Fig. 6.5 shows the mean profiles of neutral (solid lines) and stable (for the case $w\theta_s = -0.1 \text{ mKs}^{-1}$) (dashed lines) as the geostrophic wind (u_g) varies.

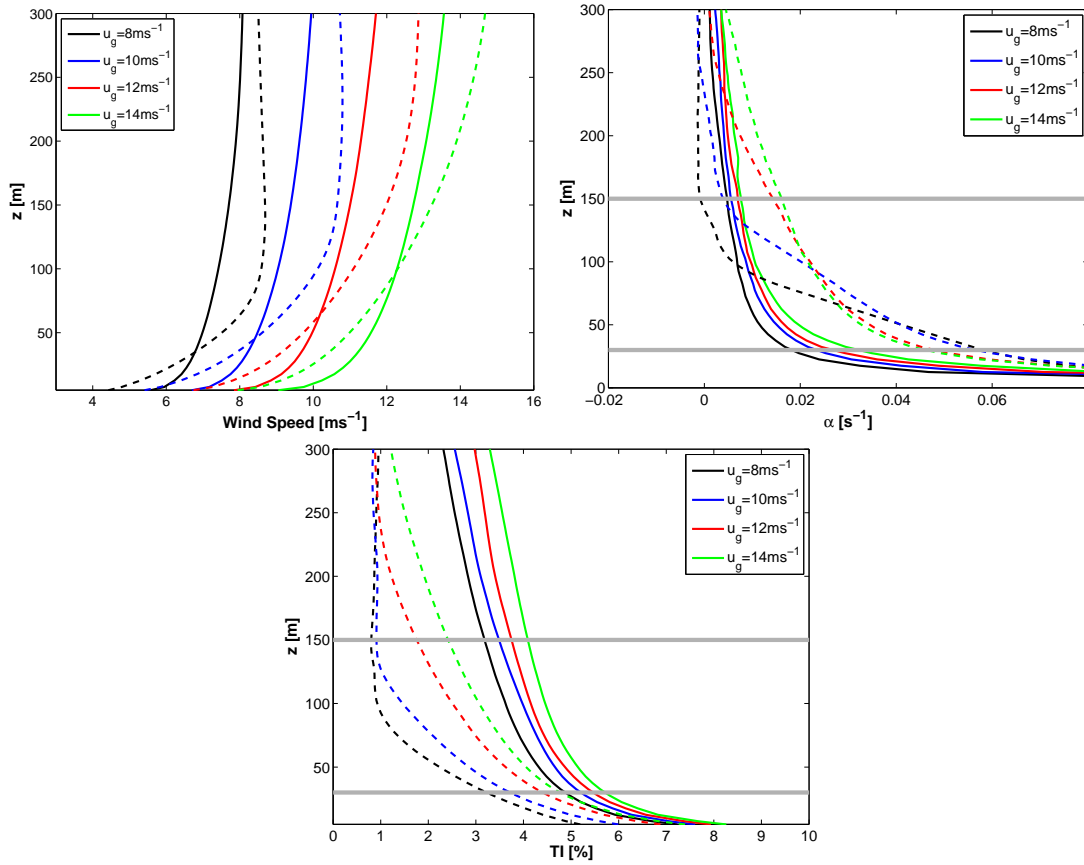


Figure 6.5: Wind speed, vertical wind shear (α) (upper panel) and Turbulence Intensity (TI) (lower panel) profiles for each case investigated. Solid (dashed) lines represent neutral (stable) regime.

For the analytical definition of α and TI , refer to Chapter 5.

Note that the simulation of stable regime for $u_g = 8 \text{ ms}^{-1}$ is suspicious of runaway cooling (see Chapter 4) and has to be considered with caution, although here it has been used for further calculations.

6.4 Assessment of Error

Before assessing the error committed by assuming that the wind speed at hub height is uniform over the rotor in terms of statistical measures, it is important to analyze how the error is distributed. In particular, the question of whether the error follows a Gaussian distribution has to be carefully tested. Here, the error is understood as the difference between both approaches. Let $P_{hub}(t)$ be the wind power at hub height and $P_{eq}(t)$ the wind power equivalent (as calculated with Eq. 6.10); then the relative deviation between the two wind power density values at time t is given by:

$$\varepsilon_{rel}(t) = \left(\frac{P_{eq}(t) - P_{hub}(t)}{P_{hub}(t)} \right) \times 100. \quad (6.11)$$

This definition of relative percentage error gives us the basic element for an assessment of error in this study.

The error, defined as a difference, is expected to follow a Normal or Gaussian distribution defined by:

$$f(x) = \frac{1}{\sqrt{2\pi\sigma^2}} e^{-\frac{(x-\mu)^2}{2\sigma^2}} \quad (6.12)$$

where μ represents the mean and σ^2 the variance. As pointed out in (Lange and Focken 2005), it is very helpful to know the type of error distribution to interpret the standard deviations of these distributions in terms of confidence intervals.

Then, the PDF (ε_{rel}), for each case studied, is calculated by dividing the relative differences between both approaches (ε_{rel}) into bins of 0.05 width and counting the relative frequency within the bins as shown graphically in Fig. 6.6.

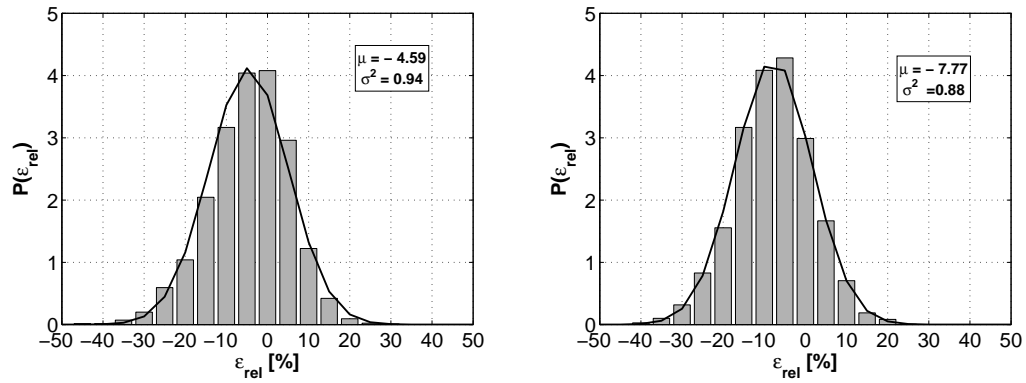


Figure 6.6: Example of PDFs of the relative percentage error for a 100 m diameter wind turbine with 90 m hub height wind, for neutral (left panel) and stable (right panel) regimes. The solid line represents the fit to a Gaussian distribution.

6.5 Results

In this section, the relative percentage error (ε_{rel}) is calculated for different combinations of rotor diameters and hub heights and for the four levels of geostrophic wind simulated. Tables 6.1 and 6.2 give, for each case investigated, the values of the mean (μ) and variance (σ^2) obtained from the fit to a Gaussian distribution for neutral and stable regimes, respectively. The goodness of fit to the Gaussian distribution has been tested by using a Kolmogorov-Smirnov (K-S) test. No appreciable departure from a standardized Gaussian distribution is evident for any of the cases investigated and so the standard deviation ε_{rel} can be interpreted at 68% confidence intervals.

The negative sign in Tables 6.1 and 6.2 indicate that the assumption of one point at hub height as representative of the wind over the whole rotor disk leads to an over-estimation of the wind power with respect to the equivalent power density approach (P_{eq}).

In order to easily identify any trend in the mean error behaviour as a function of wind speed, hub height and rotor diameter, the values given in Tables 6.1 and 6.2 are plotted in Fig. 6.7 grouped in wind speed classes. Furthermore and as additional information to account for the spatial fluctuation of the wind, the averaged standard deviation of wind speed over the rotor plane ($\sigma_{u_{i,rotor}}$) is plotted in Fig. 6.8.

A visual inspection of these figures shows that errors are larger in the stable regime than in the neutral regime. This can mainly be attributed to the large variation of wind speed over the rotor disk which in fact is caused by the higher wind shear for this regime as confirmed by Fig. 6.5. This could

lead to an over-estimation of the power curve for instance when measurements are taken in a time period where most of the time the atmosphere is stably stratified.

Moreover and as expected, as the hub height increases, the error decreases for all geostrophic wind cases investigated since the turbulence decreases with height for both regimes.

From Fig. 6.8 it is clearly seen that as the rotor diameter and the geostrophic wind increases the wind variations over the rotor plane increases. On other hand, as the hub height increase the wind variations decrease as expected.

In the stable regime, it can be seen that, as the geostrophic wind increases, the mean error decreases. The reason for this effect could be due to the higher asymmetry of the incoming wind flow for lower geostrophic wind (as illustrated in Fig. 6.5).

Neutral regime					
Hub Height [m]	Diameter [m]	$u_g = 8 \text{ ms}^{-1}$	$u_g = 10 \text{ ms}^{-1}$	$u_g = 12 \text{ ms}^{-1}$	$u_g = 14 \text{ ms}^{-1}$
90	80	-3.54 (0.78)	-3.92 (0.78)	-4.27 (0.82)	-3.76 (0.91)
	100	-3.81 (0.90)	-4.21 (0.88)	-4.59 (0.94)	-4.22 (1.04)
	120	-4.18 (0.99)	-4.59 (0.97)	-4.94 (1.03)	-4.74 (1.13)
	140	-4.84 (1.08)	-5.30 (1.07)	-5.51 (1.14)	-5.60 (1.25)
	160	-5.90 (1.16)	-6.45 (1.16)	-6.57 (1.24)	-6.89 (1.35)
100	80	-3.05 (0.72)	-3.18 (0.70)	-3.74 (0.79)	-2.88 (0.81)
	100	-3.20 (0.82)	-3.42 (0.80)	-4.07 (0.93)	-3.20 (0.93)
	120	-3.42 (0.89)	-3.75 (0.88)	-4.34 (1.02)	-3.56 (1.02)
	140	-3.80 (0.98)	-4.31 (0.97)	-4.72 (1.13)	-4.14 (1.12)
	160	-4.34 (1.05)	-4.99 (1.04)	-5.23 (1.22)	-4.86 (1.20)
110	80	-2.96 (0.67)	-2.72 (0.60)	-3.23 (0.75)	-2.48 (0.74)
	100	-3.09 (0.77)	-2.94 (0.69)	-3.51 (0.86)	-2.72 (0.85)
	120	-3.19 (0.85)	-3.26 (0.76)	-3.77 (0.94)	-2.98 (0.93)
	140	-3.43 (0.94)	-3.74 (0.83)	-4.06 (1.03)	-3.41 (1.01)
	160	-3.77 (1.01)	-4.27 (0.89)	-4.41 (1.11)	-3.94 (1.09)

Table 6.1: Mean (variance) relative percentage error [%] in power when varying the diameter and hub height in the neutral regime.

Stable regime					
Hub Height [m]	Diameter [m]	$u_g = 8 \text{ ms}^{-1}$	$u_g = 10 \text{ ms}^{-1}$	$u_g = 12 \text{ ms}^{-1}$	$u_g = 14 \text{ ms}^{-1}$
90	80	-9.26 (0.11)	-9.42 (0.32)	-6.93 (0.69)	-6.04 (0.95)
	100	-11.27 (0.12)	-10.24 (0.33)	-7.20 (0.77)	-6.32 (1.04)
	120	-13.06 (0.13)	-11.11 (0.34)	-7.56 (0.80)	-6.65 (1.11)
	140	-15.34 (0.14)	-12.33 (0.35)	-8.19 (0.83)	-7.19 (1.17)
	160	-17.57 (0.15)	-13.70 (0.36)	-9.09 (0.85)	-8.02 (1.21)
100	80	-6.52 (0.07)	-8.03 (0.23)	-7.05 (0.57)	-5.77 (0.75)
	100	-8.30 (0.08)	-8.96 (0.24)	-7.33 (0.63)	-5.94 (0.84)
	120	-9.99 (0.08)	-9.89 (0.25)	-7.66 (0.67)	-6.15 (0.90)
	140	-12.17 (0.09)	-11.15 (0.25)	-8.14 (0.69)	-6.48 (0.95)
	160	-14.30 (0.09)	-12.48 (0.26)	-8.75 (0.71)	-6.92 (0.99)
110	80	-4.27 (0.05)	-6.81 (0.19)	-6.03 (0.48)	-5.37 (0.65)
	100	-5.74 (0.06)	-7.83 (0.20)	-6.31 (0.54)	-5.49 (0.74)
	120	-7.21 (0.06)	-8.82 (0.21)	-6.63 (0.57)	-5.62 (0.80)
	140	-9.19 (0.06)	-10.11 (0.21)	-7.08 (0.59)	-5.84 (0.86)
	160	-11.16 (0.07)	-11.43 (0.22)	-7.57 (0.61)	-6.14 (0.89)

Table 6.2: Mean (variance) relative percentage error [%] in power when varying the diameter and hub height in the stable regime ($\overline{w\theta}_s = -0.01 \text{ mK s}^{-1}$). Values in bold are suspicious of runaway cooling (see Chapter 4).

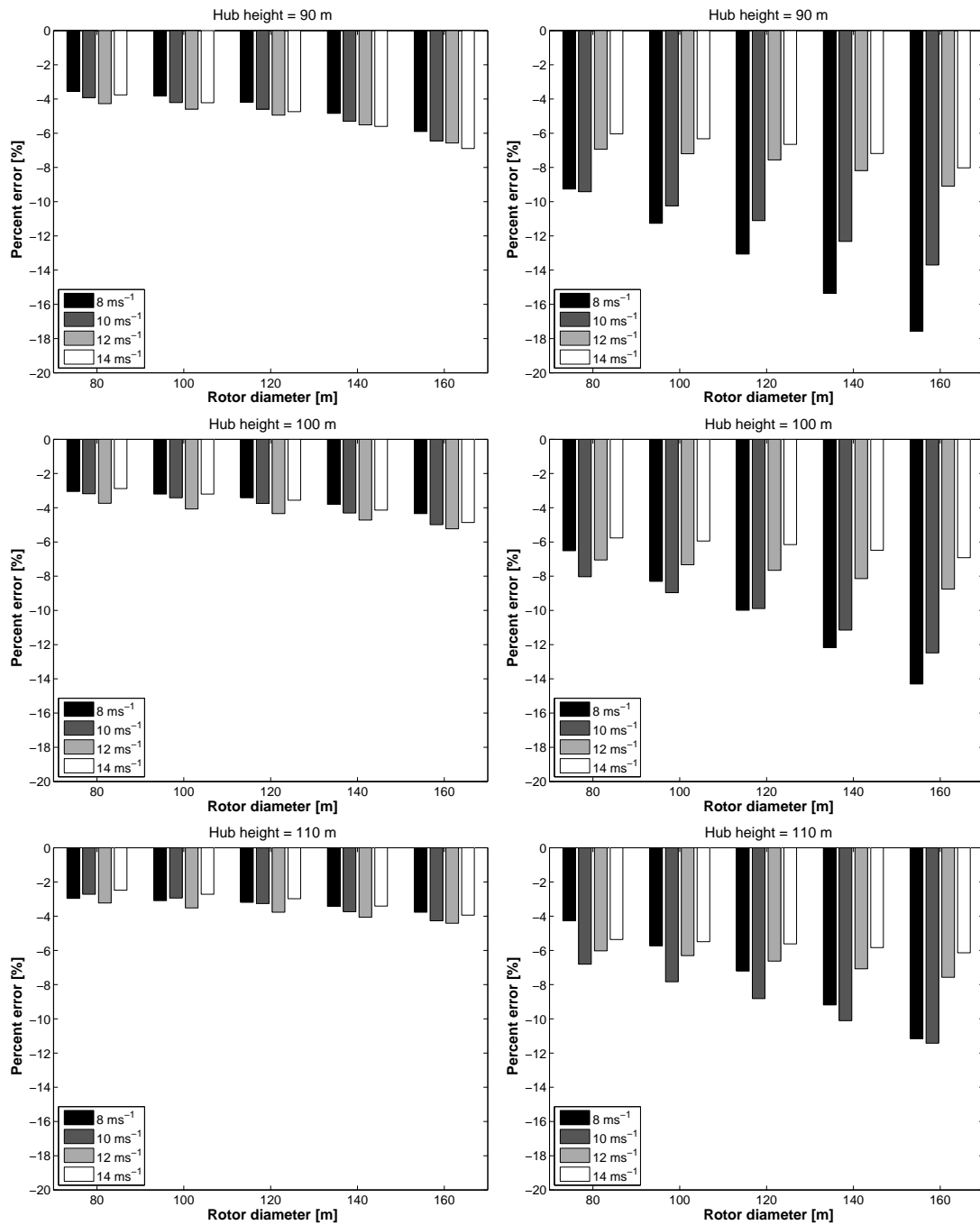


Figure 6.7: Percentage relative mean error [%] in power with varying rotor diameter at 90 m hub height (upper panel), at 100 m hub height (middle panel) and at 110 m hub height (lower panel). Left (right) side of the panel corresponds to neutral (stable) regime.

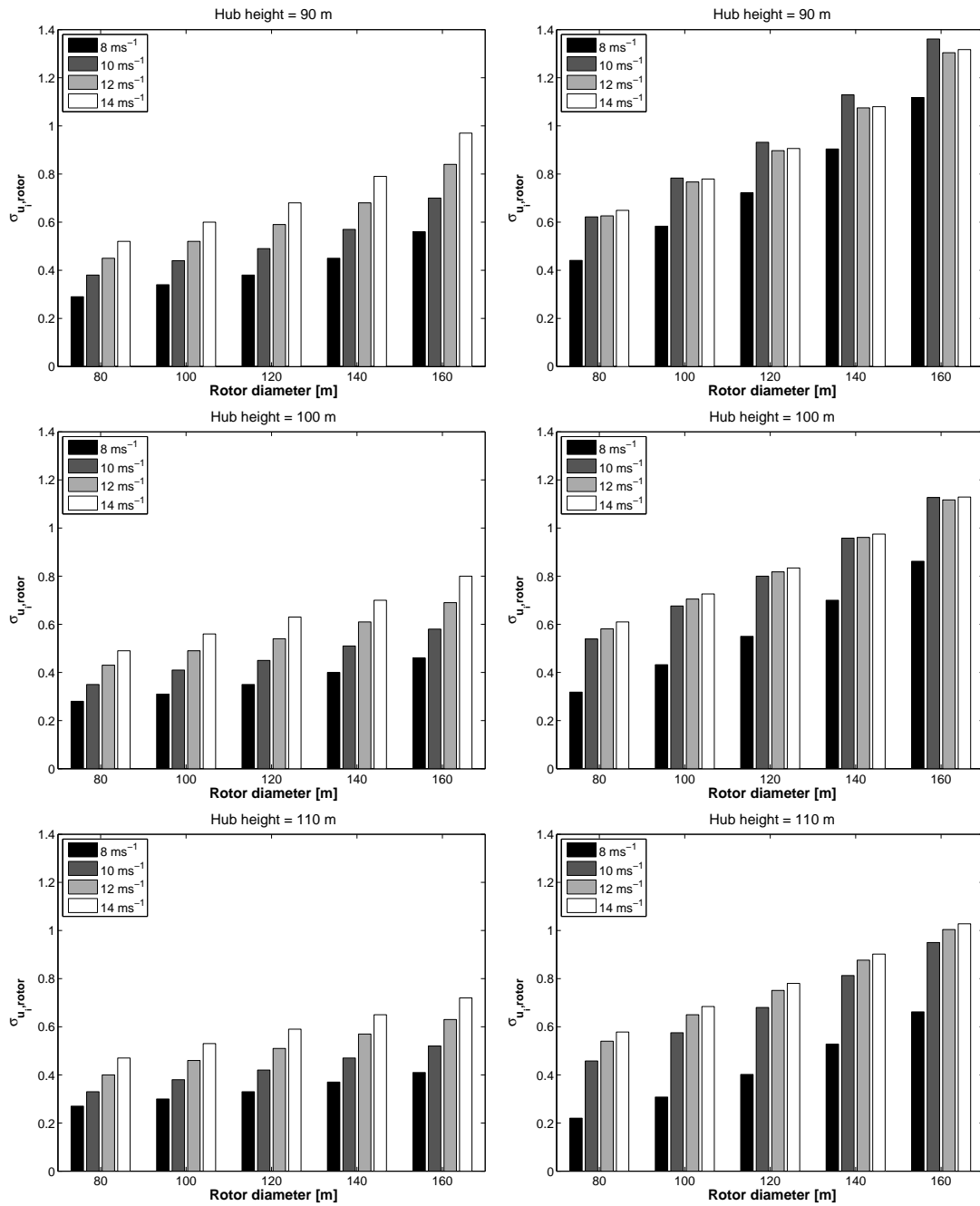


Figure 6.8: Average standard deviation of wind speed ($\overline{\sigma_{u_i}(y, z)}$) over rotor plane. As before, left (right) side of the panel corresponds to neutral (stable) regime.

6.6 Summary

The main objective of this Chapter was to investigate whether the hub height wind power density might not be representative of the integrated rotor plane power density for wind turbines of the size of offshore wind turbines.

To do so, the LES simulations performed in Chapter 4 in neutral and stable regimes and for all geostrophic wind cases simulated were used. The relevance of our approach is that it gives a more precise description of the wind inflow over the rotor span. To qualitatively assess the relative percentage error committed, an equivalent wind accounting for the spatial variation of the wind speed is defined and the difference of wind power between both approaches (error) is fitted to a normal distribution. Values of the mean and variance of the Gaussian fit are given for all cases investigated.

This study clearly shows how the assumption made in one-point measurements as representative of the whole rotor area leads to large errors in wind power density. The total mean errors are found to lie in the range 2–7 percent in the neutral regime and 4–15 percent in the stable regime.

As the hub height increases, the error decreases for all geostrophic wind cases investigated because the turbulence decreases with height in both regimes.

Chapter 7

Conclusions

In the course of the present Ph.D. Thesis an analysis of the Marine Atmospheric Boundary Layer (MABL) has been carried out by using field observations and LES-modeling, concentrating in particular on turbulence effects over the range where they play a role in wind energy applications. The motivation behind this study was to gain a better understanding of the MABL flows.

The first part of the work has been devoted to an observational data analysis where some characteristics of the surface MABL were studied in detail. For this purpose, a two-year data period from the offshore platform FINO1 located in the North Sea was used. An extensive quality control and data processing were presented, where the sonic anemometers available at FINO1 were used as primary data source. The so-called eddy covariance technique was used to determine the sensible heat fluxes and wind stresses. The Obukhov length was then derived and the stability parameter (zL^{-1}) calculated. It was found that at FINO1 the boundary layer is often neutral stratified. Besides, the Monin-Obukhov theory (MOST) was checked and was found to be in close agreement with FINO1 data, although for the most stable situations a big scatter in data was presented.

In addition, wave data from a Wave-Rider Buoy located close to FINO1 mast were used to investigate the sea state dependence on the surface wind stress under neutral conditions and thus to gain a better description of the surface MABL. The so-called wave age parameter ($C_p u_*^{-1}$) was derived and used to classify the sea state, namely, pure wind-sea and swell. It has been shown that data present a general trend of increasing sea roughness with inverse wave age, in agreement with previous studies. However, from this investigation it became clear that the dependence of sea roughness with the sea state is less pronounced than the ones reported in the literature, which implies that the wave age affect in the drag coefficient is quite small. This can probably be explained by differences

in data selection, mast location, data period as well as methods used to obtain the parameterization from data. It is worth mentioning that in this investigation the main difference to previous studies lies in the long period of data analysed. Future research must be considered to confirm this finding.

The second part of this project dealt with simulation of the MABL by using the Large Eddy Simulation (LES) technique. A parallelized LES model (PALM) was used to generate a LES-dataset where several idealized simulations were carried out with (i) different surface cooling (negative heat flux prescribed); and (ii) different geostrophic winds. Doing so, a big range of stabilities (from neutral to very stable MABL) were simulated. These simulations were intended to represent the MABL where the Charnock parameterization was used to account for roughness over the sea.

In general the model, which is based on a TKE-turbulence closure with Monin-Obukhov similarity theory (MOST) used for fluxes at the surface with stability corrections, was capable of predicting realistic turbulent wind fields, however for strong stable stratification unphysical profiles in both mean and turbulent quantities were presented. Moreover, these simulations suffered runaway cooling (very fast decreases of the surface temperature). That problem is a well-known limitation in modeling where such flow conditions are very difficult to simulate due to the intermittent nature (turbulent burstings in the midst of a laminar flow) of the turbulence.

Besides, the best configuration set-up (for the LES application considered) was chosen according to several sensibility tests carried out. It was turned out that a resolution of 5 m and domain size of about $2560 \times 1280 \times 1371$ is adequate from a numerical point of view to represent the essential features of the MABL for neutral and for stable conditions up to weak-moderate stable cases. To perform LES of most stable cases presented in this study a smaller resolution has to be used to reduce the influence of the SGS parameterization. Results were consistent with MABL features.

Furthermore, LES simulations were tested with FINO1 data through vertical profiles of wind shear, wind direction and turbulence intensity. To compare both datasets a similar strategy as used in ([Jimenez 2005](#)) was carried out. Here, the FINO1 database was classified in two categories according to the forcing applied in the simulation and then compared qualitatively with the profile simulated. This comparison was limited to the three sonic anemometers available at FINO1.

To further understand the LES approach, a statical analysis was performed through the selection of a representative neutral case from the FINO1 database. Horizontal wind spectra were analyzed in detail for different grid resolutions. Moreover, probability density function and autocorrelation as well as a brief investigation of the strength of LES data to solve short-term extreme wind events (wind

gust) was carried out. It has been shown that LES is a potential tool to tackle this issue, however further work is still needed in this respect.

In spite of the difficulties found to interpret the differences between both datasets ('idealized' simulation with observational data), a generally good qualitative agreement in many areas was found with some differences that could be attributed to the major part to the sensitivity to initial conditions, subgrid model parameterization and measurement uncertainties. It is encouraging for the physical understanding of the MABL that LES reproduces the same overall behavior as it is seen in the observations.

Finally, a basic study concerning the turbulence effect on wind power density was carried out. Here the relative percentage error committed when using a point measurement at hub height as representation of the whole rotor is investigated. This error was assessed quantitatively by defining an equivalent wind speed accounting for the spatial variation of the wind speed over the rotor span. It was found that the total mean errors are bigger for stable than for neutral conditions. That could lead to an overestimation of the power curve for instance when the measurements are taken in a time period where most of the time the atmosphere is stable stratified.

7.1 Future work

Based on the knowledge gained during the development of this work, the author suggests the following for future work:

7.1.1 Observational data

Concerning to observational data the line of investigation of 'sea state dependence on the surface wind stress' seems to be quite promising although much work is still left to do in this field. For instance, to check by using statistical methods the degree of self-correlation between friction velocity (u_*) and peak phase speed (C_p).

7.1.2 Simulation

It is proposed to extend this study to higher values of geostrophic wind as well as to unstable stratification.

Moreover, and following the wind energy application framework, the next studies are proposed:

LIDAR vs. LES volume average

In the last years the use of light detection averaging and ranging (LIDAR) technique in wind energy applications has become more and more important for measuring wind velocity and direction.

With LIDAR technique, the velocity is determined from the radial velocities measured in different directions (N, E, S and W) relative to the device (see Fig. 7.1). This means that LIDAR velocities are vector averages taken over a volume, which is different from the scalar averages acquired at one-point measured cup anemometers. This vector averaging could lead to a bias in the velocities obtained from LIDAR devices and therefore the relationship between volume and point measurements must be understood in order to increase the accuracy of the data (Clive 2009).

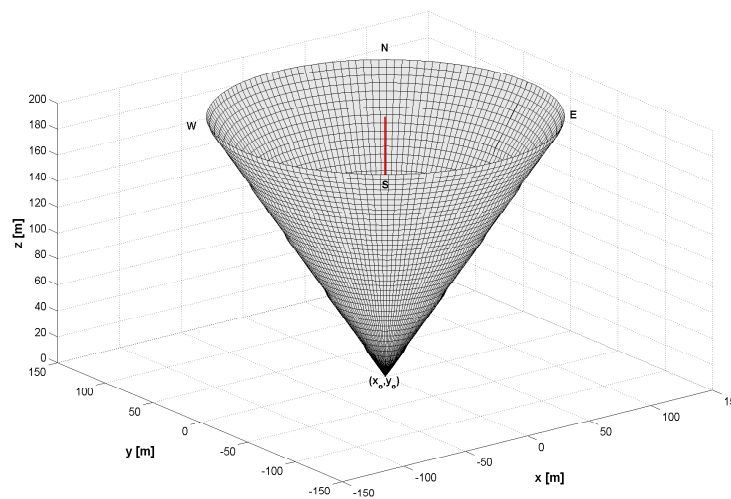


Figure 7.1: LIDAR scanning configuration where each square represents 5 m resolution LES data.

With 3D LES data this bias can be assessed, since it is possible to extract information of high resolution wind components content in the same cone scanned by the LIDAR and compare them with its value at the center point (red line in Fig. 7.1).

Wind turbine design:

In the standard guidelines for wind turbine design ([IEC61400-1 2005](#)) a 'normal turbulence model' is recommended which assumes stationary spectral representations that serve as the basis for a stochastic simulation of the inflow field. In this approach neither the unsteady character of the wind nor coherent structures are represented which are important factors in predicting wind turbine loads ([Kelley et al. 2005](#); [Sim et al. 2009](#)).

Therefore and in order to have a better description of the inflow field used in the standard aerolastic models, LES seems to be a promising tool. Time-dependent unsteady inflow velocities over the whole rotor span can be generated and used in an aerolastic model for turbine load simulations and turbine fatigue load analysis. Comparison between actual methods which generate synthetic flow and time dependent LES flow should be of great interest for the wind energy industry.

Bibliography

- E. Agee and A. Gluhovsky. Further aspects of large eddy simulation model statistics and inconsistencies with field data. *J. Atmosph. Sci.*, 56(16):2948–2950, 1999.
- A. Andr en. The structure of stably stratified atmospheric boundary layers: A large-eddy simulation study. *Q. J. Royal Meteorol. Soc.*, 121:961–985, 1995.
- A. Andr en, A. R. Brown, P. J. Mason, C-H. Moeng, F. T. M. Nieuwstadt, and U. Schumann. Large-eddy simulation of the neutrally stratified boundary layer: A comparison of four computer codes. *Q. J. Royal Meteorol. Soc.*, 120:1457–1484, 1994.
- I. Antoniou, R. Wagner, M. S. Pedersen, U. S. Paulsen, H. A. Madsen, H. E. J rgensen, K. Thomsen, P. Enevoldsen, and Thesbjerg L. Influence of the wind characteristics on the turbine performance. In *Proc. EWEC*, Milan, 2007.
- A. Arakawa and V. R. Lamb. *Methods of computational physics*. Academic Press, 1977.
- P. A. Arya. *Introduction to Micrometeorology*. Academic Press, 2001.
- S. Basu and F. Port -Agel. Large-eddy simulation of stably stratified atmospheric boundary layer turbulence: A scale-dependent dynamic modeling approach. *J. Atmosph. Sci.*, 63:2074–2091, 2006.
- R. J. Beare and M. K. Macvean. Resolution sensitivity and scaling of large-eddy simulations of the stable boundary layer. *Boundary-Layer Meteorology*, 112:257–281, 2004.
- R. J. Beare, M. K. Macvean, A. A. M. Holtslag, J. Cuxart, I. Esau, J-C. Golaz, M. A. Jimenez, M. Khairoutdinov, B. Kosovic, D. Lewellen, T. S. Lund, J. K. Lundquist, A. McCabe, A. F. Moene, Y. Noh, S. Raasch, and P. Sullivan. An intercomparison of large-eddy simulations of the stable boundary layer. *Boundary-Layer Meteorology*, 118:247–272, 2006.

- H. Bergström. Boundary-layer modelling for wind climate estimates. *Wind Energy*, 25:289–299, 2001.
- R. A. Brown. On the inflection point instability of a stratified ekman boundary layer. *J. Atmosph. Sci.*, 29(5):850–859, 1972.
- A. Brut, A. Butet, P. Durand, G. Caniaux, and S. Planton. Air-sea exchanges in the equatorial area from the equalant99 dataset: Bulk parametrizations of turbulent fluxes corrected for airflow distortion. *Quarterly Journal of the Royal Meteorological Society*, 131:2497–2538, 2005.
- G. Burba and D. Anderson. Introduction to the eddy covariance method: general guidelines and convectional workflow. Technical report, LICOR Biosciences, 2007.
- T. Burton, D. Sharpe, N. Jenkins, and E. Bossanyi. *Wind energy handbook*. Wiley InterScience, 2001.
- J. C. Butcher. *Numerical methods for ordinary differential equations*. John Wiley, 2003.
- P. Carlotti. Two-point properties of the atmospheric turbulence very close to the ground: Comparison of a high resolution les with theoretical models. *Boundary-Layer Meteorology*, 104(3):381–410, 2002.
- H. Charnock. Wind stress over a water surface. *Q. J. Royal Meteorol. Soc.*, 81:639–640, 1955.
- C. R. Chu, M. B. Parlange, G. Katul, and J. D. Albertson. Probability density functions of turbulent velocity and temperature in the atmospheric surface layer. *Water Resouces Res.*, 32(6):1681–1688, 1996.
- P. J. M. Clive. Compensation of bias in lidar wind resource assessment. *Wind engineering*, 32: 415–432, 2009.
- G. T. Csanady. *Air-Sea Interaction - Laws and Mechanisms*. Cambridge Univeristy Press, 2001.
- J. W. Deardorff. Theoretical expression for the countergradient vertical heat flux. *J. Geophys. Res.*, 77:5900–5904, 1972.
- J. W. Deardorff. *Workshop on Micrometeorology*, chapter Three-dimensional numerical modeling of the planetary boundary layer, pages 271–311. D. A. Haugen, Amer. Meteorol. Soc., Boston, 1973.
- J. W. Deardorff. Stratocumulus-capped mixed layers derived from a three-dimensional model. *Boundary-Layer Meteorology*, 186:495–527, 1980.

- S. H. Derbyshire. Nieuwstadt's stable boundary layer revisited. *Boundary-Layer Meteorology*, 116: 127–158, 1990.
- F. Ding, S. P. Arya, and Y-L. Lin. Large-eddy simulations of the atmospheric boundary layer using a new subgrid-scale model ii. weakly and moderately stable cases. *Environmental Fluid Mech.*, 1: 49–69, 2001.
- F. W. Dobson, S. D. Smith, and R. J. Anderson. Measuring the relationship between wind stress and sea state in the open ocean in the presence of swell. *Atmosphere-Ocean*, 32:237–256, 1994.
- M. A. Donelan. The dependence of the aerodynamic drag coefficient on wave parameters. In M. L. Banner, editor, *First Int. Conf. on Meteorology and Air-Sea Interaction of the Coastal Zone*, The Hague, Netherlands, 1982. American Meteorological Society.
- M. A. Donelan. *Air-sea interaction. The sea*, volume 9A. LéMehauté, B. and D. Hanes, 1990.
- W. M. Drennan and L. K. Shay. On the variability of the fluxes of momentum and sensible heat. *Boundary-Layer Meteorology*, 119(1):81–107, 2006.
- W. M. Drennan, K. K. Kahma, and M. A. Donelan. On momentum flux and velocity spectra over waves. *Boundary-Layer Meteorology*, 92(3):489–515, 1999.
- W. M. Drennan, H. C. Graber, and C. Quentin. On the wave age dependence of wind stress over pure wind seas. *J. Geophys. Res.*, 108(C3):FET10.1–FET10.13, 2003.
- W. M. Drennan, P. K. Taylor, and J. Yelland. Parametrizing the Sea Surface Roughness. *J. Phys. Oceanogr.*, 35:835–848, 2005.
- P. Drobinski and R. C. Foster. On the origin of near-surface streaks in the neutrally stratified boundary layer. *Boundary-Layer Meteorology*, 108(2):247–256, 2002.
- P. Drobinski, R. A. Brown, P. H. Flamant, and J. Pelon. Evidence of organized large eddies by ground-based doppler lidar, sonic anemometer and sodar. *Boundary-Layer Meteorology*, 88(3): 343–361, 1998.
- P. Drobinski, P. Carlotti, J. Redelsperger, R. M. Banta, V. Masson, and R. K. Newson. Numerical and experimental investigation of the neutral atmospheric surface layer. *J. Atmosph. Sci.*, 64(1): 137–156, 2007.
- P. et al. Drobinski. The structure of the near-neutral atmospheric surface layer. *J. Atmosph. Sci.*, 61:699–714, 2004.

- A. J. Dyer. A review of flux-profile relationships. *Boundary-Layer Meteorology*, 7(3):363–372, 1974.
- J. B. Edson, C. W. Fairall, P. G. Mestayer, and S. E. Larsen. A study of the inertial-dissipation method for computing air-sea fluxes. *Journal of Geophysical Research*, 96:10689–10711, 1991.
- S. Emeis and M. Türk. Wind-driven wave heights in the german bight. *Ocean Dynamics*, 59:463–475, 2009.
- I. Esau. *Large Eddy Simulation of Non-Local Turbulence and Integral Measures of Atmospheric Boundary Layers*. PhD thesis, Upsala University, 2003.
- D. Etling and R. A. Brown. Roll vortices in the planetary boundary layer: A review. *Boundary-Layer Meteorology*, 65(3):215–248, 1993.
- EU-Commission. Offshore wind energy: Action needed to deliver on the energy policy objectives for 2020 and beyond, 2008.
- T. Foken and B. Wichura. Tool for quality assessment of surface-based flux measurements. *Agricultural and Forest Meteorol.*, 78(1):83–105, 1996.
- R. C. Foster, F. Vianey, P. Drobinski, and P. Carlotti. Near-surface coherent structures and the vertical momentum flux in a large-eddy simulation of neutrally stratified boundary layer. *Boundary-Layer Meteorology*, 120(2):229–255, 2006.
- H. P. Frank and S. E. Larsen. Simulated wind power off-shore using different parametrizations for the sea surface roughness. *Wind Energy*, 80:67–79, 2000.
- G. L. Geernaert, S. E. Larsen, and F. Hansen. Measurements of the wind stress, heat flux, and turbulence intensity during storm conditions over the north sea. *J. Geophys. Res.*, 139(13):127–13, 1987.
- A. Gluhovsky and E. Agee. A definitive approach to turbulence statistical studies in planetary boundary layers. *J. Atmosph. Sci.*, 51(12):1682–1690, 1994.
- H. Gontier, A. P. Schaffarczyk, D. Kleinhaus, and R. Friedrich. A comparison of fatigue loads of wind turbine resulting from a non-gaussian turbulence model versus standard ones. *J. Phys.: Conference Series*, 75:012070 (11pp), 2007.
- M. M. Hand, N. D. Kelley, and M. J. Balas. Identification of wind turbine response to turbulent inflow structures. In *4th ASME Wind Energy Symposium/JSME Joint Fluids*, Honolulu, Hawaii, 2003.

- U. Högström. Non-dimensional wind and temperature profiles in the atmospheric surface layer: A re-evaluation. *Boundary-Layer Meteorology*, 42:55–78, 1987.
- U. Högström. Review of some basic characteristics of atmospheric surface layer. *Boundary-Layer Meteorology*, 78:215–246, 1996.
- J. Højstrup. Non-dimensional wind and temperature profiles in the atmospheric surface layer: A re-evaluation. *Boundary-Layer Meteorology*, 42(1):55–78, 1988.
- J. Højstrup. A statistical data screening procedure. *Measurement Sci. Technol.*, 4:153–157, 1993.
- IEC61400-1. Wind turbines-part 1: Design requirements. Technical report, International Electrotechnical Commission (IEC), 2005.
- IEC61400-12. Wind turbine generator systems-part 12: Wind turbine power performance testing. Technical report, International Electrotechnical Commission (IEC), 1998.
- P. A. E. M. Janssen. On the Effect of Ocean Waves on the Kinetic Energy Balance and Consequences for the Inertial Dissipation technique. *J. Phys. Oceanogr.*, 29:530–534, 1999.
- M. A. Jimenez. *Stability stratified atmospheric boundary layer: Study through Large Eddy Simulation, mesoscale modeling and observations*. PhD thesis, Universitat de les Illes Balears, September 2005.
- M. A. Jiménez and J. Cuxart. Large-eddy simulations of the stable boundary layer using the standard kolmogorov theory: Range of applicability. *Boundary-Layer Meteorology*, 115:241–261, 2005.
- H. K. Johnson, J. Højstrup, H., H. J. Vested, and S. E. Larsen. On the dependence of sea surface roughness on wind waves. *J. Phys. Oceanogr.*, 28:1702–1716, 2004.
- J. C. Kaimal and J. J. Finnigan. *Atmospheric Boundary Layer Flows*. Oxford Univ. Press, New York, 1994.
- J. C. Kaimal and J. E. Gaynor. Another look at sonic anemometry. *Boundary-Layer Meteorology*, 56:401–410, 1991.
- J. C. Kaimal, J. C. Wyngaard, Y. Izumi, and O. R. Cote. Spectral characteristics of surface-layer turbulence. *Q. J. Royal Meteorol. Soc.*, 98(417):563–589, 1972.
- B. Källstrand. Low level jets in a marine boundary layer during spring. *Contr. Atmos. Phys.*, 71: 359–373, 1998.

- N. D. Kelley. The identification of inflow fluid dynamics parameters that can be used to scale fatigue loading spectra of wind turbine structural components. In *3rd Energy-Sources Technol. Conf. and Exhib. (ETCE) on Wind Energy*, New Orleans, LA, 1994.
- N. D. Kelley, B. J. Jonkman, G. N. Scott, J. T. Bialasiewicz, and L. S. Redmond. The impact of coherent turbulence on wind turbine aeroelastic response and its simulation. In *WindPower Symp.*, Denver, Colorado, 2005.
- S. A. Kitaigorodskii and Y. A. Volkov. On the roughness parameter of the sea surface and the calculation of momentum flux in the near water level of the atmosphere. *Izv. Atmos. Oceanic Phys.*, 1:973–988, 1965.
- A. N. Kolmogorov. The local structure of turbulence in incompressible viscous fluid for very large reynolds numbers. In *SSR Academy of Sciences (Russian), translated into English by A. N. Kolmogorov and A. Nikolaevich (July 8 1991)*, volume 30, pages 299–303, 1941.
- B. Kosović and J. Curry. A large eddy simulation study of a quasi-steady, stably stratified atmospheric boundary layer. *J. Atmosph. Sci.*, 57:1052–1068, 2000.
- B. Lange and S. Tautz. Bestimmung von wrme- und impulsfluss in der marinen atmosphrischen grenzschicht fr die offshore-windenergienutzung (bago). Technical report, ForWind - Centre for Wind Energy Research, University of Oldenburg, Germany, 2004.
- B. Lange, H. K. Johnson, S. Larsen, J. Højstrup, H. Kofoed-Hansen, and M.J. Yelland. On detection of a wave age dependency for the sea surface roughness. *J. Phys. Oceanogr.*, 34:1441–1458, 2004.
- M. Lange and U. Focken. *Physical Approach to Short-Term Wind Power Prediction*. Springer, 2005.
- W. G. Large and S. Pond. Open Ocean Flux Measurements in Moderate to Strong Winds. *J. Phys. Oceanogr.*, 11:324–336, 1981.
- M. O. Letzel and S. Raasch. Large eddy simulation of thermally induced oscillations in the convective boundary layer. *Journal of the Atmospheric Sciences*, 60:2328–2341, 2003.
- M. O. Letzel, M. Kanda, and S. Raasch. A new dimension of urban climate modelling with parallel large-eddy simulation. In *6th Int. Conf. Urban Climate, , International Assoc. for Urban Climate*, Göteborg, Sweden, 2006.

- C. L. Lin, C-H. Moeng, P. P. Sullivan, and J. C. McWilliams. The effect of surface roughness on flow structures in a neutrally-stratified planetary boundary layer. *Physics of Fluids*, 9(11):3235–3249, 1997.
- L. Mahrt. Nocturnal boundary-layer regimes. *Boundary-Layer Meteorology*, 88(2):255–278, 1998.
- P. J. Mason and S. H. Derbyshire. Large-eddy simulation of the stably-stratified atmospheric boundary layer. *Boundary-Layer Meteorology*, 53:117–162, 1990.
- M. Mauder and T. Foken. *Documentation and Instruction Manual of the Eddy Covariance Software Package*, 2004.
- M. A. MJiménez and J. Cuxart. Study of the probability density functions from a large-eddy simulation for a stably stratified boundary layer. *Boundary-Layer Meteorology*, 118:401–420, 2006.
- A. S. Monin and A. M. Obukhov. Basic laws of turbulent mixing in the ground layer of the atmosphere. *Akad. Nauk. SSSR Geofiz. Inst. Tr.*, 151:163–187, 1959.
- D. Myrhaug and O. H. Slaattelid. Wind stress over waves: Effects of sea roughness and atmospheric stability. *J. Wind Eng. Indust. Aerodynamics*, 80:233–252, 1999.
- T. Neumann, K. Nolopp, and K. Herklotz. First operating experience with the fino1 research platform in the north sea. *DEWI Magazin*, 24, 2004.
- P. L. O'Neill, D. Nicolaidis, D. Honnery, and J. Soria. Autocorrelation functions and the determination of integral length with reference to experimental and numerical data. In *Proc. 115th Australasian Fluid Mech. Conf.*, Sydney, Australia, 1994.
- H. A. Panofsky and J. A. Dutton. *Atmospheric Turbulence*. John Wiley and Sons, New York, 1984.
- C. A. Paulson. The mathematical representation of wind speed and temperature profiles in the unstable atmospheric surface layer. *J. Appl. Meteorol.*, 6:857–861, 1970.
- J. Peinke, S. Barth, F. Böttcher, D. Heinemann, and B. Lange. Turbulence, a challenging problem for wind energy. *Physica A*, 338:187–193, 2004.
- E.L. Petersen, N. G. Mortensen, L. Landberg, J. Højstrup, and H. P. Frank. Wind power meteorology. part ii: siting and models. *Wind Energy*, 2:55–72, 1998.
- S. A. Piacsek and G. P. Williams. Conservation properties of convection difference schemes. *J. Computat. Phys.*, 6:392–405, 1970.

- S. Raasch and G. Harbusch. An analysis of secondary circulations and their effects caused by small-scale surface inhomogeneities using large-eddy simulation. *Boundary-Layer Meteorology*, 101:31–59, 2001.
- S. Raasch and M. Schröter. Palm : A large-eddy simulation model performing on massively parallel computers. *Meteorologische Zeitschrift*, 10:363–372, 2001.
- O. Reynolds. On the dynamical theory of turbulent incompressible viscous fluids and the determination of the criterion. *Phil. Trans. Royal Soc. London*, 186:123–161, 1895.
- L. F. Richardson. *Weather prediction by numerical process*. Cambridge University Press, 1922.
- A. Rutgersson, A. Smedman, and A. Omstedt. Measured and simulated latent and sensible heat fluxes at two marine sites in the baltic sea. *Boundary-Layer Meteorology*, 99(1):53–84, 2001.
- E. M. Saiki, C-H. Moeng, and P. P. Sullivan. Large-eddy simulation of the stably stratified planetary boundary layer. *Boundary-Layer Meteorology*, 95:1–30, 2000.
- P. Schotanus, F. T. M. Nieuwstadt, and H. A. R. De Bruin. Temperature measurement with a sonic anemometer and its application to heat and moisture fluxes. *Boundary-Layer Meteorology*, 26(1): 81–93, 2004.
- M. Schröter, J. Bange, and S. Raasch. Simulated airborne ux measurements in a les generated convective boundary layer. *Boundary-Layer Meteorology*, 95:437–456, 2001.
- C Sim, S. Basu, and L. Manuel. The influence of stable boundary layer flows on wind turbine fatigue loads. In *47th AIAA Aerospace Sci. Meeting Incl. The New Horizons Forum and Aerospace Expo.*, Orlando, Florida, 2009.
- A. Sjöblom and A. Smedman. Vertical structure in the marine atmospheric boundary layer and its implication for the inertial dissipation method. *Boundary-Layer Meteorology*, 109:1–25, 2003.
- A. Smedman, H. Bergström, and U. Högström. Spectra, variances and length scales in a marine stable boundary layer dominated by a low level jet. *Boundary-Layer Meteorology*, 75(3):211–232, 1995.
- S. D. Smith. Wind stress and heat flux over the ocean in gale force winds. *J. Phys. Oceanogr.*, 10 (5):709–726, 1980.

- S. D. Smith, R. J. Anderson, W. A. Oost, C. Kraan, N. Maat, J. De Cosmo, K. B. Katsaros, K. L. Davidson, K. Bumke, L. Hasse, and H. M. Chadwick. Sea surface wind stress and drag coefficients: The hexos results. *J. Geophys. Res.*, 60(1):109–142, 1992.
- N. Stefanatos, D. Zigras, D. Foussekis, F. Kokkalidis, P. Papadopoulos, and E. Binopoulos. Revising reference wind-speed definition for power performance measurements of multi-mw wind turbines. In *Proc. EWEC*, Brussels, 2008.
- G. Steinfeld, M. O. Letzel, S. Raasch, M. Kanda, and A. Inagaki. Spatial representativeness of single tower measurements and the imbalance problem with eddy-covariance fluxes: results of a large-eddy simulation study. *Boundary-Layer Meteorology*, 123:77–98, 2007.
- G. Steinfeld, S. Raasch, and T. Markkanen. Footprints in homogeneously and heterogeneously driven boundary layers derived from a lagrangian stochastic particle model embedded into large-eddy simulation. *Boundary-Layer Meteorology*, 129:225–248, 2008.
- R. Stull. *An Introduction to Boundary Layer Meteorology*. Kluwer Academic Publishers, 1998.
- G. I. Taylor. Statistical theory of turbulence. *Proc. Royal Soc. London. Series A, Mathematical and Phys. Sci.*, 151(873):421–444, 1935.
- H. Tennekes and J. L. Lumley. *A First Course in Turbulence*. MIT Press, Cambridge, MA, 1972.
- M. Türk and S. Emeis. Abhängigkeit der turbulenzintensität über see von der windgeschwindigkeit. *DEWI Magazin*, 30, 2007.
- J. Uhlenbrock. Entwicklung eines multigrid-verfahrens zur lösung elliptischer differentialgleichungen auf massivparallelrechnern und sein einsatz im les-modell palm. Master's thesis, Leibniz Universität Hannover, 2001.
- J. van der Tempel. *Design of Support Structures for Offshore Wind Turbines*. PhD thesis, Delf University of Technology, April 2006.
- H. van Dop and S. Axelsen. Large eddy simulation of the stable boundary-layer: A retrospect to nieuwstadt's early work. *Flow Turbulence Combustion*, 79:235–249, 2007.
- D. Vickers and L. Mahrt. Quality control and flux sampling problems for tower and aircraft data. *J. Atmosph. and Oceanic Technol.*, 14:512–526, 1997.
- D. Vickers and L. Mahrt. A solution for flux contamination by mesoscale motions with very weak turbulence. *Boundary-Layer Meteorology*, 118(3):431–447, 2006.

- Y. A. Volkov. Turbulent flux of momentum and heat in the atmospheric surface layer over a disturbed sea surface, izv. *Atmosph. Oceanic Phys.*, 6:770–774, 1970.
- E. Walls and N. LaWhite. Sodar and extrapolated tower wind shear profile comparison in various topographic conditions. In *Proc. EWEC*, Marceille, 2009.
- S. Weinbrecht, S. Raasch, A. Ziemann, K. Arnold, and A. Raabe. Comparison of large-eddy simulation data with spatially averaged measurements obtained by acoustic tomography: Presuppositions and first results. *Boundary-Layer Meteorology*, 111:441–465, 2004.
- J. M. Wilczak, S. P. Oncley, and S. A. Stage. Sonic anemometer tilt correction algorithms. *Boundary-Layer Meteorology*, 99:127–150, 2001.
- DEWI GmbH Deutsches Windenergie-Institut. Wind energy study 2008. assessment of the wind energy market until 2017. Technical report, DEWI, 2008.
- M. J. Yelland, B. I. Moat, P. K. Taylor, R. W. Pascal, J. Hutchings, and V. C. Corel. Wind stress measurements from the open ocean corrected for airflow distortion by the ship. *J. Phys. Oceanogr.*, 28:1511–1526, 1998.

Curriculum Vitae

PERSONAL DATA

Name Beatriz Cañadillas Perdomo
Date of birth 18 February 1975
Place of birth Tenerife, Spain

EDUCATION

2001-2002 M.Sc. in Renewable Energy (Wind and Solar energy) at Complutense University, Madrid
Fellowship award by Complutense University of Madrid (UCM) and the National Institute
of Meteorology (INM), Madrid

1994 - 1999 B.Sc. in Physics Sciences at La Laguna University, Tenerife

WORKING EXPERIENCE

Oct-2006 present Ph.D. student under the EU Marie Curie Training network. DEWI GmbH Deutsches
Windenergie Institut. Research and Studies Department. Germany

2003-2006 GAMESA EOLICA (Wind Turbine Manufacturer), Madrid.
Wind Assessment Department. Spain

2002-2003 IBERDROLA Engineering and Consultancy, Madrid.
Renewable Energy Department. Spain

1999-2001 CANARY UNIVERSITY HOSPITAL, Tenerife.
Environmental and Radiology Protection Department. Spain

KNOWLEDGE OF FOREIGN LANGUAGES

- Spanish (mother tongue)
- English (good)
- German (medium)

COMPUTING SKILLS

Numerical models: RAMS (Regional Atmospheric Modeling System),
 WRF (Weather Research and Forecasting)

Programming Languages: Fortran, Matlab, NCL

Scripting Languages: Unix Shell Scripting

Operating Systems: Unix/Linux, Windows

PROCEEDINGS ON CONFERENCES (recent)

- B. Canadillas, T. Neumann. SIMULATION OF NEUTRALLY STRATIFIED OFFSHORE BOUNDARY LAYER BY LARGE EDDY SIMULATIONS. DEWI, Deutsches Windenergie Institut. Wind Energy Conference (DEWEK) 2008 (OralPresentation), Bremen, Germany.
- Suselj,K., A.Sood, B.Canadillas and D.Heinemann (2007),THE PLANETARY BOUNDARY LAYER OVER THE NORTH SEA: MEASUREMENTS AND MESOSCALE SIMULATIONS. Geophysical Research Abstracts, Vol9, 09675, SRefID:16077962/gra/EGU2007A09675, Vienna, Austria.